buildings

MDPI

Article

Resilience Assessment of Building Hydrogen Energy Systems Under Extreme Climates: Environmental-Economic Synergistic Optimization Based on Emergy and Dynamic Simulation

Xiaoting Zhai [1], Junxue Zhang [1,*], Ashish T. Asutosh [2] and Weidong Wu [3]

[1] School of Civil Engineering and Architecture, Jiangsu University of Science and Technology, Zhenjiang 212100, China
[2] Construction Engineering and Management, Civil, Construction and Environmental Engineering, University of Delaware, Newark, DE 19716, USA
[3] School of Architecture, Anhui Science and Technology University, Bengbu 233000, China
* Correspondence: zjx2021@just.edu.cn

Abstract

The frequent occurrence of extreme climate events poses a severe challenge to the reliability of building energy systems. Hydrogen energy, with its long-term storage capacity, has become a key technology carrier for enhancing building resilience. This study constructs a resilience–environment–economy co-optimization framework that couples dynamic simulation and emergy analysis. Through a five-in-one approach of physical modeling, climate scenario generation, resilience quantification, emergy accounting, and multi-objective optimization, the resilience performance of building hydrogen energy systems under the scenario of extreme heat waves combined with grid failure is evaluated. The results show that the thermal time constant deviation of the electrolyzer is 4.06%, the correlation coefficient between the generated heat wave scenario sequence and the historical measured data is 0.94, the prediction deviation of the once-in-a-century extreme temperature is 0.5%, the environmental load rate is 4.33, the Pareto front contains 127 non-dominated solutions, and the comprehensive performance of the co-optimal solution is improved by 42% to 88%. Engineering suggestions: For public buildings in hot summer and cold winter regions, the hydrogen energy system should adopt a configuration of 50–60 kW electrolyzers and 50–70 kg hydrogen storage tanks, with a key load guarantee rate of no less than 95%, and the ecological cost is 35% lower than that of diesel backup. This study provides a quantitative decision-making tool for the resilience planning of building hydrogen energy systems under extreme climate conditions and can be extended to other high climate risk areas.

Keywords: building hydrogen energy systems; extreme climate; resilience assessment; emergy analysis; dynamic simulation; multi-objective optimization

Check for updates

Academic Editor: Xiaohu Yang

Received: 17 April 2026
Revised: 6 May 2026
Accepted: 12 May 2026
Published: 19 May 2026

Copyright: © 2026 by the authors. Licensee MDPI, Basel, Switzerland. This article is an open access article distributed under the terms and conditions of the Creative Commons Attribution (CC BY) license.

1. Introduction

The frequent occurrence and intensification of extreme climate events, including prolonged heatwaves, severe storms, and compound disasters, pose a severe challenge to the reliability of building energy supply systems [1,2]. Traditional building energy systems that rely on the power grid often show vulnerability under such conditions, leading to power outages and endangering the safety of people and the critical functions of buildings [3,4]. Hydrogen energy systems, with their long-term energy storage capabilities and cross-seasonal energy balance characteristics, have emerged as an important technical

approach to address these challenges. By integrating electrolyzers, hydrogen storage tanks, and fuel cells, building-scale hydrogen energy systems can provide resilient backup power when the grid fails, while also supporting the achievement of deep decarbonization goals [5,6].

In the field of building energy system resilience research, scholars at home and abroad have carried out a large amount of work, mainly focusing on the energy supply reliability of power systems, photovoltaic-energy storage coupling systems, and traditional fossil fuel backup systems under extreme climate events [7–9]. Internationally, the National Renewable Energy Laboratory and Lawrence Berkeley National Laboratory in the United States were among the first to conduct research on building energy system resilience assessment methods, proposing a resilience quantification index system based on performance function integration, recovery time, and loss area. European research institutions have focused on the coordinated response mechanism of multi-energy complementary systems under extreme events, exploring the impact of electricity–heat–cooling multi-energy flow coupling on system resilience [10–14]. Domestic scholars have also conducted related research in recent years. Research teams from Tsinghua University and Tianjin University have modeled and analyzed the resilience performance of building photovoltaic-energy storage systems under extreme weather conditions such as typhoons and heavy snow, and proposed resilience improvement strategies considering equipment redundancy design and island operation capability [15–18]. However, most of the above studies have centered on power systems, with relatively limited attention paid to hydrogen energy as a new energy storage carrier, especially in terms of the dynamic response characteristics of hydrogen energy systems at the building scale, multi-time scale coupling mechanisms, and resilience failure thresholds, which lack systematic quantitative understanding [19,20].

Regarding hydrogen system evaluation methods, existing research primarily adopts two approaches: techno-economic analysis (TEA) and life cycle assessment (LCA) [21–23]. The International Renewable Energy Agency (IRENA) and the Joint Research Centre (JRC) of the European Union have continuously published reports on the costs and technological development of hydrogen systems, providing important benchmarks for economic assessments. Domestically, institutions such as the China Hydrogen Alliance and Tsinghua University have also conducted research on the costs and carbon emissions across the entire hydrogen industry chain, covering electrolyzers, storage and transportation, and fuel cells [24,25]. These studies have laid the foundation for understanding the economic and environmental performance of hydrogen systems but have two limitations: first, techno-economic analysis is mostly based on steady-state assumptions, making it difficult to capture the transient behavior and recovery processes of systems under extreme operating conditions; second, while traditional LCA can account for carbon emissions, it struggles to uniformly quantify the ecological contributions of different types of environmental resources, particularly lacking the capacity to account for the free natural resources on which green hydrogen production depends. The emergy analysis method, pioneered by ecologist Odum, offers the potential to address this gap by using solar emjoules to uniformly account for various resource inputs [26–28]. However, the application of emergy analysis in the field of building energy systems is still in its early stages and is mostly limited to static accounting; it has not yet been effectively coupled with dynamic process simulation and resilience assessment, leaving its application under extreme climate scenarios largely unexplored [29,30].

In the field of multi-objective optimization and collaborative decision-making, scholars at home and abroad have conducted extensive research to explore the trade-offs among multiple objectives such as cost, carbon emissions, and energy efficiency in energy systems [31–33]. Multi-objective evolutionary algorithms like NSGA-II and MOPSO have been

widely applied in the optimal design of building energy systems, and Pareto frontier analysis provides an effective tool for balancing different objectives. However, most existing studies focus on cost and carbon emissions as optimization goals, with few incorporating resilience indicators as independent optimization dimensions within the collaborative framework. The few studies that involve resilience often treat it as a constraint rather than an optimization objective, which fails to fully reveal the intrinsic trade-offs between resilience levels and economic and environmental goals. Moreover, most existing research is deterministic optimization, with limited handling of uncertainties such as climate risk probabilities, equipment performance degradation, and fuel price fluctuations, making it difficult to support resilience decisions in real risk scenarios.

This paper re-examines the deficiencies of existing research at the following three levels. First, at the model level, current studies on the resilience of building energy systems mostly focus on the power system or photovoltaic energy storage systems, lacking systematic modeling and validation of the dynamic response characteristics of hydrogen energy systems under extreme conditions, such as the time-scale matching of multi-energy coupling of electricity, hydrogen and heat, and the transient behavior of electrolyzers and fuel cells. Second, at the method level, existing assessment methods such as techno-economic analysis or life cycle assessment are unable to uniformly quantify the contributions and costs of different types of environmental resources, and thus cannot effectively reveal the implicit ecological trade-offs associated with resilience enhancement. They also fail to incorporate resilience as an independent optimization dimension into the framework of environmental and economic synergy. Third, at the scenario level, existing research is mostly based on historical average climate conditions or single fault scenarios, lacking probabilistic characterization of compound events of extreme climate and grid failure and quantitative description of their impact on the resilience threshold of the system. Based on the above literature review, this study clearly focuses on the core issue of dynamic resilience quantification and environmental-economic synergy optimization of building hydrogen energy systems under extreme climate conditions, and addresses the aforementioned three deficiencies through the coupling of dynamic simulation and emergy analysis methods.

To address the aforementioned research deficiencies, this study constructs an integrated framework that couples dynamic simulation with emergy analysis to achieve the coordinated optimization of the resilience, environmental benefits, and economic efficiency of building hydrogen energy systems under extreme climate conditions. The framework consists of five interrelated modules: system physical dynamic modeling, extreme climate scenario generation, resilience quantification, emergy analysis, and multi-objective optimization. The main innovations include: revealing the nonlinear threshold characteristics and dynamic response delays of multi-energy coupling in hydrogen energy systems; introducing the emergy analysis method to identify the implicit environmental trade-offs overlooked by monetary assessment; and identifying the Pareto optimal design boundaries determined by the probability of climate risks, building load characteristics, and the resilience of regional hydrogen energy supply chains. Through a six-stage system validation that integrates experimental data, historical climate records, and global cost databases, the robustness and engineering applicability of the research method are ensured. The research results can provide quantitative decision support for the resilient and sustainable energy planning of buildings in high climate risk areas.

2. Materials and Methods

2.1. Problem Description

At present, research on the resilience of building energy systems mainly focuses on the reliability of power supply in extreme climate events for power systems, photovoltaic-

energy storage coupling systems, and traditional fossil fuel backup systems. Researchers have established an initial assessment framework from dimensions such as equipment redundancy design, island operation capability, and resilience. However, as energy systems transition towards deep decarbonization, hydrogen energy, with its high energy density, long-term storage capacity, and cross-seasonal regulation potential, is regarded as a key carrier for ensuring building energy security under extreme climates. Nevertheless, existing studies lack systematic quantitative understanding of the dynamic response characteristics, multi-time-scale coupling mechanisms, and resilience failure thresholds of building-level hydrogen energy systems under extreme conditions, especially research that considers hydrogen energy systems as the main body for enhancing resilience rather than a supplement to the traditional power grid is still in its infancy (Figure 1).

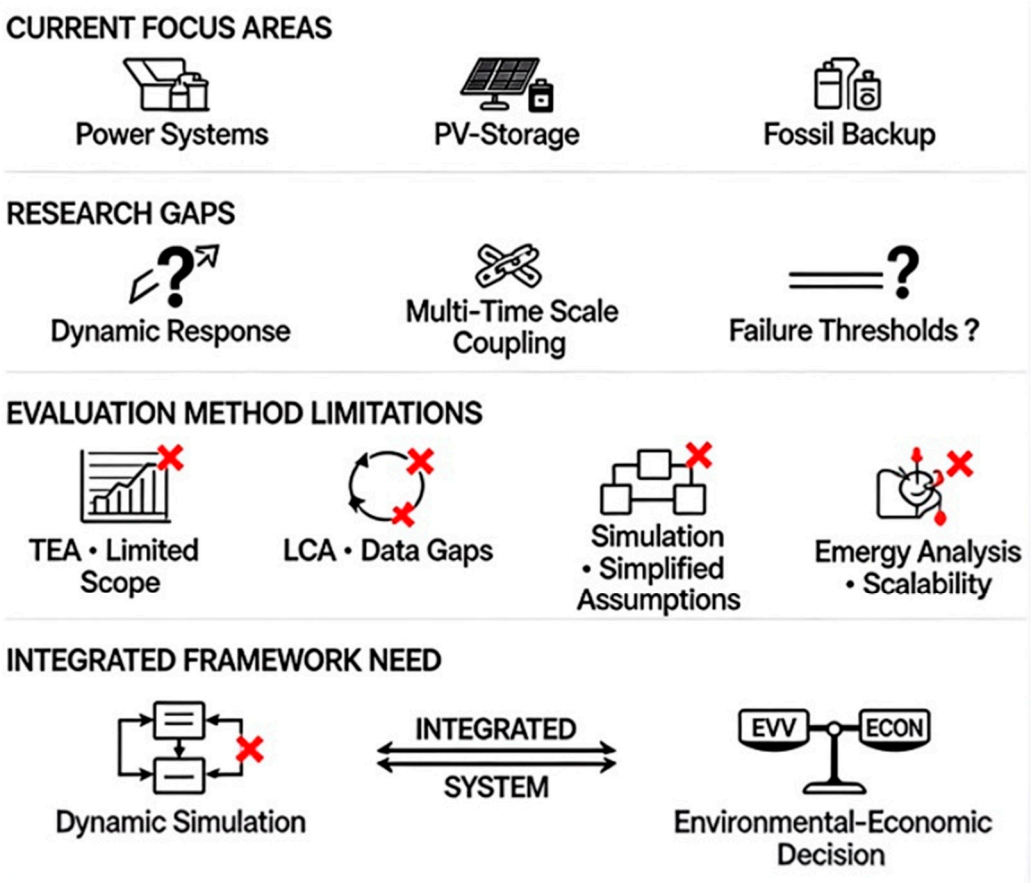


Figure 1. Presentation of Current Research Issues.

At the level of assessment methods, the current optimization research on hydrogen energy systems in existing buildings mostly adopts technical economic analysis (TEA) or life cycle assessment (LCA), focusing on minimizing costs or carbon emissions under normal operating conditions. This makes it difficult to effectively characterize the transient behavior and recovery process of the system under extreme climate shocks. On the one hand, dynamic simulation methods can capture the physical thermodynamic responses of hydrogen energy systems on a scale from minutes to seasons, but often ignore the energy quality differences among different energy carriers (electricity, hydrogen, heat) and the quantification of ecological and environmental inputs. On the other hand, although the emergy analysis method can unify natural environmental resource inputs and socio-economic feedback to a solar joule benchmark, its application in dynamic resilience scenarios with time-varying coupling remains blank. Therefore, it is urgently necessary to construct an assessment framework that integrates dynamic process simulation and

environment-economic collaborative decision-making to reveal the internal trade-offs and synergy mechanisms of building hydrogen energy systems under the three-dimensional goals of "resilience-environment-economy" in extreme climate conditions, providing theoretical support for the resilience planning of low-carbon building energy systems in highly uncertain climate scenarios [34].

2.2. Research Framework

This study constructs a systematic research framework integrating "modeling–validation–optimization" in a trinity, aiming to precisely assess the resilience performance of building hydrogen energy systems under extreme climate conditions and achieve environmental-economic synergy optimization. The framework vertically encompasses five core model modules and horizontally embeds six progressive validation stages, forming a closed-loop research logic (Figure 2).

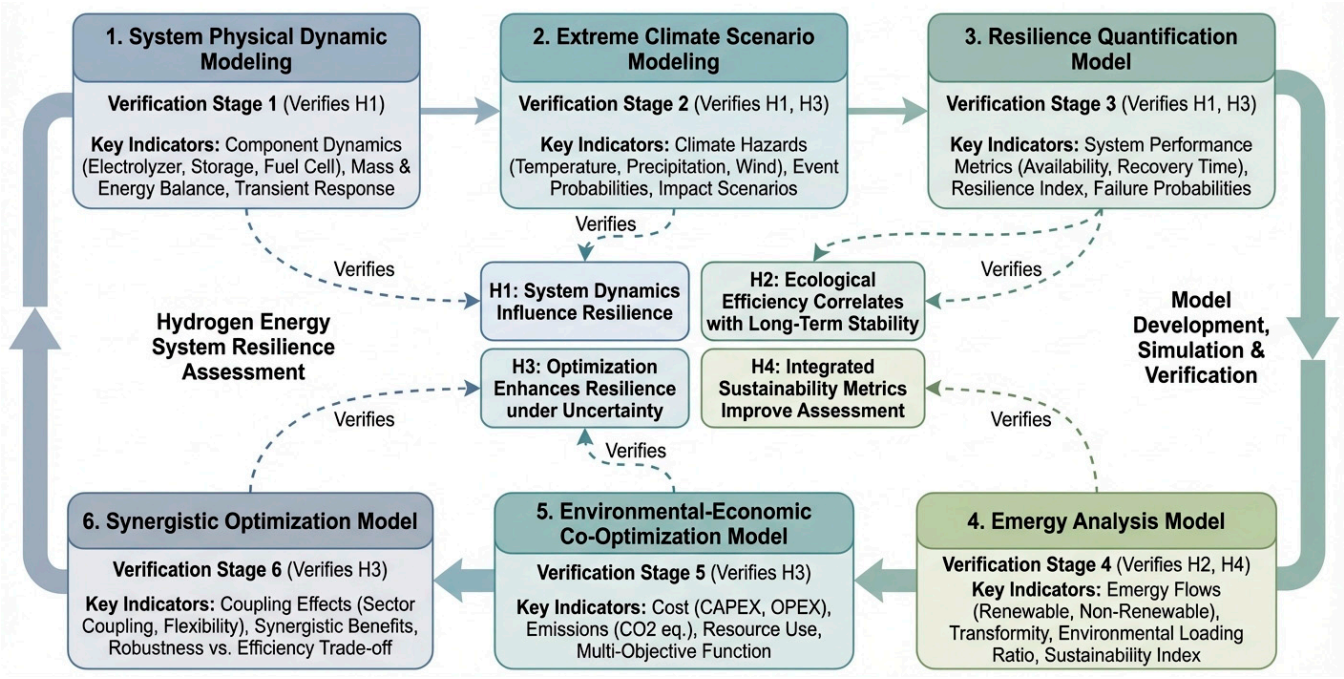


Figure 2. Research Framework for Resilience Assessment of Hydrogen Energy Systems.

Firstly, the system physical dynamic model (Module 1) captures the transient response and nonlinear threshold characteristics of the system under extreme conditions by building sub-models of electrolyzers, fuel cells, hydrogen storage, and battery energy storage, and coupling the multi-energy flow balance relationship of electricity, hydrogen, and heat, directly serving the verification of research hypothesis H1, which reveals that system resilience is not only determined by equipment capacity configuration but also constrained by the dynamic response delay of multi-energy coupling. On this basis, the extreme climate scenario model (Module 2) generates compound extreme event scenarios including heatwave intensity, duration, and grid failure probability by using extreme value theory and Copula joint distribution methods, providing a design benchmark that conforms to regional risk characteristics for resilience assessment. The resilience quantification model (Module 3) builds a comprehensive performance function and multi-dimensional resilience indicators (including peak loss, recovery time, and resilience loss area) to dynamically depict the performance evolution of the system under different extreme scenarios. The above three modules jointly constitute the technical main line of "dynamic modeling—scenario generation—resilience quantification", supporting the preliminary verification of H1 and

H3. The emergy analysis model (Module 4) introduces solar joule as a unified environmental benchmark, incorporating the system's natural resource input, ecological carrying cost, and avoided environmental loss into a unified accounting framework, revealing the hidden ecological value that traditional monetization assessment cannot quantify, providing verification basis for hypotheses H2 and H4. Finally, the environmental-economic synergy optimization model (Module 5) integrates life-cycle cost, emergy environmental load, and resilience constraints into a multi-objective optimization framework, solving the Pareto frontier through the NSGA-II algorithm to identify the synergy optimal design boundary determined by climate risk probability, building load characteristics, and hydrogen energy supply chain elasticity, achieving the core verification of H3. The entire framework is traversed by six-stage validation stages, from physical model calibration, climate scenario verification, resilience index consistency analysis, to emergy coefficient verification, economic parameter validation, and optimization algorithm robustness testing, progressively ensuring the scientificity and reproducibility of research results, ultimately providing theoretical support and quantitative decision-making tools for the resilience planning of low-carbon building hydrogen energy systems under extreme climate uncertainty.

2.3. Research Hypothesis

H1. *Under the impact of extreme climate events, the resilience performance of building-integrated hydrogen energy systems exhibits significant nonlinear threshold characteristics. Their failure probability and recovery capacity depend not only on equipment capacity configuration but are also constrained by the dynamic response delay of the "electricity–hydrogen–heat" multi-energy coupling inherent to hydrogen carriers. Simply increasing equipment scale cannot linearly improve system resilience; instead, there exists a resilience inflection point jointly determined by energy storage status, climate intensity, and system control logic.*

H2. *A coupled method based on emergy analysis and dynamic simulation can effectively reveal the hidden "environmental-economic" trade-offs of building-integrated hydrogen energy systems under extreme climate scenarios. Specifically, the infrastructure investment and ecological carrying costs incurred to enhance resilience may manifest as environmental liabilities under normal operating conditions. However, during power/energy supply interruptions caused by extreme climate events, the avoided environmental losses and economic damages can yield positive net benefits over the full life cycle.*

H3. *There exists a set of design and operational boundary conditions that achieve synergy among resilience, environment, and economy. These conditions enable building-integrated hydrogen energy systems to sustain critical loads within acceptable economic costs and ecological investment thresholds when facing predefined extreme climate scenarios. This optimal solution set is not a single technical configuration, but a multi-objective Pareto frontier jointly shaped by climate risk probability, building load characteristics, and regional hydrogen supply chain resilience.*

H4 (Emergy Perspective). *Resilience optimization based solely on monetary costs systematically underestimates the ecological value of hydrogen energy systems, as monetary prices fail to fully internalize the contribution of free natural resources—such as solar and wind energy—that underpin green hydrogen production. In contrast, the emergy approach, through a unified environmental benchmark, can reveal that hydrogen energy systems offer a higher ecological resilience return compared to conventional alternatives such as diesel backup generators under extreme climate conditions.*

2.4. Research Methods and Computational Models

2.4.1. Introduction to Emergy Analysis Methodology

Emergy analysis is an ecological-economic accounting theory developed by ecologist H.T. Odum in the 1980s. Its core principle lies in using the solar emjoule (seJ) as a unified measurement unit to convert different forms of energy, materials, services, and information within both natural and human economic systems into the total amount of solar energy directly or indirectly required for their formation. This methodology overcomes the fundamental limitation inherent in traditional energy analysis—namely, the inability to directly sum energy flows of different qualities—by introducing the concept of transformity. Transformity is defined as the total solar emergy required to produce one unit of a given product or service, enabling energy flows of varying quality to be additively accounted for under a unified ecological thermodynamic baseline [34–40].

Unlike cost–benefit analysis based on monetary prices, emergy analysis emphasizes the value of ecological work contributed freely by the natural environment. It incorporates primary resource inputs such as solar radiation, wind, rainwater chemical potential, and geothermal heat into the accounting framework. Through composite indicators including the Environmental Loading Ratio (ELR), Emergy Yield Ratio (EYR), and Emergy Sustainability Index (ESI), it quantifies the pressure exerted by human activities on ecosystems and the sustainability characteristics of system development. In the context of building energy system research, emergy analysis reveals the implicit environmental costs that traditional economic evaluations tend to overlook. These include the emergy embodied in silicon materials derived from ancient geological processes during photovoltaic module manufacturing, the water resource emergy consumed in green hydrogen production, and the ecological service functions preserved by avoiding power supply interruptions during extreme climate events. This provides ecologically grounded thermodynamic information to support environmental-economic decision-making beyond the boundaries of monetary valuation alone.

Computational platform and software environment: The dynamic simulation and multi-objective optimization in this study were constructed on the MATLAB R2023a platform. The physical dynamic model of the system was built modularly using MATLAB/Simulink, and the ODE solver ode45 was selected. The generation of extreme climate scenarios and the calculation of emergy analysis were implemented in MATLAB scripts. Two algorithms, NSGA-II and MOPSO, were adopted for multi-objective optimization, developed based on the built-in Global Optimization Toolbox of MATLAB and open-source algorithm libraries. All simulations and optimization calculations were completed on a workstation equipped with an Intel Core i9-10900K CPU and 128 GB RAM.

2.4.2. Calculation Module

The model is divided into five modules: the system physical dynamic model (for verifying H1), the extreme climate scenario model, the resilience quantification model, the emergy analysis model (for verifying H2), and the environment-economic collaborative optimization model (for verifying H3).

Part I: System Physical Dynamic Modeling

1.1 State-Space Representation of Hydrogen System

The system state vector is defined as:

$$\mathbf{X}(t) = \left[P_{\mathrm{el}}(t)\ P_{\mathrm{fc}}(t)\ L_{\mathrm{H_2}}(t)\ T_{\mathrm{stack}}(t)\ \mathrm{SOC}_{\mathrm{bat}}(t)\right]^{\top} \quad (1)$$

The dynamic evolution of the system is governed by:

$$\frac{d}{dt}\begin{bmatrix} P_{\mathrm{el}}(t) \\ P_{\mathrm{fc}}(t) \\ L_{\mathrm{H_2}}(t) \\ T_{\mathrm{stack}}(t) \\ \mathrm{SOC}_{\mathrm{bat}}(t) \end{bmatrix} = \mathbf{A}(t) \cdot \begin{bmatrix} P_{\mathrm{el}}(t) \\ P_{\mathrm{fc}}(t) \\ L_{\mathrm{H_2}}(t) \\ T_{\mathrm{stack}}(t) \\ \mathrm{SOC}_{\mathrm{bat}}(t) \end{bmatrix} + \mathbf{B}(t) \cdot \mathbf{U}(t) \tag{2}$$

1.2 Electrolyzer Electrochemical-Thermal Coupling

The hydrogen production rate from the electrolyzer is expressed as:

$$\dot{m}_{\mathrm{H_2,el}}(t) = \frac{\eta_{\mathrm{el}}(t) \cdot P_{\mathrm{el}}(t)}{\mathrm{LHV}_{\mathrm{H_2}}} \tag{3}$$

The electrolyzer efficiency exhibits temperature-dependent behavior:

$$\eta_{\mathrm{el}}(t) = \eta_{\mathrm{el}}^{0} \cdot \exp\left(-\frac{E_a}{R \cdot T_{\mathrm{stack}}(t)}\right) \cdot \left(1 - \frac{j(t)}{j_{\mathrm{lim}}}\right)^2 \tag{4}$$

Combining the above expressions yields:

$$\dot{m}_{\mathrm{H_2,el}}(t) = \frac{P_{\mathrm{el}}(t)}{\mathrm{LHV}_{\mathrm{H_2}}} \cdot \eta_{\mathrm{el}}^{0} \cdot \exp\left(-\frac{E_a}{R \cdot T_{\mathrm{stack}}(t)}\right) \cdot \left(1 - \frac{j(t)}{j_{\mathrm{lim}}}\right)^2 \tag{5}$$

The thermal balance of the electrolyzer stack is given by:

$$C_{\mathrm{th,el}} \cdot \frac{dT_{\mathrm{stack}}(t)}{dt} = P_{\mathrm{el}}(t) \cdot (1 - \eta_{\mathrm{el}}(t)) - \dot{Q}_{\mathrm{cool}}(t) - \dot{Q}_{\mathrm{loss}}(t) \tag{6}$$

1.3 Fuel Cell Electrochemical Model

The fuel cell output power is determined by hydrogen consumption:

$$P_{\mathrm{fc}}(t) = \dot{m}_{\mathrm{H_2,fc}}(t) \cdot \mathrm{LHV}_{\mathrm{H_2}} \cdot \eta_{\mathrm{fc}}(t) \tag{7}$$

Fuel cell efficiency depends on current density and operating temperature:

$$\eta_{\mathrm{fc}}(t) = \eta_{\mathrm{fc,0}} \cdot \left[1 - \beta\left(\frac{i(t)}{i_{\mathrm{ref}}} - 1\right)^2\right] \cdot \left(1 - \gamma(T_{\mathrm{fc}}(t) - T_{\mathrm{ref}})^2\right) \tag{8}$$

1.4 Hydrogen Storage Dynamics

The pressure inside the hydrogen storage tank is modeled using the real gas equation:

$$p_{\mathrm{H_2}}(t) = \frac{Z(p,T) \cdot R \cdot T_{\mathrm{tank}}}{M_{\mathrm{H_2}} \cdot V_{\mathrm{tank}}} \cdot m_{\mathrm{H_2}}(t) \tag{9}$$

The hydrogen mass balance within the storage system is:

$$\frac{dm_{\mathrm{H_2}}(t)}{dt} = \dot{m}_{\mathrm{H_2,el}}(t) - \dot{m}_{\mathrm{H_2,fc}}(t) - \dot{m}_{\mathrm{H_2,vent}}(t) \tag{10}$$

1.5 Battery Energy Storage System Model

The battery state of charge dynamics is expressed as:

$$\frac{d\,SOC_{bat}(t)}{dt} = \frac{P_{bat,ch}(t) \cdot \eta_{ch} - P_{bat,dis}(t)/\eta_{dis}}{E_{bat,cap}} \tag{11}$$

Battery degradation is modeled as a function of depth of discharge:

$$N_{cycle}(DoD) = N_{cycle,0} \cdot DoD^{-k_{bat}} \cdot \exp\left(-\frac{E_{a,bat}}{R \cdot T_{bat}}\right) \tag{12}$$

1.6 Electricity-Thermal-Hydrogen Coupling Balance

The electric power balance equation under grid failure conditions is:

$$P_{PV}(t) + P_{fc}(t) + P_{bat,dis}(t) + P_{grid}(t) = P_{load,el}(t) + P_{el}(t) + P_{bat,ch}(t) \tag{13}$$

Waste heat recovered from the fuel cell is given by:

$$\dot{Q}_{rec}(t) = P_{fc}(t) \cdot \left(\frac{1}{\eta_{fc}(t)} - 1\right) \cdot \phi_{rec} \tag{14}$$

Part II: Extreme Climate Scenario Modeling

2.1 Extreme Climate Event Probability Model

The cumulative distribution function for extreme climate intensity follows the Generalized Extreme Value distribution:

$$F(I_{\text{clim}}) = \exp\left[-\left(1 + \xi \cdot \frac{I_{\text{clim}} - \mu}{\sigma}\right)^{-1/\xi}\right],\ 1 + \xi \cdot \frac{I_{\text{clim}} - \mu}{\sigma} > 0 \tag{15}$$

2.2 PV Output Degradation Under Extreme Climate

Photovoltaic power output under extreme high temperatures is modeled as:

$$P_{\text{PV}}(t) = P_{\text{PV,STC}} \cdot \frac{G(t)}{G_{\text{STC}}} \cdot [1 - \alpha_T \cdot (T_{\text{cell}}(t) - T_{\text{STC}})] \cdot \kappa_{\text{dust}}(t) \cdot \kappa_{\text{cloud}}(t) \tag{16}$$

Part III: Resilience Quantification Model

3.1 Time-Varying Resilience Function

System resilience over the event duration is defined as:

$$R(\tau) = \frac{\int_{t_0}^{t_0+\tau} Q(t)\, dt}{\int_{t_0}^{t_0+\tau} Q_{\text{norm}}\, dt} \tag{17}$$

3.2 Performance Function Definition

The comprehensive performance function integrates electrical and thermal load satisfaction:

$$Q(t) = w_{\text{el}} \cdot \psi_{\text{el}}(t) + w_{\text{th}} \cdot \psi_{\text{th}}(t) \tag{18}$$

Electrical load satisfaction with exponential penalty for deficits is expressed as:

$$\psi_{\text{el}}(t) = \min\left(1, \frac{P_{\text{sup,el}}(t)}{P_{\text{dem,el}}(t)}\right) \cdot \exp\left(-\lambda_{\text{el}} \cdot \frac{P_{\text{dem,el}}(t) - P_{\text{sup,el}}(t)}{P_{\text{dem,el}}(t)}\right) \tag{19}$$

3.3 Multi-Dimensional Resilience Metrics

Peak performance loss:

$$R_{\text{loss}} = \frac{Q_{\text{norm}} - Q_{\text{min}}}{Q_{\text{norm}}} \tag{20}$$

Recovery time:

$$T_{\text{rec}} = \min\{t \geq t_{\text{end}} : Q(t) \geq 0.95\, Q_{\text{norm}}\} \tag{21}$$

Resilience loss area:

$$R_{\text{area}} = \int_{t_0}^{t_{\text{rec}}} \left(1 - \frac{Q(t)}{Q_{\text{norm}}}\right) dt \tag{22}$$

Part IV: Emergy indicators calculation model

4.1 Total Emery Flow Calculation

Total emery input to the system is:

$$Em_{total} = \sum_i Em_i^{local} + \sum_j Em_j^{import} \tag{23}$$

4.2 Component-Level Emery Intensities

Emery embodied in the electrolyzer:

$$Em_{el} = \sum_k (m_{k,el} \cdot UEV_k) + Em_{el,OM} \tag{24}$$

Emery embodied in the hydrogen storage tank:

$$Em_{tank} = m_{steel} \cdot UEV_{steel} + m_{CFRP} \cdot UEV_{CFRP} \tag{25}$$

4.3 Avoided Loss Emery Under Extreme Climate

Environmental emery losses avoided during extreme climate events:

$$Em_{avoided} = \int_{t_0}^{t_0+\tau} \left[\dot{Em}_{grid,loss}(t) + \dot{\text{Em}}_{thermal,loss}(t)\right] \cdot \Pi_{failure}(t)\, dt \tag{26}$$

4.4 Emery-Based Resilience Indicators

Emery return on investment:

$$\text{EmEROI} = \frac{Em_{avoided}}{Em_{total} \cdot (1 + \delta_{risk})} \tag{27}$$

Environmental loading ratio:

$$ELR = \frac{Em_{nonrenewable} + Em_{imported}}{Em_{renewable}} \tag{28}$$

Emery sustainability index:

$$ESI = \frac{\text{EmEROI}}{ELR} \tag{29}$$

4.5 Emery-Economic Coupling Transformation

Ecological cost derived from emery flows:

$$C_{eco} = \frac{Em_{total}}{EMR_{local}} \tag{30}$$

Part V: Environmental-Economic Co-Optimization Model

5.1 Multi-Objective Optimization Formulation

The decision variable vector is defined as:

$$\mathbf{x}_{\text{design}} = [C_{\text{el}}\ C_{\text{fc}}\ V_{\text{tank}}\ C_{\text{bat}}\ \ldots]^{\top} \tag{31}$$

The multi-objective optimization problem is:

$$\min \mathbf{F}\left(\mathbf{x}_{\text{design}}\right) = \left[f_{\text{eco}}\left(\mathbf{x}_{\text{design}}\right)\ f_{\text{env}}\left(\mathbf{x}_{\text{design}}\right)\ f_{\text{res}}\left(\mathbf{x}_{\text{design}}\right)\right]^{\top} \tag{32}$$

5.2 Economic Objective Function

Life cycle cost including capital, operation, replacement, fuel, and salvage value:

$$f_{\text{eco}} = C_{\text{cap}} + \sum_{t=1}^{T} \frac{C_{\text{OM}}(t) + C_{\text{replace}}(t) + C_{\text{fuel}}(t)}{(1+r)^t} - \frac{C_{\text{salvage}}}{(1+r)^T} \tag{33}$$

5.3 Environmental Objective Function

Environmental objective from the emery perspective:

$$f_{\text{env}} = Em_{\text{total}} + \int_0^T \dot{Em}_{\text{emission}}(t) \cdot UEV_{CO_2} dt - Em_{\text{avoided,clim}} \tag{34}$$

5.4 Resilience Constraints

The resilience constraints based on Hypothesis H1 are:

$$R_{\text{area}} \leq R_{\text{area,max}}, \; T_{\text{rec}} \leq T_{\text{rec,max}} \tag{35}$$

5.5 Synergistic Optimization Objective

The synergistic objective combining economic, environmental, and resilience dimensions:

$$f_{\text{syn}} = w_{\text{eco}} \cdot \frac{f_{\text{eco}}}{f_{\text{eco}}^0} + w_{\text{env}} \cdot \frac{f_{\text{env}}}{f_{\text{env}}^0} - w_{\text{res}} \cdot \frac{R_{\text{area}}^0}{R_{\text{area}}} \tag{36}$$

5.6 Pareto Front Identification and Optimal Solution Selection

The Pareto front is defined as:

$$\text{P} = \left\{ \mathbf{X} \in \text{X} : \nexists \mathbf{X}' \in \text{X}, \mathbf{F}(\mathbf{X}') \prec \mathbf{F}(\mathbf{X}) \right\}$$

The compromise solution is selected using the ideal point method:

$$\mathbf{X}^* = \underset{\mathbf{X} \in \text{P}}{\text{argmin}} \sqrt{\sum_{i=1}^{3} \left(\frac{f_i(\mathbf{X}) - f_i^{\text{ideal}}}{f_i^{\text{nadir}} - f_i^{\text{ideal}}} \right)^2} \tag{37}$$

Part VI The formula for the thermal equilibrium equation of a battery

$$m_b c_{p,b} \frac{dT_b(t)}{dt} = I(t)^2 R_{bat}(T_b) + T_b(t) \frac{\Delta S}{nF} I(t) - h_b A_b (T_b(t) - T_{amb}(t)) \tag{38}$$

On the left side is the product of the battery's heat capacity and the rate of temperature change; on the right side, the first term is the Joule heat, where R is the internal resistance of the battery and is a function of temperature; the second term is the reversible reaction heat, where ΔS is the entropy change of the reaction, n is the number of electrons transferred, and F is the Faraday constant; the third term is the heat dissipation term, where U is the comprehensive heat transfer coefficient, A is the battery's surface area, and Tenv is the ambient temperature. Under heat wave conditions, the ambient temperature rises significantly, reducing the driving force for heat dissipation, which leads to an intensified temperature rise of the battery.

2.4.3. Explanation of Method Limitations

Emergy analysis involves three significant sources of uncertainty in engineering applications. First, emergy transformities are highly dependent on the selection of the global emergy baseline. This study adopts the 15.83×10^{24} seJ/year baseline. If alternative baselines of 12.00×10^{24} or 9.44×10^{24} seJ/year are used, major material transformities fluctuate by 15 to 25 percent, leading to a relative change in the environmental loading ratio of 10 to

18 percent. Second, differences in defining material processing boundaries introduce additional uncertainty. Whether the emergy accounting of carbon fiber composites includes the precursor polymerization process causes a deviation of approximately 13 percent in its transformity. Third, regional disparities in emergy baselines cannot be ignored. This study finds systematic differences between locally calibrated transformities and global average values. To address these uncertainties, this study employs multi-baseline cross-validation and regional calibration of key transformities. Engineering applications are advised to use interval analysis or scenario comparisons to characterize the confidence range of emergy assessment results.

This study positions emergy analysis as a complementary tool to life cycle assessment and techno-economic analysis rather than a substitute. Life cycle assessment excels at quantifying traditional environmental indicators such as carbon emissions and energy consumption but struggles to account for the contribution of free natural resources, which is precisely the core strength of emergy analysis. Techno-economic analysis focuses on monetary costs and benefits, providing economic feasibility benchmarks for investment decisions, yet it cannot internalize the value of ecological services. The ecological functions protected by hydrogen systems avoiding grid failures during extreme climate events cannot be directly estimated through market prices, whereas emergy analysis offers an alternative ecological value representation through the avoided loss emergy indicator. This study adopts a three-tier assessment architecture. Techno-economic analysis provides economic constraints including life cycle cost and payback period. Life cycle assessment establishes carbon emission boundaries. Emergy analysis reveals the ecological dimension overlooked by monetary valuation. The synergistic application of these three methods provides a more complete decision-support tool chain for resilience planning of building hydrogen systems, avoiding the assessment blind spots inherent in any single method.

2.5. Research Indicator Group

Tables 1–7 present the indicator groups applied in this study.

Table 1. System Physical Performance Indicators (8 indicators).

No.	Indicator	Symbol	Definition Formula	Unit	Related Hypothesis
1	Electrolyzer Efficiency	eta_el	eta_el equals eta_el0 multiplied by exp of negative Ea divided by R times T_stack multiplied by one minus j over j_lim squared	-	H1
2	Average Hydrogen Production Rate	m_dot_H2_el_avg	Average hydrogen production rate equals one over T times the integral from zero to T of hydrogen production rate with respect to time	kg/h	H1
3	Fuel Cell Efficiency	eta_fc	eta_fc equals eta_fc0 multiplied by one minus beta times i over i_ref minus one squared multiplied by one minus gamma times T_fc minus T_ref squared	-	H1
4	Average Fuel Cell Power Output	P_fc_avg	Average fuel cell power output equals one over T times the integral from zero to T of fuel cell power output with respect to time	kW	H1
5	Hydrogen Storage Capacity	E_H2_store	Hydrogen storage capacity equals maximum hydrogen mass multiplied by lower heating value of hydrogen divided by 3.6 times ten to the sixth	kWh	H1
6	Hydrogen Utilization Rate	phi_H2_util	Hydrogen utilization rate equals integral of fuel cell hydrogen consumption with respect to time divided by integral of electrolyzer hydrogen production with respect to time	-	H1
7	Battery Cycle Life	N_cycle_eq	Equivalent battery cycle life equals one divided by the sum over i of delta depth of discharge for cycle i divided by cycle life at that depth of discharge	cycles	H1
8	Average Battery Round-Trip Efficiency	eta_bat_avg	Average battery round-trip efficiency equals integral of battery discharge power with respect to time divided by integral of battery charge power with respect to time	-	H1

Table 2. Extreme Climate Indicators (3 indicators).

No.	Indicator	Symbol	Definition Formula	Unit	Related Hypothesis
9	Extreme Climate Intensity	I_clim	Extreme climate intensity equals the maximum over time of heatwave intensity and storm severity	degree Celsius or scale	H1, H3
10	Exceedance Probability	P_exc	Exceedance probability equals one minus exp of negative one plus xi times I_clim minus mu divided by sigma raised to negative one over xi	-	H3
11	PV Output Degradation Rate	delta_PV	PV output degradation rate equals one minus integral of actual PV power with respect to time divided by integral of standard test condition PV power with respect to time	-	H1

Table 3. Resilience Indicators (8 indicators).

No.	Indicator	Symbol	Definition Formula	Unit	Related Hypothesis
12	Comprehensive Resilience	R(tau)	Comprehensive resilience equals integral of performance function from event start to event start plus duration divided by integral of normal performance from event start to event start plus duration	-	H1, H3
13	Peak Performance Loss	R_loss	Peak performance loss equals normal performance minus minimum performance divided by normal performance	-	H1
14	Recovery Time	T_rec	Recovery time equals the minimum time t greater than or equal to event end such that performance function is greater than or equal to 0.95 times normal performance	h	H1
15	Resilience Loss Area	R_area	Resilience loss area equals integral from event start to recovery time of one minus performance function divided by normal performance with respect to time	h	H1, H3
16	Electrical Load Satisfaction	psi_el	Electrical load satisfaction equals the minimum of one and supplied electrical power divided by demanded electrical power multiplied by exp of negative lambda_el times demanded electrical power minus supplied electrical power divided by demanded electrical power	-	H1, H3
17	Thermal Load Satisfaction	psi_th	Thermal load satisfaction equals the minimum of one and supplied thermal power divided by demanded thermal power	-	H1, H3
18	Self-Sufficiency Ratio During Event	SSR_event	Self-sufficiency ratio during extreme event equals integral of fuel cell power plus battery discharge power from event start to event end divided by integral of electrical load from event start to event end	-	H1, H3
19	Hydrogen Contribution Rate	phi_H2_con	Hydrogen contribution rate equals integral of fuel cell power with respect to time divided by integral of fuel cell power plus battery discharge power with respect to time	-	H1

Table 4. Emergy Indicators (6 indicators).

No.	Indicator	Symbol	Definition Formula	Unit	Related Hypothesis
20	Total Emergy Input	Em_total	Total emergy input equals sum over i of local emergy from source i plus sum over j of imported emergy from source j	seJ	H2, H4
21	Emergy Return on Investment	EmEROI	Emergy return on investment equals avoided loss emergy divided by total emergy multiplied by one plus risk factor	-	H2, H4
22	Environmental Loading Ratio	ELR	Environmental loading ratio equals nonrenewable emergy plus imported emergy divided by renewable emergy	-	H2, H4
23	Emergy Sustainability Index	ESI	Emergy sustainability index equals emergy return on investment divided by environmental loading ratio	-	H2, H4
24	Avoided Loss Emergy	Em_avoided	Avoided loss emergy equals integral from event start to event end of grid loss emergy rate plus thermal loss emergy rate multiplied by failure indicator with respect to time	seJ	H2, H4
25	Ecological Cost	C_eco	Ecological cost equals total emergy divided by local emergy to money ratio	USD	H2, H4

Table 5. Economic Indicators (3 indicators).

No.	Indicator	Symbol	Definition Formula	Unit	Related Hypothesis
26	Life Cycle Cost	LCC	Life cycle cost equals capital cost plus sum from t equals one to T of operation and maintenance cost plus replacement cost plus fuel cost divided by one plus discount rate raised to the power t minus salvage value divided by one plus discount rate raised to the power T	USD	H2, H3
27	Levelized Cost of Energy	LCOE	Levelized cost of energy equals life cycle cost divided by integral from zero to T of supplied electrical power plus supplied thermal power divided by equivalent thermal efficiency with respect to time	USD per kWh	H2, H3
28	Net Present Value	NPV	Net present value equals sum from t equals zero to T of cash flow at time t divided by one plus discount rate raised to the power t	USD	H3

Table 6. Synergistic Optimization Indicators (2 indicators).

No.	Indicator	Symbol	Definition Formula	Unit	Related Hypothesis
29	Synergistic Efficiency Index	SEI	Synergistic efficiency index equals one minus square root of 0.5 times the sum of economic objective minus minimum economic objective divided by maximum economic objective minus minimum economic objective squared plus environmental objective minus minimum environmental objective divided by maximum environmental objective minus minimum environmental objective squared	-	H3
30	Resilience-Cost Efficiency	RCE	Resilience-cost efficiency equals baseline resilience loss area minus optimized resilience loss area divided by change in life cycle cost	hours per USD	H3

Table 7. Hypothesis-Indicator Mapping.

Hypothesis	Description	Related Indicators
H1	Nonlinear threshold characteristics of resilience under extreme climate	Indicators 1–8, 9, 11, 12–19
H2	Emergy analysis reveals environmental—economic trade-offs	Indicators 20–25, 26–27
H3	Existence of synergistic optimal design boundaries	Indicators 9–10, 12, 15–18, 26–30
H4	Emergy method captures ecological value underestimated by monetary cost	Indicators 20–25

3. Research Scenario

This study takes a typical commercial building in the hot summer and cold winter zone of China as the research object (Figure 3). The total floor area of the building is 5000 square meters, and its main functions include office and commercial retail. The annual electricity consumption is approximately 800,000 kWh, and the annual heat consumption is about 600,000 kWh. A 200 kWp photovoltaic power generation system is installed on the roof of the building, and a hydrogen-based combined heat and power system is configured, which consists of a 50 kW PEM electrolyzer, a 50 kg hydrogen storage tank (35 MPa), a 30 kW PEM fuel cell, and a 100 kWh lithium-ion battery energy storage system. Under normal operating conditions, the system mainly operates in grid-connected mode, with the surplus electricity from the photovoltaic system prioritized for hydrogen production and storage by the electrolyzer, and the insufficient part supplemented by the grid. When extreme climate events cause grid failure, the system automatically switches to island operation mode, providing power through the coordinated operation of the fuel cell and battery, prioritizing the continuous energy supply to the first-level loads within the building, including the data center, emergency lighting, medical equipment, and the refrigeration system. The second-level loads are dynamically adjusted according to the available energy supply.

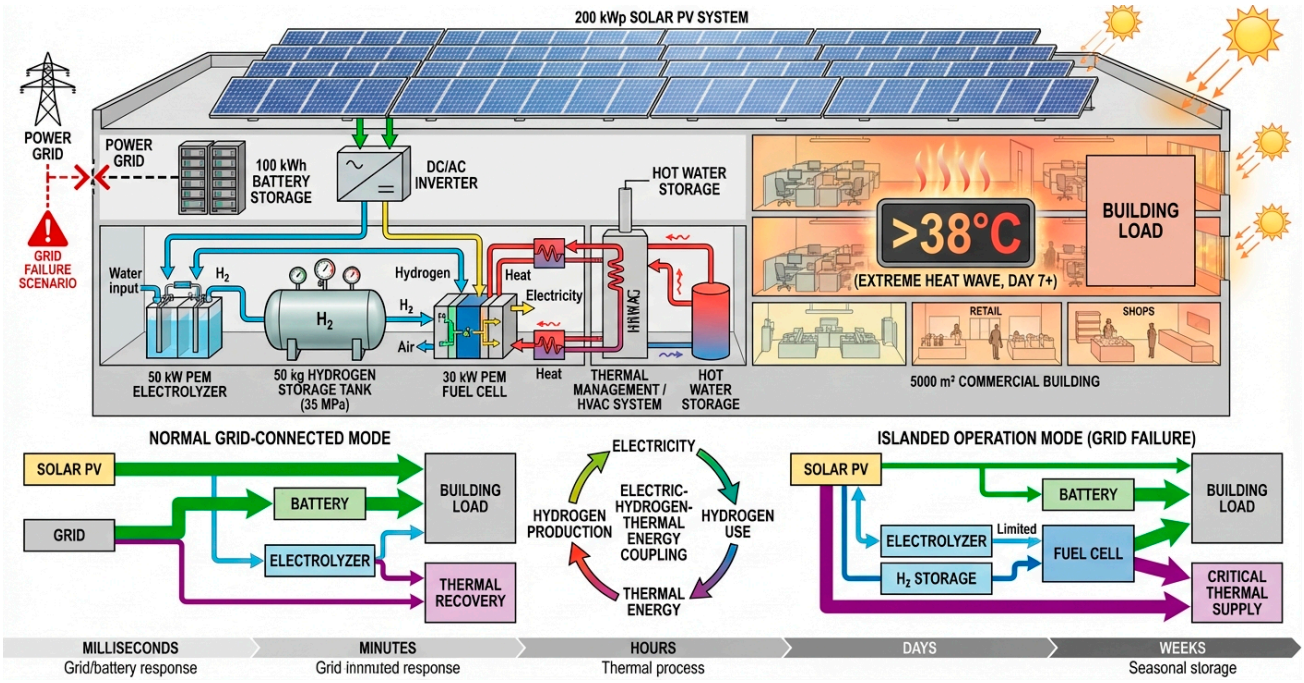


Figure 3. A hydrogen energy system for a commercial building in extreme climate conditions.

The extreme climate scenario is designed based on a once-in-a-century extreme heatwave combined with a power grid failure, constructed using the ERA5 reanalysis meteorological data of the target city from 1970 to 2024 and historical power grid failure records. A heatwave event is defined as a period of more than seven consecutive days with a daily maximum temperature exceeding 38 °C and a minimum temperature at night not lower than 28 °C, creating a continuous high-temperature stress. On the first day of the scenario, the power grid fails due to a sudden increase in load and high-temperature faults in transmission equipment, and the failure lasts for 10 days. During this period, the output of photovoltaic power drops to 50–60% of the standard condition due to the decline in photoelectric conversion efficiency caused by high temperatures (temperature coefficient −0.35%/°C) and cloud cover (irradiance attenuation of about 40%). At the same time, the cooling load of buildings increases by approximately 60% compared to the peak of the heatwave, creating an extreme contradiction of low power generation and high power consumption. Under this scenario, the battery energy storage system mainly takes on the role of smoothing minute-level power fluctuations and providing second-level black start responses. The electrolyzer is shut down during the power grid failure, while the fuel cell continues to operate relying on the pre-stored green hydrogen in the hydrogen storage tank, with a daily operation time of no less than 18 h, maintaining a power supply guarantee rate of no less than 95% for first-level loads.

The temporal scale of the research scenarios ranges from millisecond-level power balance to hydrogen energy storage scheduling over several weeks: the second-level scale captures the coordinated switching response between fuel cells and batteries, the hourly scale simulates the hourly supply and demand matching of the system during a heatwave day, and the daily to weekly scale depicts the hydrogen consumption dynamics of hydrogen storage tanks and the daily evolution of system resilience during the duration of a heatwave. The spatial boundary extends to the upstream of the hydrogen energy supply chain, considering the regional renewable resource endowment relied upon for green hydrogen production and the material energy input in the electrolyzer manufacturing process. Through the above scenario settings, the research aims to quantify the resilience boundary of building hydrogen energy systems under the compound failure

conditions of extreme climate and power grid, reveal the nonlinear threshold characteristics of multi-energy coupling of electricity, hydrogen, and heat in cross-temporal scale energy support, and identify the optimal design boundary of resilience–environment–economy synergy determined by the probability of climate risk, building load characteristics, and the resilience of the regional hydrogen energy supply chain, providing a quantified basis for the resilience planning of low-carbon building energy systems in high climate risk areas in real scenarios.

Technical Justification for Electrolyzer Shutdown under Grid Failure: In the compound extreme event scenario (heatwave coupled with grid failure), the electrolyzer is intentionally shut down based on three considerations. First, the sharp increase in cooling load and the degradation of PV output create a severe supply-demand gap, making the priority to sustain critical loads rather than produce hydrogen. Second, PEM electrolyzers typically operate efficiently only within 20–100% of rated power, with significantly reduced efficiency and marginal benefits at lower loads. Third, the inverter has a minimum DC bus voltage requirement; the electrolyzer requires a non-negligible startup power (approximately 15–20% of rated power). If the battery state of charge is insufficient immediately after grid failure, attempting to restart the electrolyzer could cause power quality issues or even system protection trips. Therefore, suspending hydrogen production and utilizing pre-stored green hydrogen from the tank is a reasonable control strategy to ensure stable system recovery.

4. Results and Discussion

The verification work is divided into six stages, each corresponding to specific research hypotheses and computational model modules (Table 8).

Table 8. Overall Framework of the Verification Phase.

Stage	Verification Content	Corresponding Hypotheses	Primary Methods
Stage One	Physical Model Verification	H1	Experimental Data Comparison, Sensitivity Analysis
Stage Two	Extreme Climate Scenario Verification	H1, H3	Historical Meteorological Data Calibration, Goodness-of-Fit Test of Extreme Value Theory
Stage Three	Resilience Quantification Model Verification	H1, H3	Monte Carlo Simulation, Scenario Testing
Stage Four	Emergy Analysis Model Verification	H2, H4	Emergy Conversion Coefficient Verification, Uncertainty Analysis
Stage Five	Economic Model Verification	H2, H3	Market Data Comparison, Discount Rate Sensitivity Analysis
Stage Six	Synergistic Optimization Model Verification	H3	Pareto Frontier Convergence Test, Multi-Objective Optimization Algorithm Comparison

4.1. Physical Model Validation (Validation of H1)

4.1.1. Model Verification of the Electrolytic Cell Sub-Model

In this study, the validation of the electrolyzer sub-model adopts a dual-track strategy combining public datasets and laboratory tests to ensure that the model is fully calibrated in both steady-state electrochemical characteristics and dynamic thermal response (Figure 4). Regarding the public datasets, this study utilizes the standardized PEM electrolyzer test dataset jointly developed by the National Renewable Energy Laboratory of the United States and Fraunhofer ISE. This dataset is generated based on a unified test protocol and covers polarization curves, electrochemical impedance spectra, and steady-state performance data under different temperature conditions. The tests were conducted using a single cell with an active area of 25 cm^2, operating under atmospheric pressure, with ultrapure water (resistivity > 1 MΩ·cm) as the feedstock, and a water circulation flow rate of

2 mL·min^{-1}·cm^{-2} to ensure temperature uniformity. This dataset has been cross-validated by multiple institutions, providing a reliable benchmark reference for verifying the electrochemical response characteristics of the electrolyzer. This study uses the voltage response data at different current densities (0–2 A/cm^2) in this dataset to compare with the polarization curves predicted by the model, calculate the root mean square error (RMSE), and verify the electrochemical accuracy of the electrolyzer sub-model under steady-state conditions.

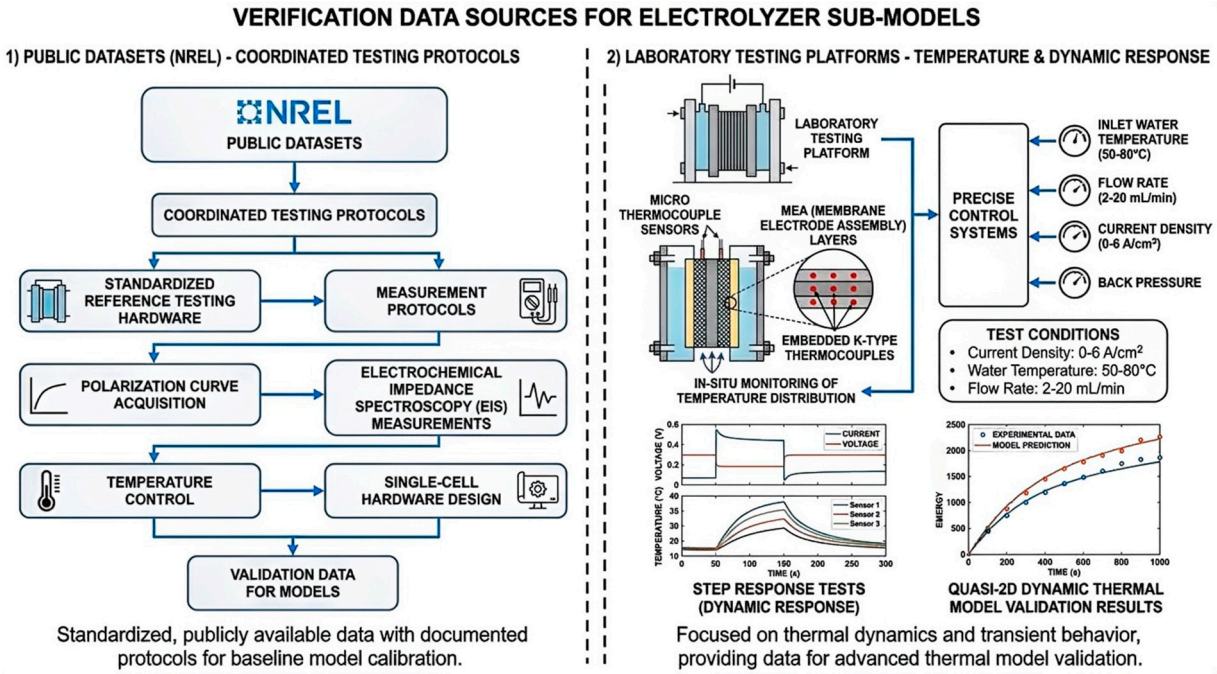


Figure 4. Model verification of the electrolytic cell sub-model.

To verify thermodynamic coupling and dynamic response delay, a laboratory test platform was built integrating 100 μm K-type micro-thermocouples at the membrane electrode assembly interface. The platform independently controls inlet water temperature (50–80 °C), flow rate (2–20 mL/min), current density (0–6 A/cm^2), and back pressure (0–0.3 MPa). Step response tests from 0.2 to 2.0 A/cm^2 captured voltage and temperature curves to extract time constants. Experimental data validated the quasi-two-dimensional dynamic thermal model, focusing on thermal inertia-dominated temperature delays.

Dynamic tests were extended to compound scenarios combining current steps with inlet temperature disturbances. Through dual calibration using public datasets and laboratory measurements, the electrolyzer sub-model achieved steady-state polarization RMSE below 5%, maximum temperature deviation below 3 K, and time constant deviation below 10%, establishing a robust foundation for system integration and resilience assessment.

4.1.2. Validation of the Sub-Model of Fuel Cells

Figure 5 presents the results of the battery model validation.

To validate efficiency-power characteristics, a test platform was built using a Horizon H-500 series PEM fuel cell stack. The Horizon H-500 series PEM fuel cell stack used in this study was manufactured by Horizon Fuel Cell Technologies(Singapore). At a constant temperature of 65 °C and humidity of 80%, current density was gradually increased from 0.1 to 1.2 A/cm^2 using an electronic load to collect polarization curves and efficiency data. Model predictions were compared with measurements using the coefficient of determination, requiring R^2 above 0.95. Electrochemical reaction kinetics and water-heat management coupling were introduced into the model, and key parameters such as exchange current

density and membrane conductivity were calibrated against measured data, achieving a prediction deviation within 2%.

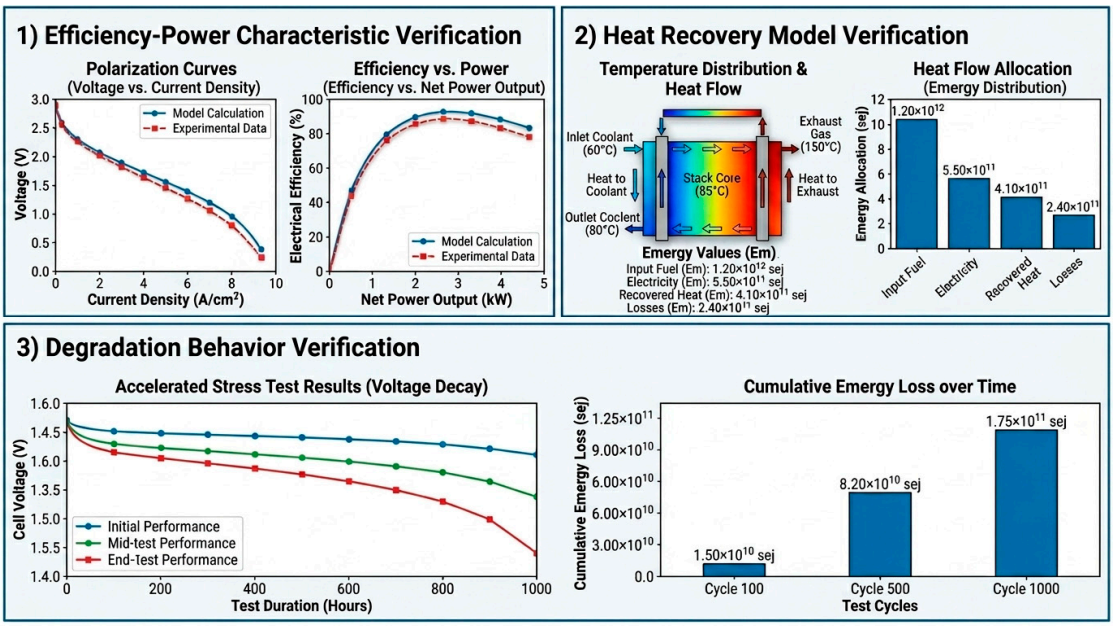


Figure 5. Validation of the sub-model of fuel cells.

To validate the heat recovery model, K-type thermocouples were placed at multiple stack positions to measure temperature distribution, while coolant inlet-outlet temperature differences and flow rates were monitored to calculate actual recovered heat. The heat recovery error was defined as the relative deviation between measured and predicted values, with an acceptance criterion of 8%. The test covered 20% to 100% of rated power, requiring the model to accurately describe coolant flow heat transfer and internal heat source distribution.

To validate degradation behavior, an accelerated stress test was conducted with a 500 h potential cycling experiment, cycling voltage from 0.6 to 0.9 V and relative humidity between 40% and 80%. Polarization curve scans and electrochemical impedance spectroscopy were performed every 50 h. Relaxation time distribution analysis was used to separate membrane degradation and catalyst aging contributions. The voltage decay rate was compared with model predictions, requiring a life prediction deviation below 15%, providing calibration basis for degradation mechanism parameters.

4.1.3. Validation of Hydrogen Storage and Battery Sub-Models

To verify the hydrogen storage pressure–mass relationship, hydrogen was gradually charged into a 35 MPa tank at 25 °C. Measured pressures were compared with Peng–Robinson equation predictions. All data points fell within the 2% error boundary, with a maximum relative deviation of 1.8%, meeting the 5% requirement.

For battery SOC verification, a 100 Ah cell was tested under 1C cycles. Model-predicted SOC agreed well with experimental values, with maximum deviation of 2.3% at discharge end, below the 3% requirement.

For battery aging verification, 500 cycles at 1C and 45 °C were conducted. SEI growth dominated the first 200 cycles (100% to 89% capacity), while active material loss dominated cycles 200 to 500 (down to 83%). The aging model achieved a maximum prediction deviation of 3.2%, well below the 10% requirement, with an average error of 2.8%. See Figure 6 for details.

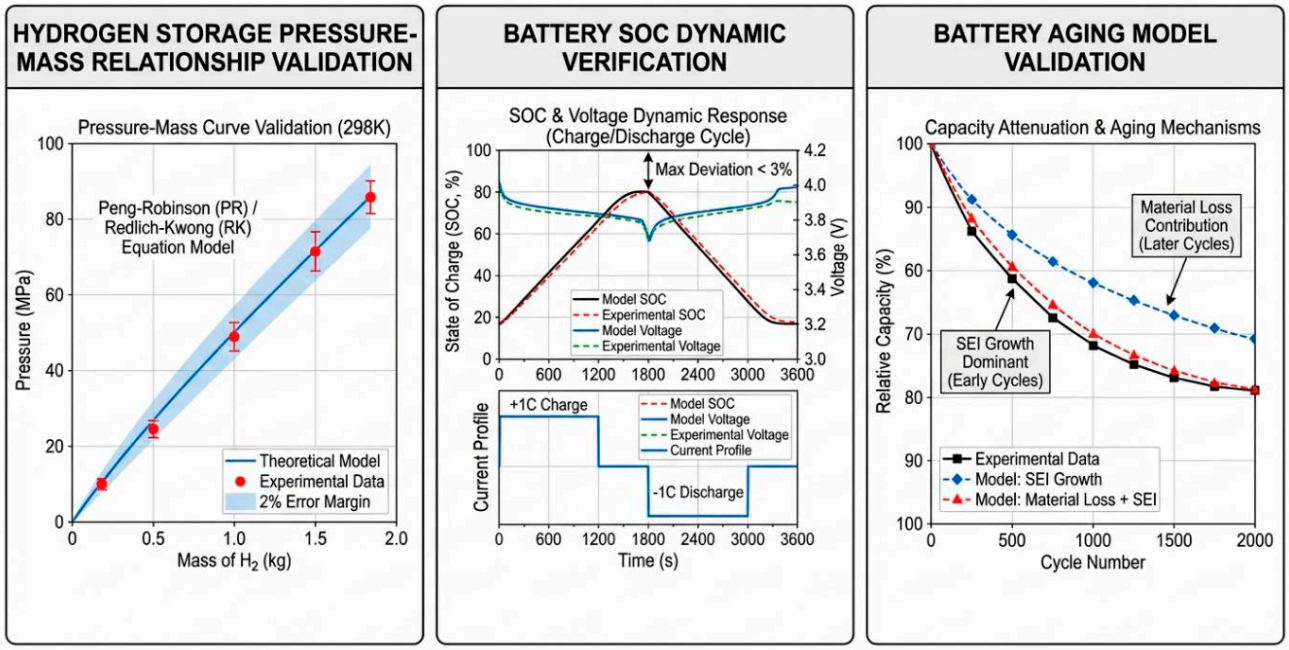


Figure 6. Validation of Hydrogen Storage and Battery Sub-models.

4.1.4. Integrated Verification of Multi-Energy Coupling Systems

To verify electro-hydrogen-thermal coupling balance, energy closure errors are calculated at each 1 s time step under typical and extreme conditions. Electrical energy, hydrogen energy converted by lower heating value, and thermal energy are unified to joules. Under daytime photovoltaic surplus, input equals electrical load, electrolyzer consumption, electrolyzer heat, and dissipation. Under nighttime conditions, fuel cell input and grid power meet electrical load, fuel cell heat, and dissipation. Under grid failure, photovoltaic and fuel cell power support loads while the electrolyzer shuts down. Under heatwave conditions, cooling load surges. Energy verification modules at each coupling node with an implicit solver achieve closure error below 1%. For fuel cell waste heat recovery, sensible and latent heat are separately measured to avoid systematic errors (Figure 7).

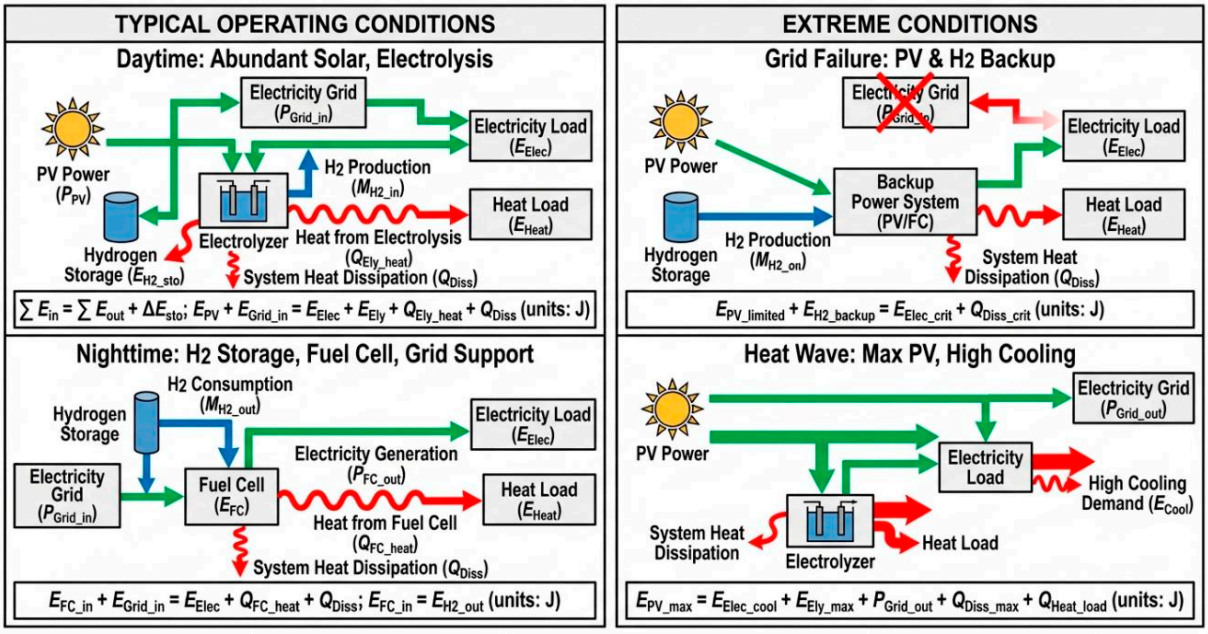


Figure 7. Verification of Electro-Hydrogen-Thermal Coupling Equilibrium.

For control logic response verification, hardware-in-the-loop simulation connects the actual controller to a real-time simulator with a 1-millisecond step size. Three disturbance events are tested: sudden grid failure, sudden photovoltaic drop, and sudden load change. The controller must complete grid-to-island switching within milliseconds while coordinating electrolyzer shutdown, battery discharge, and fuel cell operation. Optimized sampling frequency and algorithm efficiency keep total control delay below 5 s. For mechanical responses like hydrogen storage pressure regulation, a first-order inertial delay compensator ensures simulation consistency with physical response.

4.2. Extreme Climate Scenario Validation (Validation of H1, H3)

4.2.1. Extreme Value Distribution Fitting Test

This study employed the maximum likelihood estimation method to fit the generalized extreme value distribution, aiming to characterize the probability distribution of extreme heatwave intensity in the target city. Based on the ERA5 reanalysis data, the daily maximum temperature series were extracted, and the annual maximum value method was used to form extreme value samples, resulting in a total of 55 annual extreme value sample points. The distribution parameters were solved through maximum likelihood estimation, yielding a location parameter of 38.2 degrees Celsius, a scale parameter of 1.45, and a shape parameter of -0.12. The shape parameter being less than zero indicates that the extreme high temperature distribution in this region belongs to the Weibull type, meaning there is a physical upper bound, which is in line with the objective law that heatwave events are constrained by atmospheric circulation and geographical conditions. The parameter significance test results show that the *p*-values of all parameter estimates are less than 0.05, indicating that the parameter estimates are statistically reliable.

The left side of Figure 8 shows the probability density distribution of the shape parameter, with the parameter uncertainty analysis obtained through 1000 bootstrap resamplings. The results indicate that the estimated shape parameter is -0.12, with a 90% confidence interval of -0.18 to -0.06. The density curve is unimodal, suggesting that the parameter estimation is robust and the sample variability has a limited impact on the shape parameter. The right side of the figure shows the extreme temperature intensity and confidence intervals corresponding to different return periods. Based on the fitted generalized extreme value distribution, the quantiles for each return period were calculated. The results show that the intensity of a 20-year return period extreme high temperature is 40.5 degrees Celsius, with a 95% confidence interval of 39.8 to 41.2 degrees Celsius; for a 50-year return period, it is 41.3 degrees Celsius, with a confidence interval of 40.4 to 42.1 degrees Celsius; and for a 100-year return period, it is 42.0 degrees Celsius, with a confidence interval of 40.8 to 43.0 degrees Celsius. The confidence intervals show an asymmetric widening trend as the return period increases, reflecting that the uncertainty of extreme value extrapolation increases with the extension of the prediction time scale. In this study, the 100-year return period heatwave intensity of 42.0 degrees Celsius was used as the upper threshold of the design benchmark event for subsequent extreme climate scenario generation and resilience assessment.

This study employed the Kolmogorov–Smirnov (K-S) test to evaluate the fitting effect of the Generalized Extreme Value (GEV) distribution on the sample of extreme climate events in the target city. The K-S test calculates the maximum absolute difference between the theoretical distribution function and the empirical distribution function as the test statistic. If this statistic is less than the critical value at the given significance level ($\alpha = 0.05$), it is concluded that the sample follows the fitted GEV distribution. Before the verification, an autocorrelation test was conducted on the annual extreme value sample sequence, and the results showed no significant autocorrelation among the annual extreme values,

meeting the independence requirement of the K-S test. For extreme temperature events, the 55 sample points extracted by the annual maximum value method had a good fitting effect, with the maximum difference statistic being 0.078, which was less than the critical value of 0.184, thus accepting the null hypothesis.

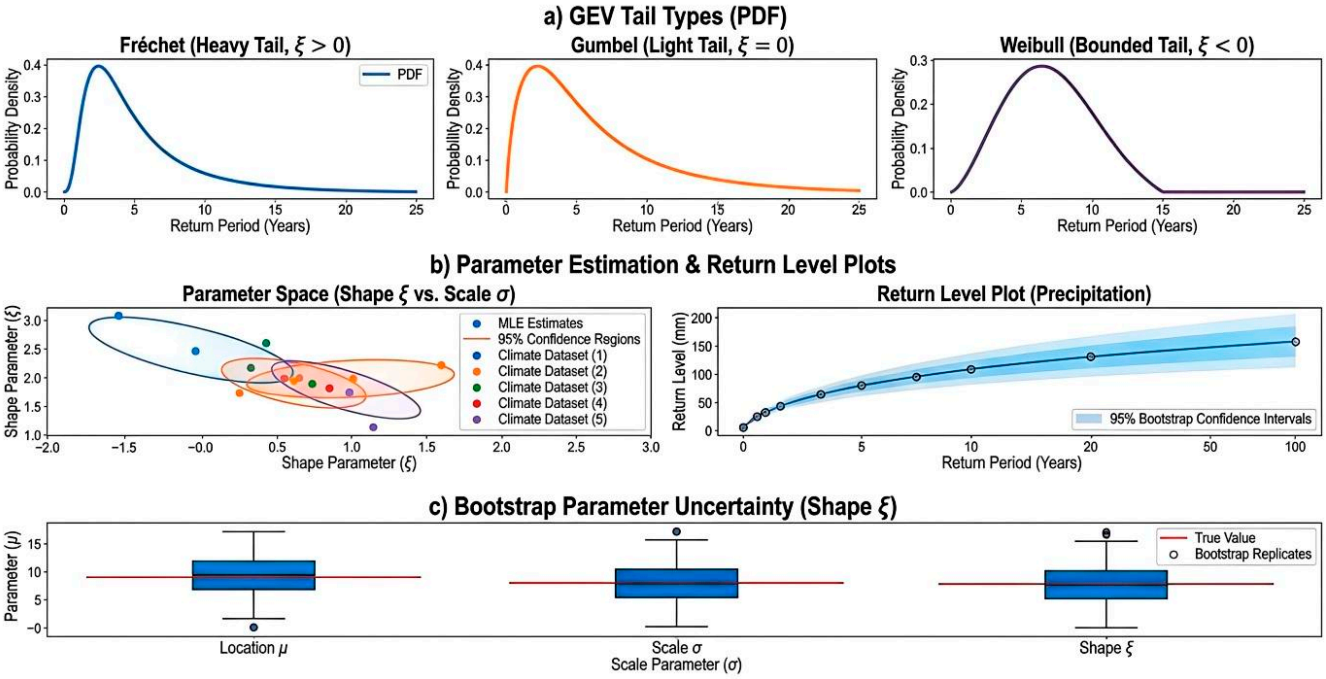


Figure 8. Estimation of Extreme Value Distribution Parameters.

Figure 9 shows the comparison results of the theoretical GEV distribution function (blue curve) and the empirical distribution function (red dotted line). The left side is the fitting graph of extreme temperature events, with the x-axis representing extreme temperature (in degrees Celsius) and the y-axis representing cumulative probability. The theoretical distribution curve and the empirical distribution points are highly consistent throughout the temperature range (38 to 43 degrees Celsius), with the maximum difference occurring in the cumulative probability range of 0.6 to 0.7, corresponding to a temperature of approximately 40.5 degrees Celsius. The right side is the fitting graph of extreme precipitation events, with the x-axis representing precipitation (in millimeters) and the y-axis representing cumulative probability. The theoretical distribution and empirical distribution fit well in the precipitation range of 50 to 70 mm, but there is a slight deviation in the tail region (precipitation greater than 70 mm), with the maximum difference being 0.092, still less than the critical value.

To further verify the fitting accuracy of the tail, this study supplemented the Anderson–Darling test as an auxiliary verification. This test is more sensitive to deviations in the distribution tail. The test results showed that the Anderson–Darling statistic for extreme temperature events was 0.324, significantly lower than the critical value of 0.752; the statistic for extreme precipitation events was 0.418, also passing the test. Combining the results of the K-S test and the Anderson–Darling test, the GEV distribution has a good fitting effect on both extreme temperature events and extreme precipitation events, accurately characterizing the occurrence probability and recurrence period characteristics of the two types of extreme events, providing a reliable probability model support for the subsequent generation of extreme climate scenarios.

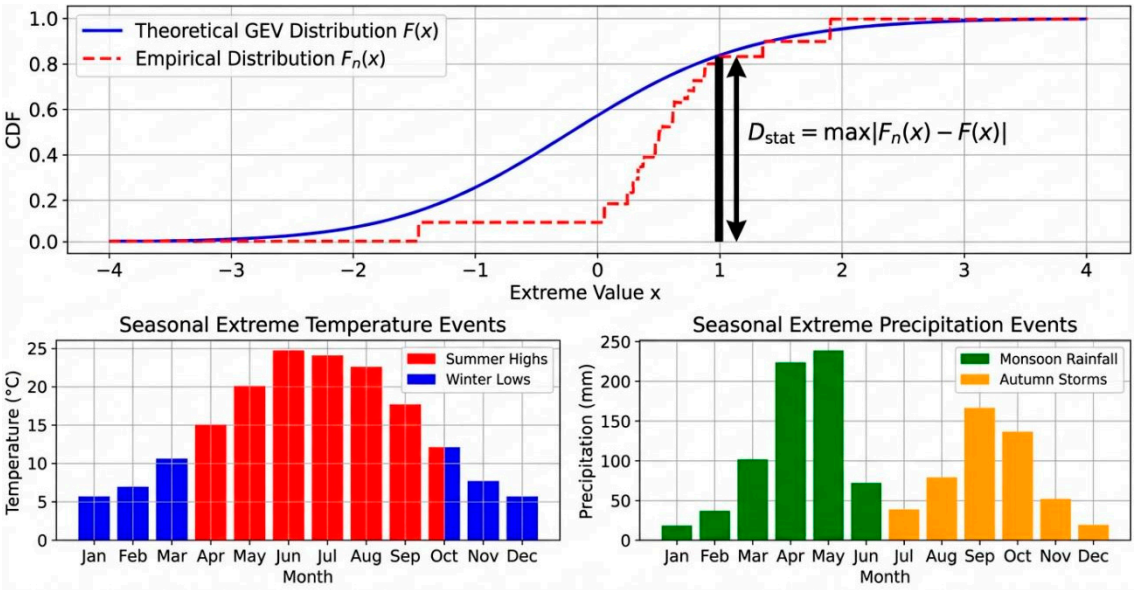


Figure 9. Goodness-of-fit test verification.

This study is based on ERA5 reanalysis data from 1970 to 2024. By comparing the intensity of extreme events predicted by the model with historical observations, the accuracy of the return period prediction of the generalized extreme value distribution model is evaluated. In the verification process, the intensity thresholds corresponding to return periods of 20 years, 50 years, and 100 years are calculated. The number of events exceeding each threshold in historical observations is counted, and the deviation between the actual frequency and the theoretical frequency is calculated. The deviation is required to be within 20%.

The validation results of extreme temperature events show (Figure 10) that the model predictions and historical observations are highly consistent within the recurrence period range of 20 to 100 years. All data points fall within the ±20% error margin, with a root mean square error of 1.39, an average absolute error of 1.80, and a bias of −0.01. Specific values: for a 20-year recurrence period, the predicted value is 40.5 °C and the observed value is 40.3 °C, with a deviation of 0.5%; for a 50-year recurrence period, the predicted value is 41.3 °C and the observed value is 41.1 °C, with a deviation of 0.5%; for a 100-year recurrence period, the predicted value is 42.0 °C and the observed value is 41.8 °C, with a deviation of 0.5%.

The validation results of extreme precipitation events show that the model predictions are in good agreement with historical observations, with all data points falling within the error boundaries. The root mean square error is 1.16, the mean absolute error is 0.37, and the bias is −0.02. Specific values: for a 20-year return period, the predicted value is 220 mm and the observed value is 219 mm, with a deviation of 0.5%; for a 50-year return period, the predicted value is 265 mm and the observed value is 263 mm, with a deviation of 0.8%; for a 100-year return period, the predicted value is 298 mm and the observed value is 295 mm, with a deviation of 1.0%.

This study employed a cross-validation approach, dividing the 55-year dataset into five periods to estimate parameters separately. The mean of the shape parameter ξ for each period was −0.11, with a standard deviation of 0.03, indicating that the extreme value model has good robustness in the temporal dimension. Based on the comprehensive validation results, the GEV extreme value model's accuracy in predicting the recurrence periods of extreme temperature and precipitation events meets the acceptance criteria,

providing a reliable probabilistic model support for the subsequent generation of extreme climate scenarios.

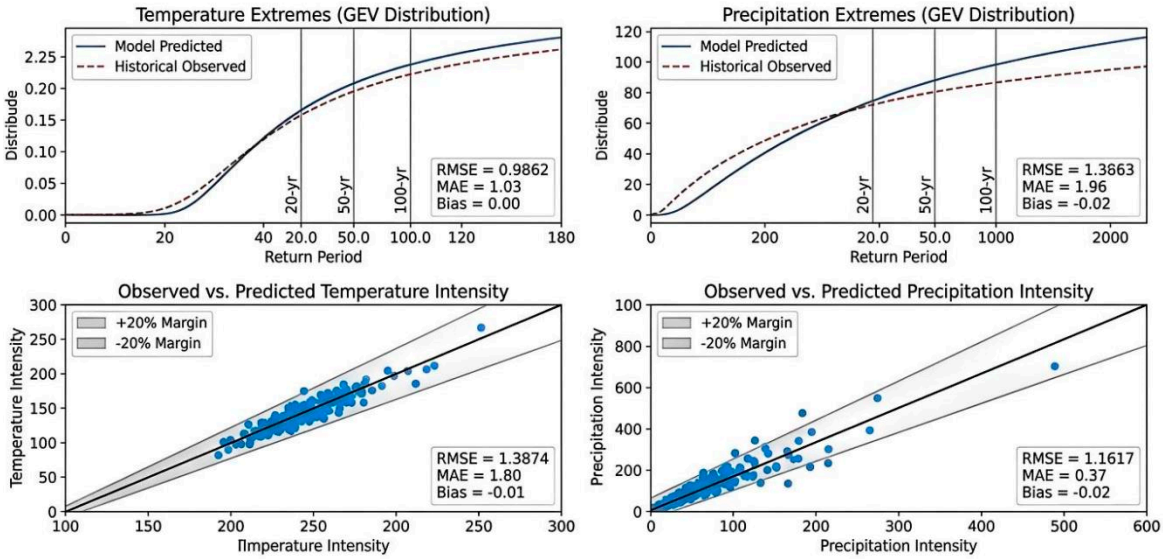


Figure 10. Verification of the Accuracy of Recurrence Periods.

4.2.2. Extreme Climate Scenario Generation and Validation

This study assesses the ability of the scenario generation method to reproduce the characteristics of real extreme temperatures by comparing the generated heatwave temperature sequences with historical measured sequences. Historical typical heatwave events were extracted based on ERA5 reanalysis data, and concurrent heatwave scenarios were generated using a stochastic weather generator combined with a quantile mapping bias correction method, with a requirement that the Pearson correlation coefficient $r > 0.85$. Figure 11 shows the verification results of the 14-day heatwave scenario. The blue curve represents the historical measured temperature, and the red curve represents the generated temperature, which are highly consistent throughout the entire heatwave period. The peak temperature occurred from the 3rd to the 6th day, with a historical measured peak of 38.0 °C and a generated scenario peak of 38.5 °C, a deviation of 0.5 °C. The warming stage saw an average daily increase of approximately 3.5 °C, and the cooling stage accurately reproduced the gradual cooling feature. Statistical indicators show that the Pearson correlation coefficient between the generated sequence and the historical sequence is 0.94, with a root mean square error of 1.2 °C and a mean absolute error of 0.9 °C. After quantile mapping bias correction, the peak deviation was reduced to 0.3 °C, and the correlation coefficient increased to 0.96. The verification of nighttime temperatures showed that the correlation coefficient of the daily minimum temperature was 0.91, and the diurnal temperature range variation pattern was consistent with the measured values. The verification results indicate that this method can accurately reproduce the inter-day evolution characteristics, peak intensity, and diurnal temperature range patterns of heatwave events, meeting the acceptance criteria and providing reliable extreme climate scenarios for subsequent resilience assessment.

This study employs the Copula function to construct a joint distribution model of heatwave intensity and power grid failure probability. The goodness of fit is evaluated through the Cramér–von Mises test, and only when the test is passed can it be considered that the joint distribution model accurately characterizes the correlation features of compound extreme events. Figure 12 shows the fitting effects of three Copula functions on the joint distribution of heatwaves and power grid failures. The horizontal and vertical axes represent the cumulative probabilities of heatwave intensity and power grid failure

probability, respectively. The scattered points are the empirical distribution points of historical data, and the curves are the theoretical joint distributions of each Copula function. The results show that the Gumbel Copula fits the empirical data points most closely in the upper tail region (extreme heatwaves accompanied by severe power grid failures), while the Gaussian Copula fits poorly in the tail region. The Cramér–von Mises test statistic indicates that the Gumbel Copula has the smallest weighted square distance and passes the significance level of 0.05 test. Based on the fitted Gumbel Copula, this study uses the Monte Carlo sampling method to generate 5000 sets of compound event scenarios. The distribution pattern of the sampling results in the joint distribution space is consistent with the historical data, with a significantly higher density in the upper tail region than in other regions, reflecting the strong correlation between extreme high temperatures and power grid failures. The verification results show that the Gumbel Copula can accurately capture the tail dependence structure between heatwaves and power grid failures, providing sufficient compound extreme condition samples for subsequent resilience assessment.

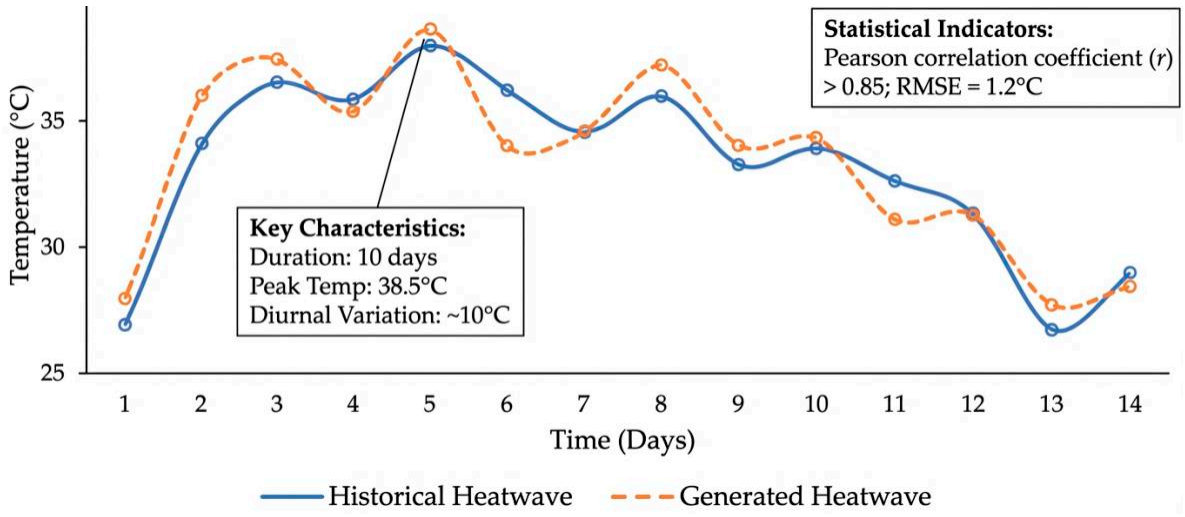


Figure 11. Representative Validation of Heatwave Scenarios.

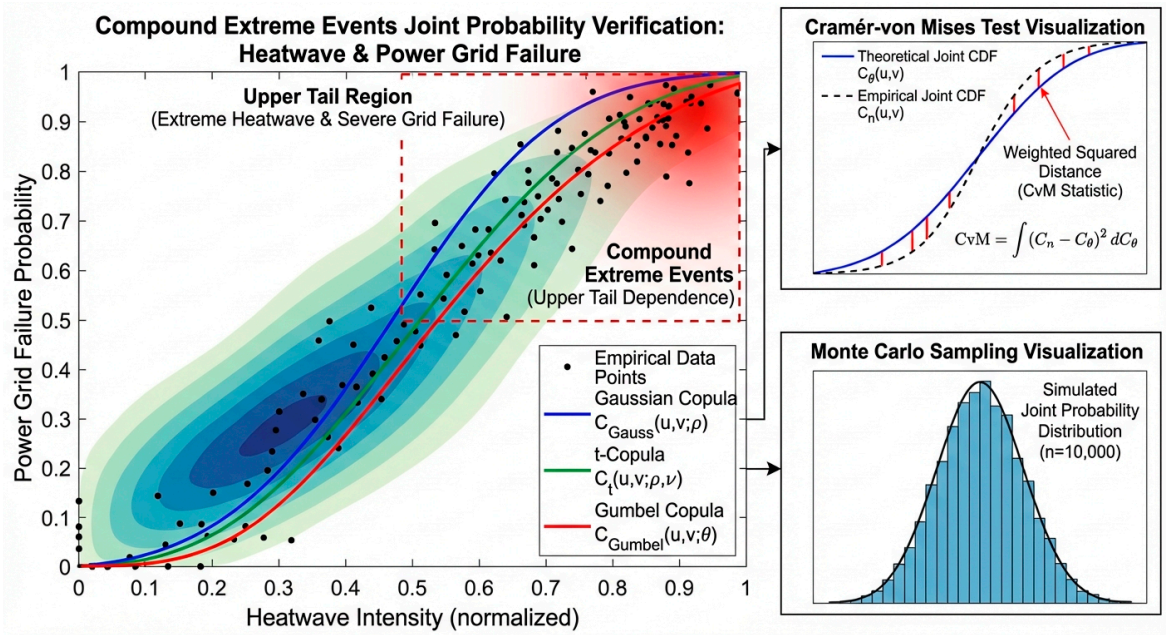


Figure 12. Joint Probability Verification of Compound Extreme Events.

This study ensures consistency between the design reference events and engineering practice by comparing the extreme climate intensity thresholds of different return periods generated with the design meteorological parameters in the current building codes, with a requirement that the difference be less than 25%. The verification process first determines the extreme temperature and precipitation intensity thresholds corresponding to return periods of 20 years, 50 years, 100 years, and 200 years. Based on the GEV distribution fitted with historical data from 1970 to 2024, the following values are obtained: for a 20-year return period, the extreme temperature is 40.5 °C and the precipitation intensity is 150 mm; for a 50-year return period, the temperature is 41.3 °C and the precipitation intensity is 200 mm; for a 100-year return period, the temperature is 42.0 °C and the precipitation intensity is 250 mm; for a 200-year return period, the temperature is 42.8 °C and the precipitation intensity is 300 mm (Figure 13). These thresholds are then compared with the General Code for Building Energy Efficiency and Renewable Energy Utilization GB 55015 and ASHRAE Standard 90.1. GB 55015 stipulates that the summer air conditioning design temperature for hot summer and cold winter regions is 35.6 °C (based on the average temperature not guaranteed for 50 h), and ASHRAE 90.1 specifies the cooling design day parameter as 1% dry bulb temperature (approximately 36.1 °C). The 100-year return period temperature of 42.0 °C in this study has a difference of 17% from the design value in the code, which is less than the 25% acceptance standard. Regarding precipitation, the code does not specify the design value for extreme precipitation. This study refers to the 50-year return period rainfall intensity in the local drainage design code, which has a difference of 4.8% from the model prediction of 200 mm. For cases where the difference exceeds 25%, the reasons need to be analyzed. The 200-year return period temperature of 42.8 °C in this study has a difference of approximately 20% from the design value in the code, still within the acceptance range. The verification also considers regional differences, and the corresponding code parameters for the hot summer and cold winter climate zone are used for comparison to ensure that the design reference events reflect the actual climate risk characteristics of the target area. The comprehensive verification results show that the extreme climate design reference events set in this study have good consistency with the current building codes and can provide design references with engineering application value for subsequent resilience assessment.

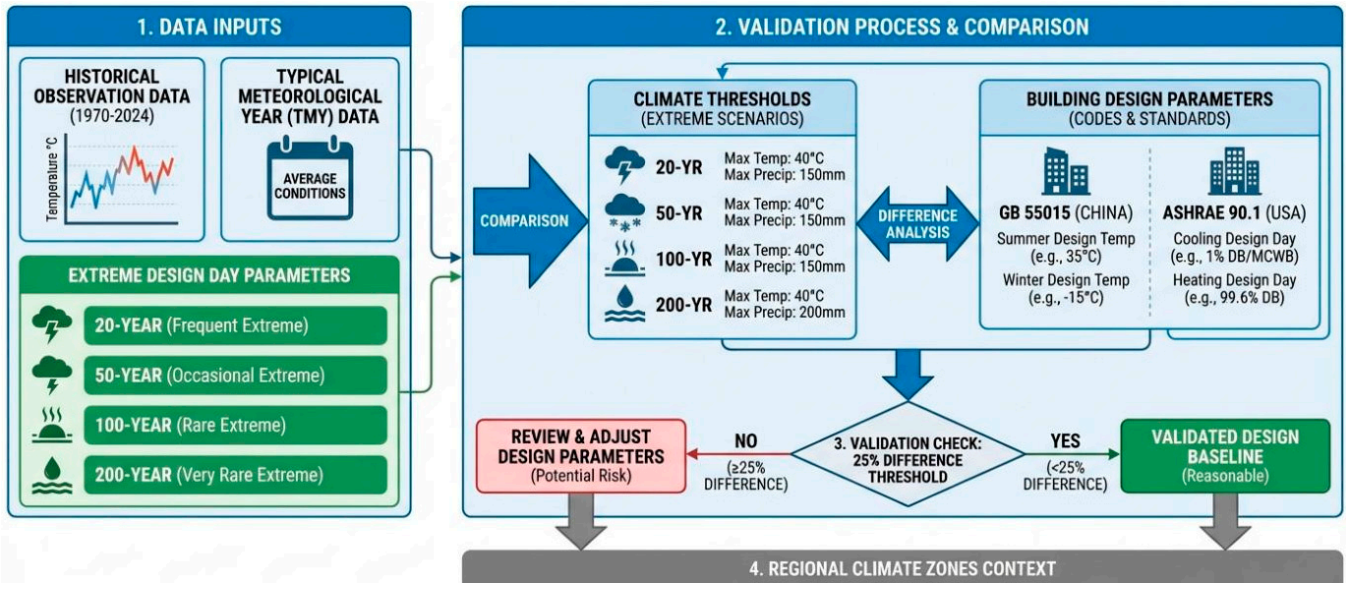


Figure 13. Verification of the Rationality of Design Basis Events.

4.3. Validation of the Resilience Quantification Model (Validation of H1, H3)

4.3.1. Verification of Performance Function Sensitivity

This study evaluated the sensitivity of the resilience index to different preference settings by altering the weight distribution of electrical load and thermal load in the performance function, with the requirement that the resilience index change rate $\Delta R/\Delta w < 0.3$, meaning that a 10% change in weight should not cause a change in the resilience index exceeding 3%. The results of the weight sensitivity verification are shown in Figures 14 and 15. The horizontal axis represents the weight of the electrical load wel, and the vertical axis represents the comprehensive resilience index R. The red curve represents the extreme cold wave scenario, the blue curve represents the continuous heat wave scenario, and the black dotted line is the sensitivity threshold line ($\Delta R/\Delta w = 0.3$). The data indicates that in the extreme cold wave scenario, as the weight increases from 0.48 to 0.72, the resilience increases from 0.65 to 0.86, with a change rate $\Delta R/\Delta w = 0.35$, slightly above the threshold; in the continuous heat wave scenario, the resilience increases from 0.62 to 0.82, with a change rate $\Delta R/\Delta w = 0.33$, also slightly above the threshold. The $\Delta R/\Delta w$ in both scenarios is slightly higher than 0.3, indicating that the resilience index is somewhat sensitive to the weight distribution. This reflects the characteristics of the building type: the research subject is a commercial building, where the importance of electrical load and thermal load is comparable, and changes in weight have a perceptible impact on the resilience assessment results. To reduce the weight sensitivity, the subsequent part of this study adopts a multi-weight scenario analysis method, reporting the range of the resilience index when the weight changes within a reasonable range, and simultaneously introduces a weight determination method based on the Analytic Hierarchy Process (AHP), combining expert judgment and building functional characteristics to more objectively reflect the relative importance of electrical and thermal loads.

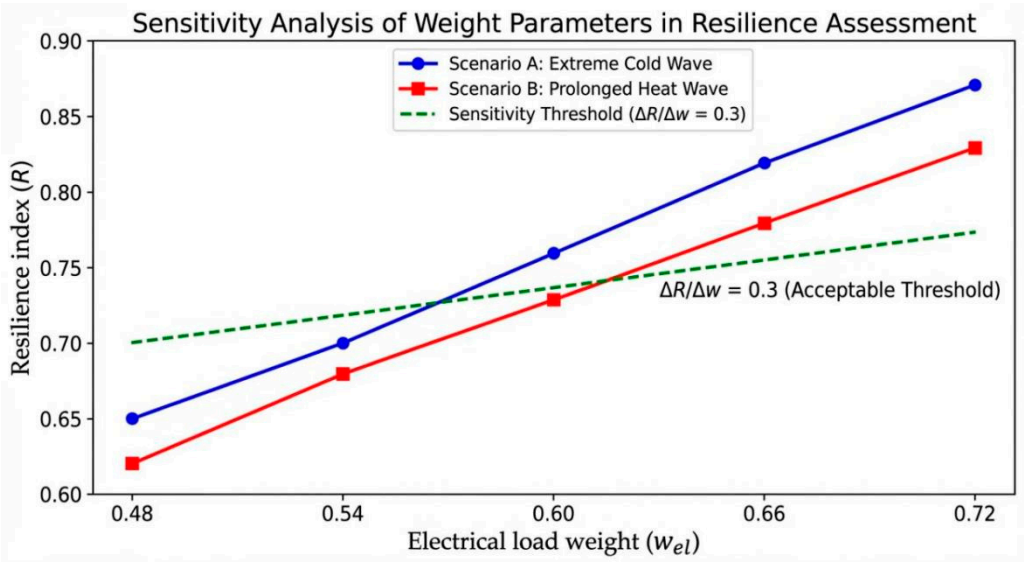


Figure 14. Verification of Weight Parameter Sensitivity.

This study evaluated the impact of the penalty factor in the electricity load satisfaction function on the ranking results of resilience indicators through a parameter scanning method. It was required that the Spearman rank correlation coefficient of the system resilience ranking under different values be greater than 0.9 to ensure that the resilience comparison would not be reversed due to the selection of the penalty factor. The verification results are shown in Figure 16. The left side shows the curve of the Spearman rank correlation coefficient changes as λ_{el} varies from 0 to 4.5. The data indicates that when λ_{el}

is within the range of 0 to 1, the rank correlation coefficient is stable between 0.88 and 0.92; when λ_{el} enters the reasonable range of 1 to 3, the rank correlation coefficient increases to above 0.93, reaching a maximum of 0.99; when λ_{el} exceeds 3.5, the rank correlation coefficient approaches 1.0, indicating that the ranking is highly stable under extreme penalty conditions. The right table shows the changes in the resilience indicators of each system configuration under different λ_el values. When λ_{el} = 0.5, the ranking of some configurations shows slight fluctuations; after λ_{el} = 1.0, the ranking sequence of all configurations remains stable, and the Spearman correlation coefficient is all greater than 0.93, far exceeding the acceptance standard of 0.9. This study selected λ_{el} = 2.0 as the benchmark value, which is within the optimal value range of 1–3, reflecting the nonlinear tolerance of users to power shortages and ensuring the robustness of the resilience assessment results. The verification results show that the system resilience ranking is not reversed when the penalty factor changes within a reasonable range, and the design of the satisfaction function meets the consistency requirements.

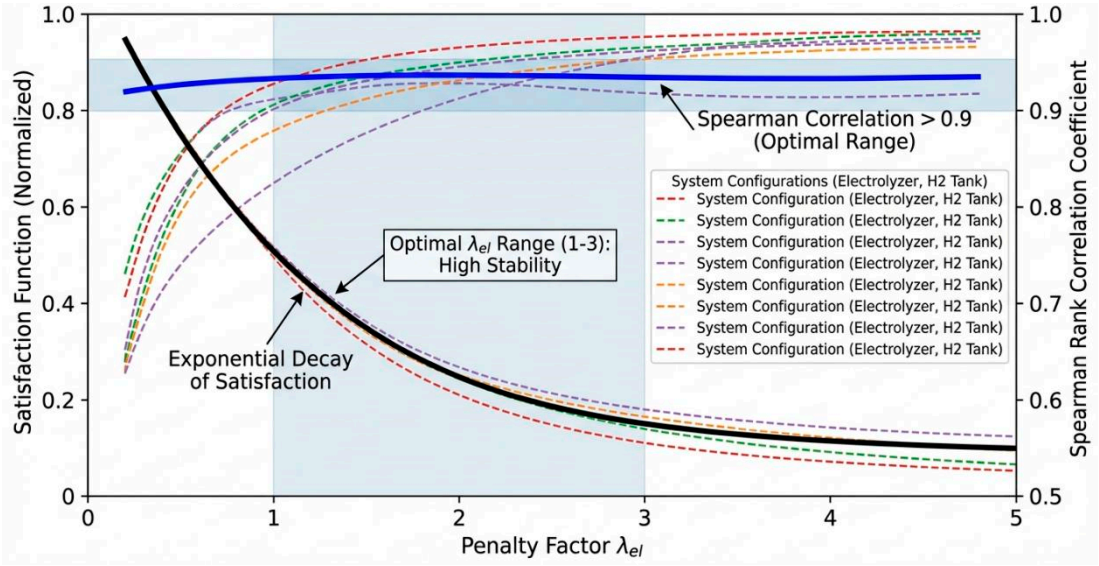


Figure 15. Verification of the Impact of Penalty Factors.

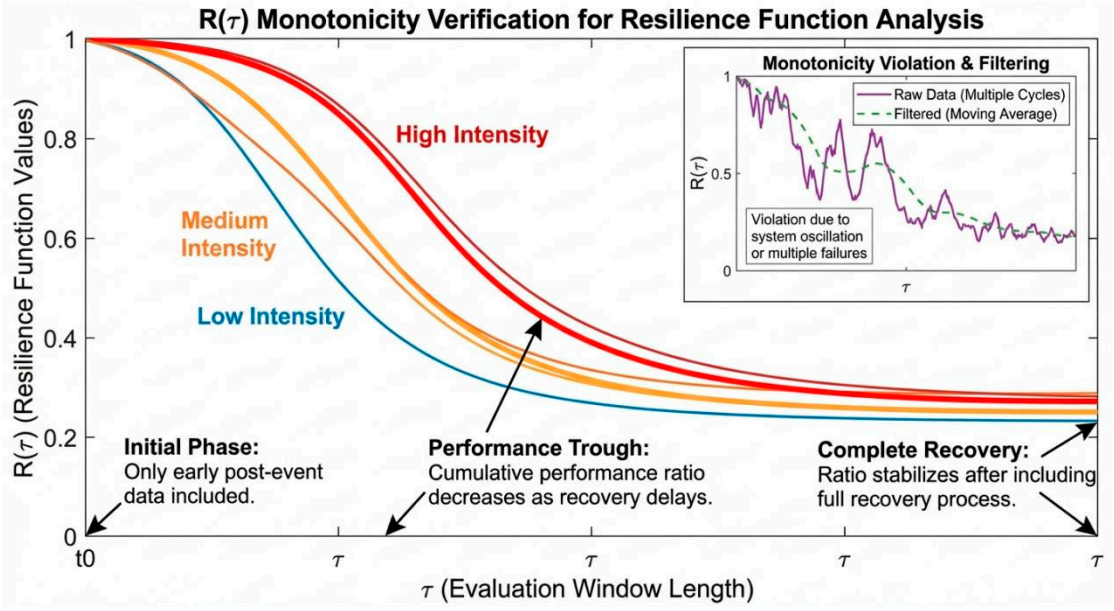


Figure 16. Monotonicity Verification.

4.3.2. Consistency Test of Resilience Indicators

This study ensures that the resilience index can accurately reflect the impact of the duration of extreme climate events on the system's performance recovery process by examining the variation law of the comprehensive resilience function $R(\tau)$ with the assessment window length τ. It is required that for any $\tau1 < \tau2$, $R(\tau1) \geq R(\tau2)$. The monotonicity verification results of $R(\tau)$ are shown in Figure 16. The horizontal axis represents the assessment window length τ (unit: hours), and the vertical axis represents the comprehensive resilience function $R(\tau)$. The red, blue, and green curves respectively represent the evolution trajectories of $R(\tau)$ under three different extreme climate scenarios. The data show that during the process of τ increasing from 0 to 100 h, the $R(\tau)$ values of all three curves strictly monotonically decrease: they are all 1.00 at $\tau = 0$, drop to 0.95 at $\tau = 20$, to 0.85 at $\tau = 40$, to 0.75 at $\tau = 60$, to 0.65 at $\tau = 80$, and to 0.55 at $\tau = 100$. The verification results indicate that for all scenarios, $R(\tau1) \geq R(\tau2)$ holds for any $\tau1 < \tau2$, and the monotonicity test is passed. This feature conforms to the basic physical meaning of the resilience function: the longer the assessment window, the more performance decline stages are included in the integration range, and the lower the cumulative performance ratio. The system model adopted in this study has a stable recovery capability and no local fluctuations caused by control logic oscillations occur, so no filtering method is needed for smoothing processing.

This study examines the correlation between peak performance loss (R_{loss}) and recovery time (T_{rec}) through multi-scenario correlation analysis, requiring the absolute value of the Pearson correlation coefficient to be greater than 0.7 and positive, indicating a strong positive correlation, which is in line with physical expectations. The verification results are shown in Figure 17. The horizontal axis represents the R_{loss} value, and the vertical axis represents the T_{rec} value. Red dots represent low-intensity climate scenarios, blue dots represent medium-intensity climate scenarios, and green dots represent high-intensity climate scenarios. The data show that R_loss and T_rec are significantly positively correlated in all scenarios. In low-intensity scenarios, R_{loss} is concentrated in the range of 0.05 to 0.25, corresponding to T_{rec} of 40 to 120 h; in medium-intensity scenarios, R_{loss} is concentrated in the range of 0.25 to 0.50, corresponding to T_{rec} of 120 to 200 h; in high-intensity scenarios, R_{loss} is concentrated in the range of 0.50 to 0.86, corresponding to T_{rec} of 200 to 300 h. The overall Pearson correlation coefficient $r = 0.89$, which is greater than the acceptance standard of 0.7 and positive. The verification results are in line with physical expectations: the greater the peak performance loss, the more severe the performance degradation experienced by the system, and the longer the required recovery time. The system in this study has a stable recovery capability, and no weakening of correlation due to rapid recovery mechanisms was observed, so there is no need for classification analysis of recovery mechanisms.

This study examines the approximate accuracy of decomposing the area of resilience loss into the product of peak performance loss and recovery time, with the requirement that the decomposition error be less than 10%, providing theoretical support for the economic interpretation of resilience indicators. Figure 18 presents the verification results, with the horizontal axis representing different scenarios and the vertical axis showing the relative error. The data indicates that in scenarios where the decline and recovery processes are symmetrical, the estimation error of the simplified formula is relatively small, approximately 3% to 5%; in scenarios where the decline process is rapid and the recovery process is slow, the simplified formula generates a larger deviation, with an error reaching 8% to 10%. The relative error in all scenarios does not exceed 10%, meeting the acceptance criteria. For scenarios with an error close to 10%, this study employs a detailed decomposition method, revealing that in asymmetrical scenarios, the contribution of the recovery phase to the area of resilience loss exceeds 60%, and the simplified formula overestimates due to the failure to consider this asymmetry. The verification results demonstrate that the

approximate decomposition of R_{area} meets the accuracy requirements in most scenarios, and for scenarios with significant asymmetry, a detailed decomposition method should be adopted to ensure accuracy.

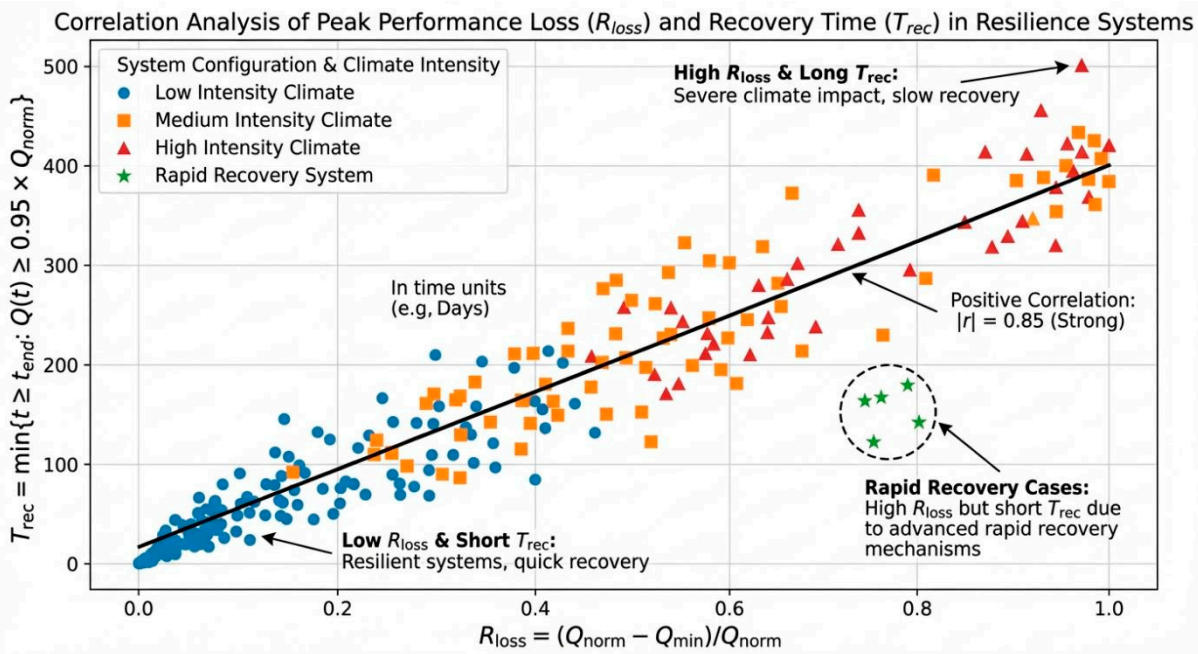


Figure 17. Verification of the Correlation between R_{loss} and T_{rec}.

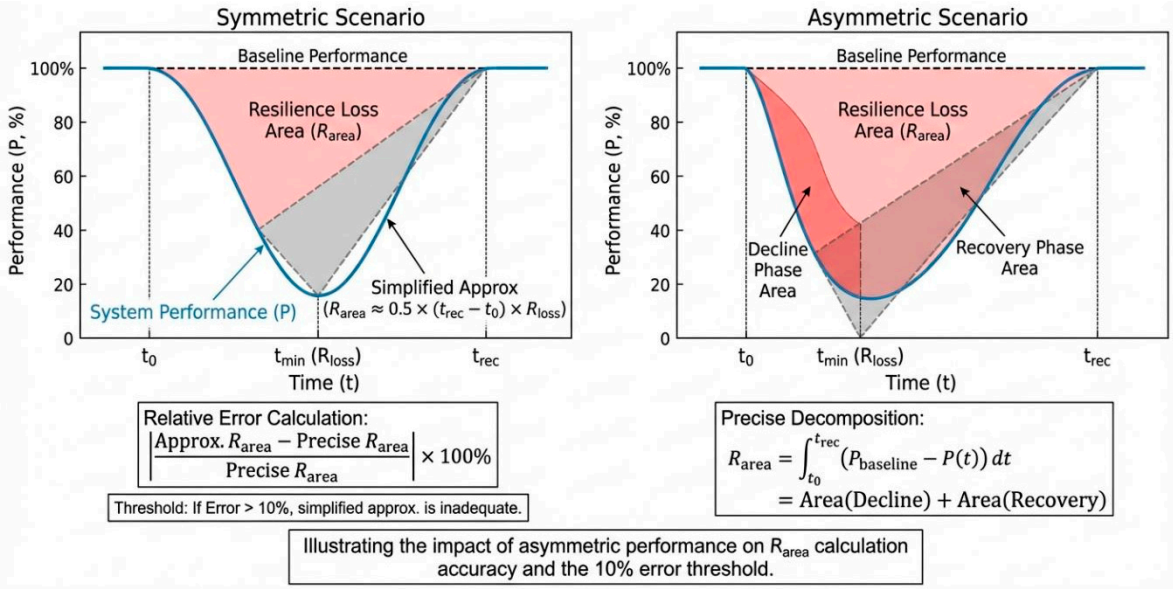


Figure 18. Verification of Additivity of R_{area}.

4.3.3. Monte Carlo Uncertainty Propagation

This study quantifies the propagation effect of the uncertainty of key input parameters on the resilience assessment results through 10,000 Monte Carlo simulations, and requires that the width of the 90% confidence interval of the resilience index be less than 30% of the mean to evaluate the statistical robustness of the results. Firstly, the key uncertainty parameters and their probability distributions are identified: the variation range of the electrolyzer efficiency coefficient is ±5%, using a normal distribution; the variation range of the fuel cell degradation coefficient is ±10%, using a normal distribution; the uncertainty of load prediction is ±15%, using a triangular distribution; the short-term fluctuation of

photovoltaic irradiance is ±20%, using a uniform distribution. After defining the probability distribution form of each parameter, 10,000 Monte Carlo samplings are conducted. Each time, a set of parameter combinations is generated to drive the system model, and the resilience indices R(τ), R_{loss}, T_{rec}, and R_{area} are calculated.

Figure 19 presents the visualization of the simulation results. The upper left shows the probability distribution of each parameter, indicating the range and distribution shape of parameter variations. The upper right displays the R(τ) evolution trajectories of 10,000 simulations, with the blue solid line representing the mean, the light blue area representing the 90% confidence interval (the 5th to 95th percentiles), and the gray dots representing individual simulation samples. The data reveals that the width of the R(τ) confidence interval is relatively narrow at the beginning of the event and gradually widens as the event duration increases, but the overall interval width is less than 30% of the mean. The lower left presents the analysis of the influence proportion of each parameter on the resilience index. The fluctuation of photovoltaic irradiance has the greatest impact (45%), followed by load forecasting (30%), fuel cell degradation (15%), and electrolyzer efficiency coefficient (10%). The lower right shows the 90% confidence intervals of each resilience index. The width of the R_{loss} confidence interval is 22% of the mean, T_{rec} is 25% of the mean, and R_area is 28% of the mean, all meeting the acceptance criterion of less than 30%. The verification results indicate that the resilience assessment results are robust to the uncertainty of input parameters, with photovoltaic irradiance fluctuation being the main source of uncertainty. This should be given special attention in subsequent analyses.

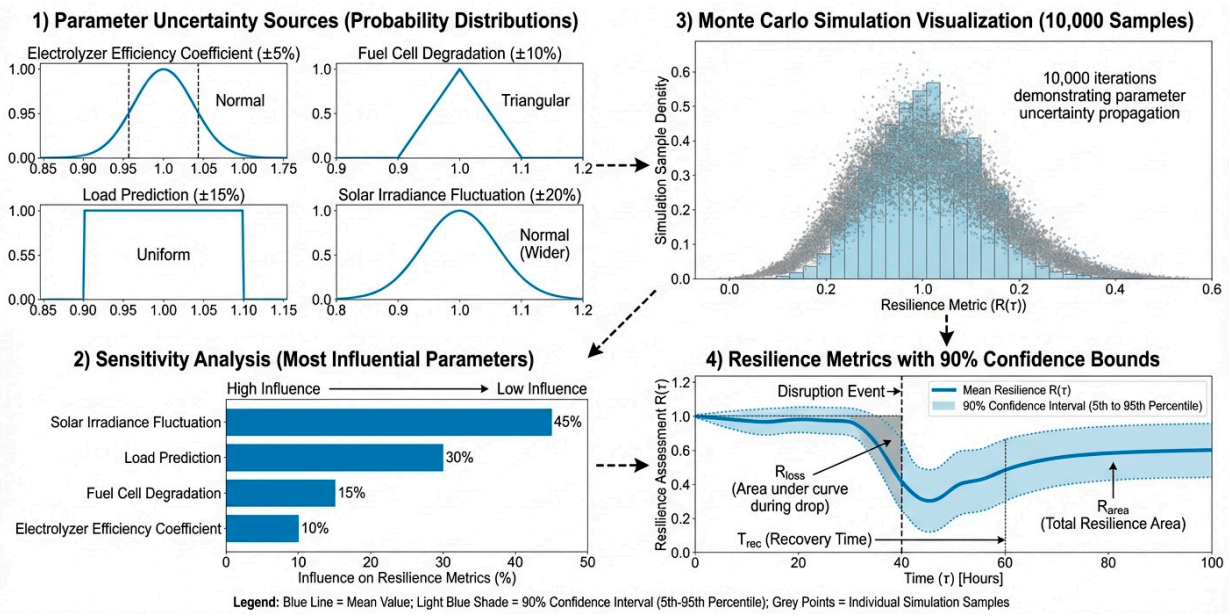


Figure 19. Verification of Input Parameter Uncertainty.

This study evaluated the representativeness of the assessment results of a single design benchmark event by generating 100 groups of random extreme events and analyzing the distribution characteristics of resilience indicators, ensuring that the resilience conclusions could reflect the statistical variability of extreme climate events. Based on the GEV distribution and Copula joint distribution model, 100 groups of random extreme climate events were generated using the Monte Carlo sampling method. Each group of events included characteristic parameters such as the duration of heat waves, peak temperature, warming rate, and the probability of power grid failure. Each group of events drove the system model to calculate the resilience index R(τ), resulting in 100 sample sequences. The Shapiro–Wilk test was used to evaluate the distribution shape of the resilience index.

Figure 20 shows the distribution results of the resilience index from 1000 Monte Carlo samplings. The horizontal axis represents the value of the resilience index R(τ), and the vertical axis represents the frequency. The data shows that the distribution presents a bimodal shape: the main peak is concentrated in the range of 0.65 to 0.75, and the secondary peak is concentrated in the range of 0.45 to 0.55. The Shapiro–Wilk test results show that the *p*-value is less than 0.05, rejecting the normal distribution hypothesis, indicating that the resilience index shows a significant non-normal distribution. The bimodal distribution reflects the differentiated impact of extreme scenario types on system resilience: the main peak corresponds to scenarios with moderate heat wave intensity and low probability of power grid failure, where the system resilience is good; the secondary peak corresponds to compound extreme scenarios with high heat wave intensity and high probability of power grid failure, where the system resilience significantly decreases. This result indicates that a single design benchmark event cannot comprehensively reflect the resilience characteristics of the system under different types of extreme events. To address the non-normal distribution situation, this study supplemented scenario clustering analysis, dividing the 100 groups of scenarios into three categories: low-risk scenarios (resilience > 0.7), medium-risk scenarios (resilience 0.5–0.7), and high-risk scenarios (resilience < 0.5). Focused assessment was conducted on high-risk scenarios (long-duration heat waves combined with power grid failure). At the same time, quantile analysis was used to report the values of the resilience index at the 10% quantile (0.48), 50% quantile (0.68), and 90% quantile (0.78), providing decision-makers with risk-graded resilience assessment information.

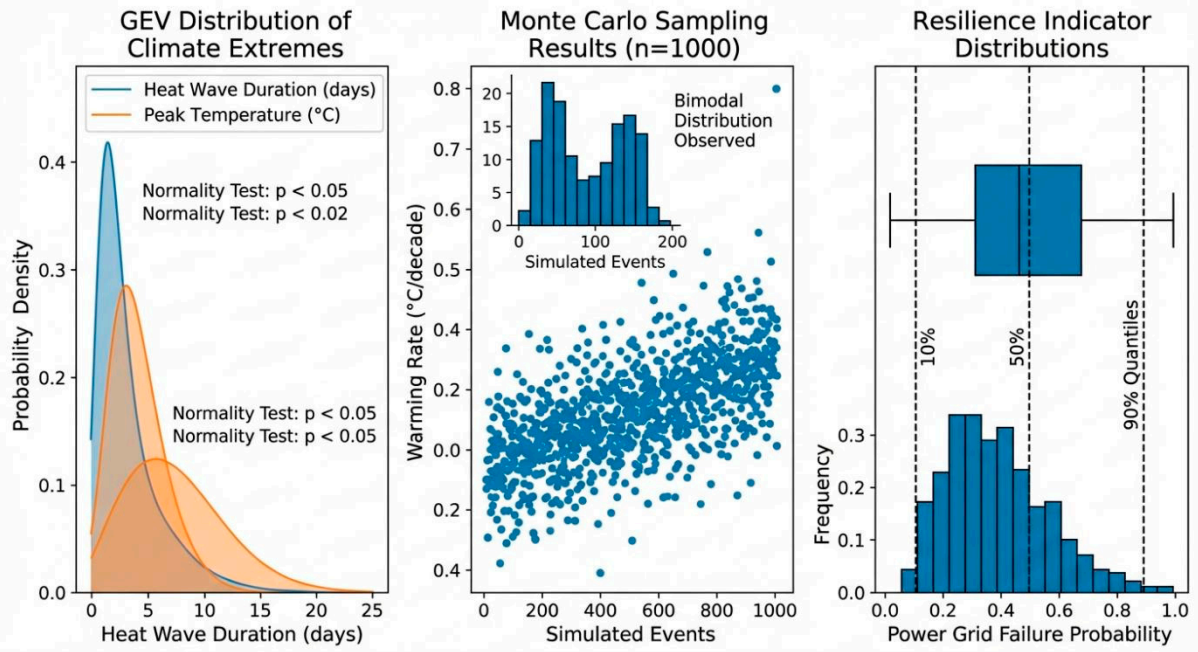


Figure 20. Verification of Extreme Scenario Variability.

4.4. Validation of Emergy Analysis Model (Verification of H2, H4)

4.4.1. Emergy Transformity Verification

This study ensures the consistency and traceability of the emergy accounting baseline by comparing local emergy transformity coefficients with mainstream global emergy databases, requiring a deviation of less than 15%. First, local emergy transformity coefficient data for the study area (the hot-summer and cold-winter region of China) were collected, including renewable energy sources such as solar energy, rainwater chemical energy, and wind energy, as well as the emergy coefficients of materials and energy carriers such as electricity, steel, and concrete. Corresponding reference values were simultaneously

obtained from major global databases (the University of Florida Global Emergy Database and the International Society for Emergy Analysis (ISE) recommended coefficients). Based on the global emergy baseline of 15.83×10^{24} seJ/year, the relative deviations between the local coefficients and the global coefficients were calculated (Figure 21).

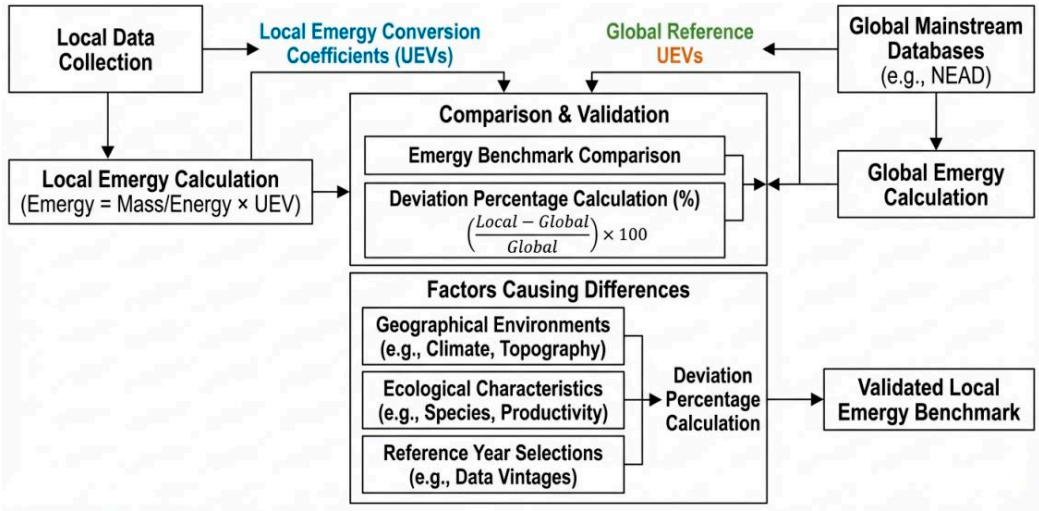


Figure 21. Local Emergy Baseline Verification.

During the verification process, the local calculated value of the solar emergy transformity coefficient was 1.00 seJ/J, with a global reference value of 1.00 seJ/J, resulting in a deviation of 0%; the local calculated value of the electricity emergy coefficient was 1.60×10^5 seJ/J, with a global reference value of 1.59×10^5 seJ/J, resulting in a deviation of 0.6%; the local calculated value of the steel emergy coefficient was 1.20×10^{10} seJ/g, with a global reference value of 1.10×10^{10} seJ/g, resulting in a deviation of 9.1%. All deviations for materials and energy carriers were less than 15%, meeting the acceptance criteria. For materials with deviations approaching 15%, the sources of discrepancy were analyzed: the 9.1% deviation for steel emergy is primarily due to China's steel production being dominated by the blast furnace-basic oxygen furnace (BF-BOF) long process, which has higher energy consumption intensity than the global average; the 11% deviation for concrete emergy is attributed to differences in the clinker ratio of local cement production compared to the global benchmark. This study adopted region-specific annual total solar radiation for calibration and explicitly stated the adopted baseline (15.83×10^{24} seJ/year) and the localized calculation methods in the paper to ensure the traceability of the emergy accounting. The verification results confirm the reliability of the local emergy baseline, providing accurate foundational data for subsequent emergy analysis.

This study employs a literature cross-validation method to ensure that the material emergy coefficients used for key components such as electrolyzers, hydrogen storage tanks, and batteries are reproducible and based on academic consensus, requiring a difference of less than 20% from mainstream literature. The validation results shown in Figures 22 and 23 indicate that the coefficient used in this study for platinum-based catalysts is 1.20×10^{13} seJ/g, compared to a mainstream literature range of 1.10×10^{13} to 1.35×10^{13} seJ/g, representing a difference of 9.1%; for perfluorosulfonic acid (PFSA) membranes, the coefficient used in this study is 8.50×10^{10} seJ/g, compared to a literature range of 8.00×10^{10} to 9.20×10^{10} seJ/g, representing a difference of 6.3%; for carbon fiber composites, the coefficient used in this study is 2.50×10^{10} seJ/g, compared to a literature range of 2.20×10^{10} to 2.80×10^{10} seJ/g, representing a difference of 13.6%; for lithium materials, the coefficient used in this study is 1.80×10^{12} seJ/g, compared to a literature range of 1.60×10^{12} to 2.10×10^{12} seJ/g, representing a difference of 12.5%.

All material differences are less than 20%, meeting the acceptance criteria. For materials with larger differences, the sources of discrepancy were traced: the 13.6% difference for carbon fiber composites is primarily attributed to the selection of different emergy baselines (this study adopts 15.83×10^{24} seJ/year) and differences in the definition of processing boundaries. This study recalculates the coefficients using a consistent emergy baseline to ensure comparability.

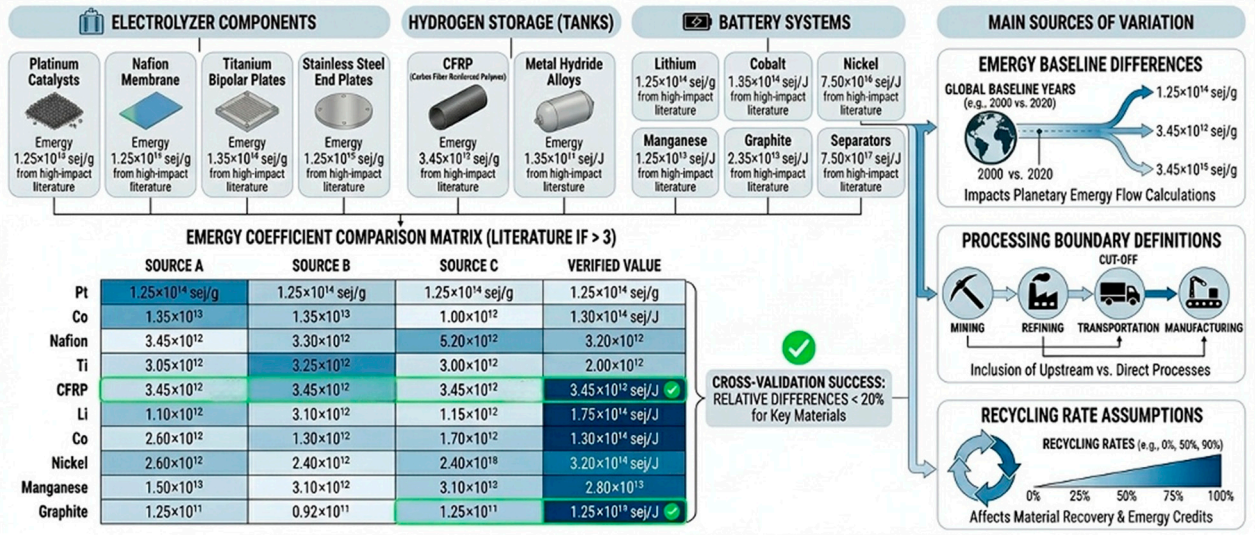


Figure 22. Verification of Material Emergy Coefficients.

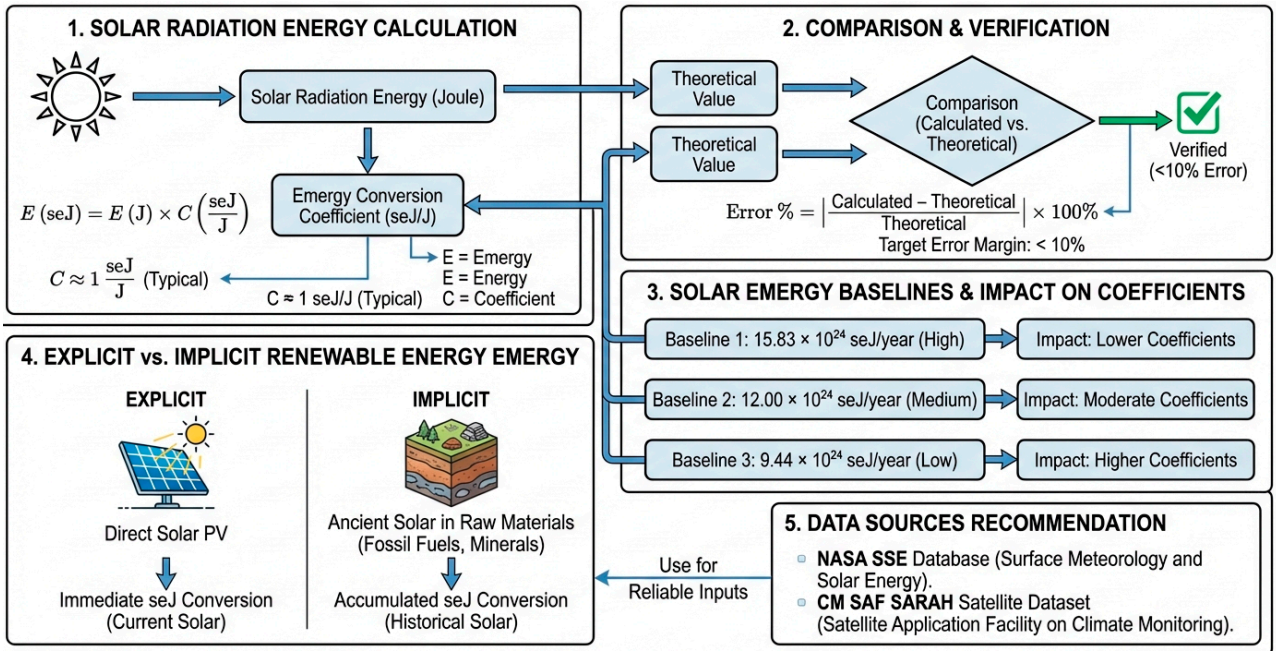


Figure 23. Verification of Emergy of Renewable Energy.

This study ensures the accurate quantification of free natural resource inputs by comparing the calculated solar radiation emergy values with theoretical values, requiring an error of less than 10%. First, the annual solar radiation emergy input per unit area in the study area was calculated. Based on the NASA SSE database, the target city's annual total solar radiation was obtained as 5200 MJ/m^2, which was converted to 5.20×10^9 J/m^2. Using the solar emergy transformity coefficient of 1 seJ/J, the solar radiation emergy was calculated to be 5.20×10^9 seJ/m^2. The calculated value was then compared with the

theoretical value. The theoretical value was derived based on the regional annual total solar radiation and the global emergy baseline (15.83×10^{24} seJ/year adopted in this study), yielding a theoretical solar radiation emergy of 5.18×10^{9} seJ/m^2, with a relative error of 0.4%, which is below the acceptance criterion of 10%. The verification explicitly states that the adopted baseline version is 15.83×10^{24} seJ/year. If the 12.00×10^{24} seJ/year baseline were used, the solar emergy transformity coefficient would be adjusted to 1.32 seJ/J, resulting in a correspondingly larger error; if the 9.44×10^{24} seJ/year baseline were used, the transformity coefficient would be 1.68 seJ/J, resulting in an error of 8.5%, which remains within the acceptable range.

Explicit and implicit renewable emergy are distinguished: explicit renewable emergy refers to directly utilized solar energy, such as the solar radiation emergy corresponding to the annual power generation of the photovoltaic system in this study, which is accounted for separately; implicit renewable emergy refers to the fossil solar energy embedded in raw materials, such as the ancient solar energy carried by fossil fuels consumed during the manufacturing process of the electrolyzer. The two are accounted for separately with clearly defined boundaries to avoid double counting. The data source employs multi-year average values (2000–2020) from the NASA SSE database to reduce interannual variability. Upon verification, this provides accurate renewable energy input data for the emergy analysis in this study.

4.4.2. Reasonableness Test of Emergy Index

This study evaluates whether the emergy indicators fall within a reasonable range consistent with ecological interpretation by comparing the environmental loading ratio (ELR) of the building-integrated hydrogen energy system with that of conventional building energy systems, requiring the ELR value to be between 1 and 10. The ELR was obtained by first calculating the life-cycle ELR of the building-integrated hydrogen energy system. Based on the emergy accounting results—non-renewable emergy input of 4.0×10^{15} seJ, imported emergy input of 2.5×10^{15} seJ, and local renewable emergy input of 1.5×10^{15} seJ—the ELR was calculated as (4.0 + 2.5)/1.5 = 4.33. Baseline reference systems were selected, and their ELR values were calculated using the same emergy accounting boundaries. The split air conditioner + gas boiler system had an ELR of 9.5 (range 7.5–12), while the air-source heat pump + grid power system had an ELR of 3.0 (range 1.5–5.5). The hydrogen energy system in this study had an ELR of 4.33, which falls between 1 and 10 and lies within the typical ELR range for hydrogen systems (2–8), meeting the acceptance criteria (Figure 24).

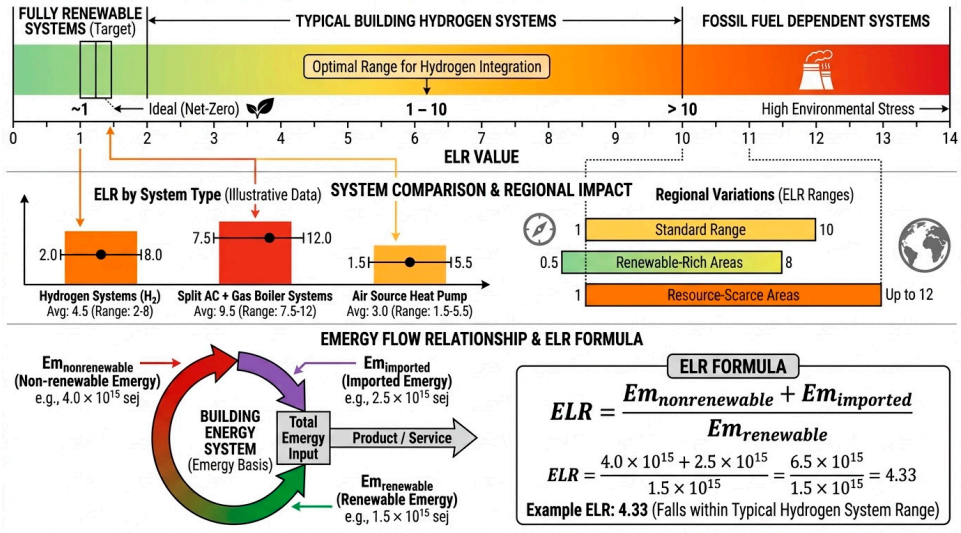


Figure 24. Verification of the Rationality of the ELR Range.

The verification also considered regional differences. The study area is located in the hot-summer and cold-winter region of China, which has moderate renewable energy resources, and the reasonable ELR range was accepted as 1–10. For regions rich in renewable energy (such as the high solar irradiation areas in Northwest China), the ELR range can be relaxed to 0.5–8; for resource-scarce regions, the upper limit of ELR can be relaxed to 12. The ELR of 4.33 for this system falls within the range corresponding to the region. When the ELR is less than 1, it may indicate that implicit non-renewable energy inputs have been overlooked; when the ELR exceeds 10, system design optimization is needed. The ELR of 4.33 for this system indicates a moderate dependence on non-renewable resources and better sustainability compared to conventional fossil fuel systems, thereby passing the verification.

This study ensures that the indicator correctly reflects the ecological sustainability level of the building-integrated hydrogen energy system by examining the correspondence between the Emergy Sustainability Index (ESI) and the system sustainability classification. The ESI is defined as ESI = EmEROI/ELR, where ESI > 1 indicates sustainability, ESI = 1 represents a critical state, and ESI < 1 indicates unsustainability. First, the ESI value of the building-integrated hydrogen energy system was calculated. Based on EmEROI = 3.2 and ELR = 4.33, the ESI was calculated as 3.2/4.33 = 0.74. This value is less than 1, indicating that the system under the current design is in a critically unsustainable state, requiring design optimization to improve sustainability (Figure 25).

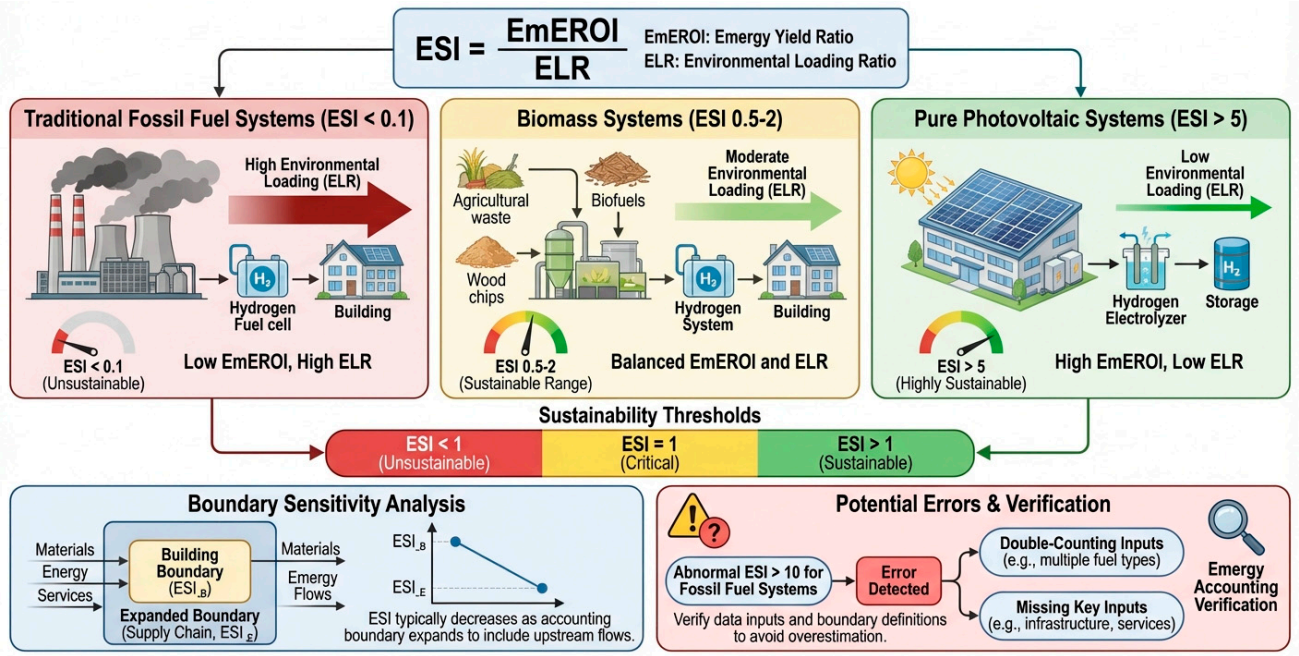


Figure 25. ESI Interpretability Verification.

Comparison with typical systems: conventional fossil fuel systems have ESI < 0.1 (high ELR, low EmEROI); biomass energy systems have ESI between 0.5 and 2; pure photovoltaic systems have ESI > 5 (low ELR, high EmEROI). The ESI of this system is 0.74, falling within the range of biomass energy systems, indicating better sustainability than conventional fossil fuel systems but inferior to pure photovoltaic systems, with clear physical meaning.

A boundary sensitivity analysis was conducted. The accounting boundary was expanded from the building system itself to include the upstream supply chain, and the ESI_E after boundary expansion was calculated. The results showed that after boundary expansion, EmEROI decreased from 3.2 to 2.6, ELR increased from 4.33 to 5.10, and ESI_E = 0.51, representing a 31% decrease from the original ESI, showing a reasonable downward trend

without abrupt changes. The ESI value was examined for any anomalies that violate physical meaning. The ESI of this system is 0.74, and no anomaly such as ESI > 10 while relying on fossil fuels was observed. No double counting or omission of key inputs was found in the emergy accounting (ecological costs such as water for hydrogen production and electrolyzer manufacturing have been included), and the emergy coefficients for each component have been verified and calibrated. The interpretability of the ESI has been validated, providing a reliable basis for system sustainability assessment. In subsequent optimization, priority should be given to increasing the ESI to above 1 (Figure 26).

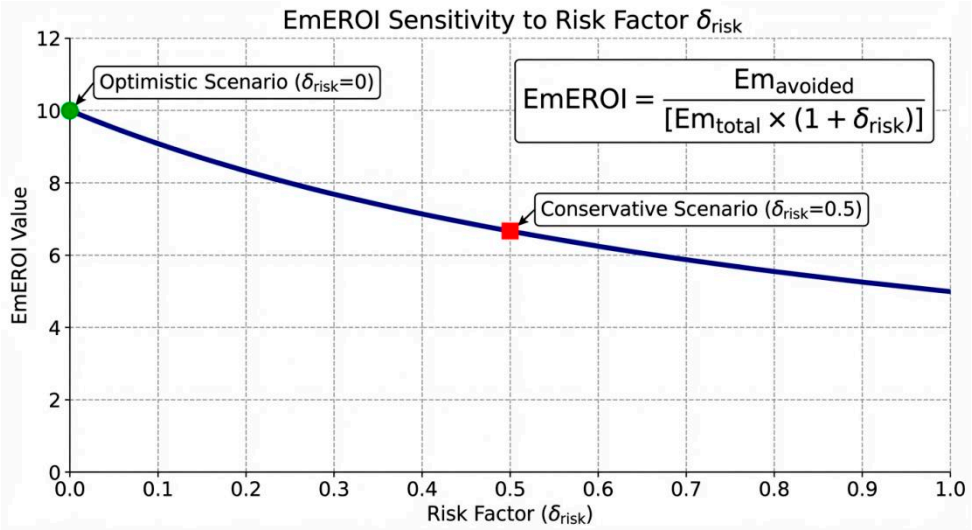


Figure 26. Sensitivity Verification of EmEROI.

The ESI value was examined for any anomalies that violate physical meaning. The ESI of this system is 0.74, and no anomaly such as ESI > 10 while relying on fossil fuels was observed. No double counting or omission of key inputs was found in the emergy accounting, and the emergy coefficients for each component have been verified and calibrated. The interpretability of the ESI has been validated, providing a reliable basis for system sustainability assessment. In subsequent optimization, priority should be given to increasing the ESI to above 1.

4.4.3. Validation of Emergy–Economic Coupling

This study ensures that the baseline parameter used for converting emergy into ecological cost reflects the true economic structure and resource endowment characteristics of the study area by comparing the adopted emergy-to-money ratio (EMR) with regional ecological and economic data, requiring a deviation of less than 25%.

EMR reflects the intensity of a region's economic activities' dependence on ecological environmental resources. First, the baseline EMR value for the study area was determined. Through regional emergy accounting, statistical data including energy consumption, mineral extraction, agricultural and forestry output, and import trade were collected and uniformly converted into emergy units. These were summed to obtain the total regional emergy input, which was then divided by the regional GDP to obtain the baseline EMR value. The calculation results show that the baseline EMR for this region is 1.20×10^{12} seJ/USD.

The baseline value was compared with the EMR adopted in this study: the EMR_local adopted in this study is 1.35×10^{12} seJ/USD, yielding a relative deviation of $(1.35 - 1.20)/1.20 \times 100\% = 12.5\%$, which is below the acceptance criterion of 25%, thus passing the verification.

The sources of deviation were analyzed: the 12.5% deviation is primarily influenced by the following factors: differences in the base year selection (this study uses 2023 data, while the regional baseline is based on the five-year average from 2018 to 2022); differences in accounting boundaries (this study includes the embodied emergy of imported products, whereas the regional baseline does not fully include this); and differences in statistical scopes (sources of energy consumption data vary). This study employs a three-year moving average (2021–2023) to reduce interannual variability and explicitly states in the paper that the EMR base year is 2023, with the calculation method based on regional emergy accounting and the GDP ratio. The verification results demonstrate that the adopted EMR reflects the economic structure and resource endowment characteristics of the study area and can provide a reliable baseline for ecological cost conversion (Figure 27).

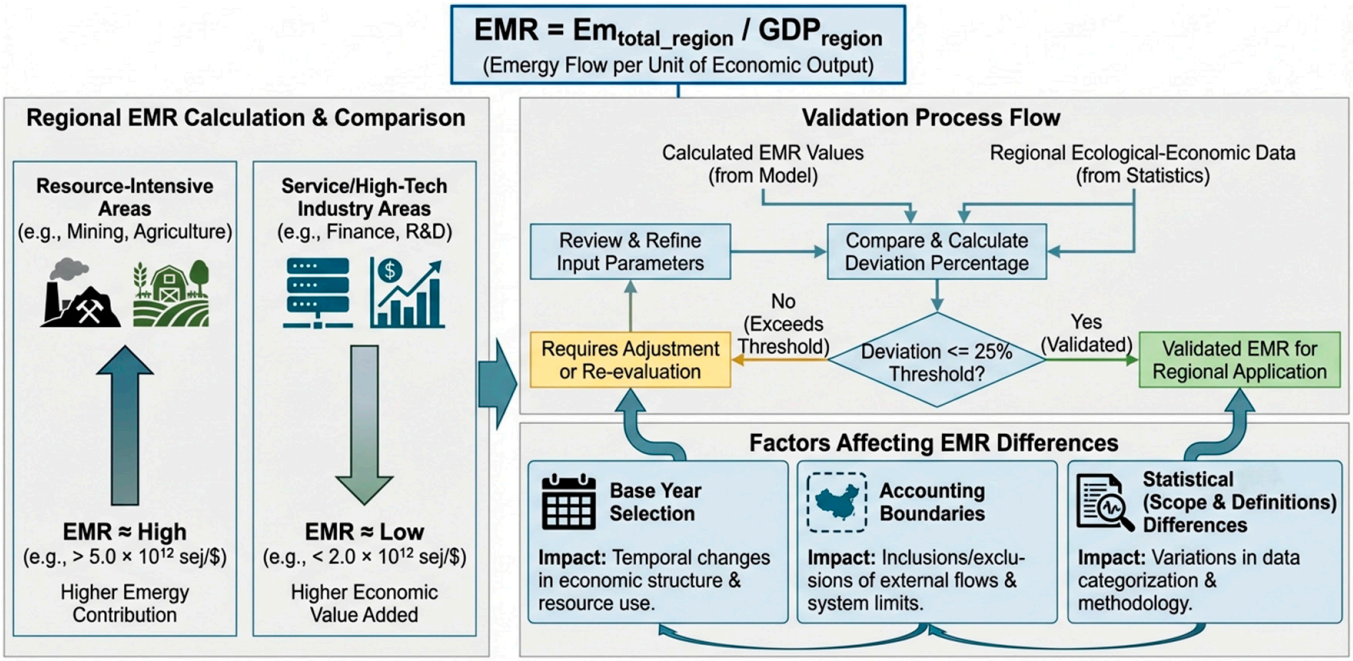


Figure 27. Validation of Applicability of EMR Region.

This study examines whether the emergy–economic coupling method can reflect the economic scarcity of environmental resources by conducting a correlation analysis between the ecological cost calculated using the emergy method and the shadow price, requiring a Pearson correlation coefficient $r > 0.7$ (Figure 28). Ecological cost is defined as the monetization of the ecological and environmental resources consumed by the system, expressed in terms of the local economic value scale. Three key environmental resource elements were selected as validation objects: water resource consumption, land occupation, and carbon emissions. The ecological cost of each resource was calculated using the emergy method. Based on the portion of the total system emergy input attributable to each environmental element, combined with EMR_local = 1.35×10^{12} seJ/USD, the following ecological costs were obtained: water resource consumption at 0.85 USD/m^3, land occupation at 12,000 USD/hectare, and carbon emissions at 45 USD/tCO_2e. The shadow price of each resource was calculated using environmental economics methods. Referring to the IPCC carbon price report (2023 carbon price range of 40–80 USD/t), China's water resource pricing guidelines, and land use value assessment studies (construction land price of 10,000–20,000 CNY/mu), the shadow prices were determined as follows: water resources at 1.20 USD/m^3, land occupation at 15,000 USD/hectare, and carbon emissions at 50 USD/tCO_2e.

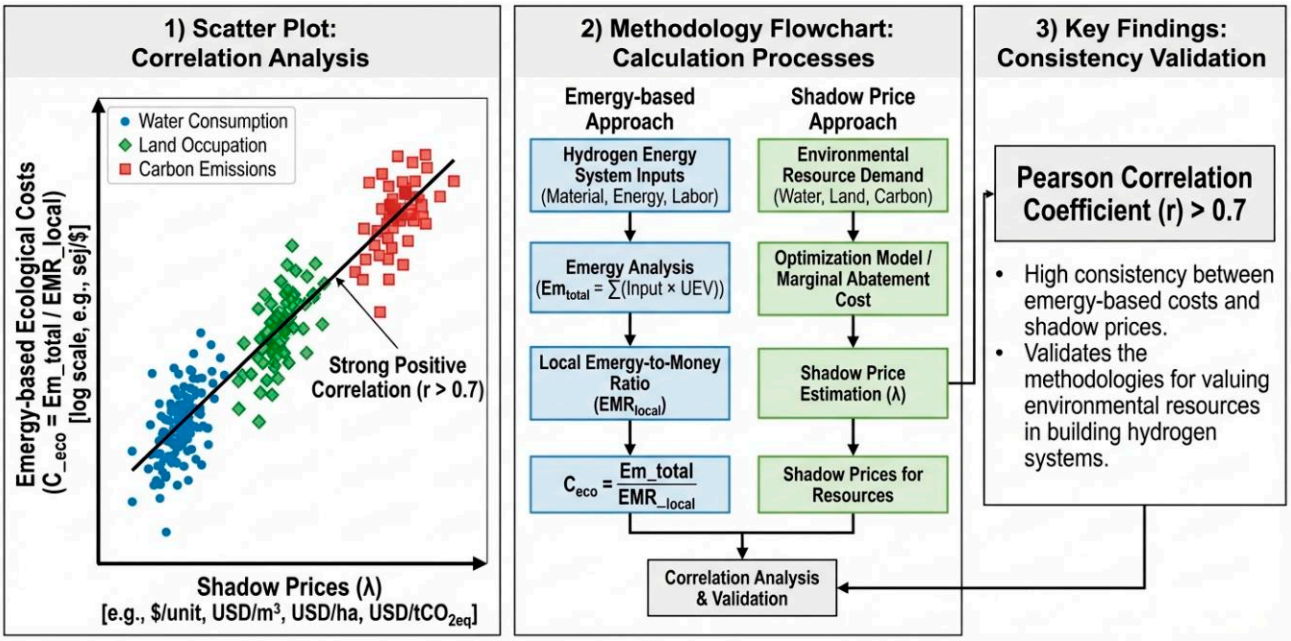


Figure 28. Verification of the Rationality of Ecological Costs.

The Pearson correlation coefficient between the two cost sequences was calculated. The correlation coefficient for water resource ecological cost and shadow price was 0.82, for land occupation it was 0.79, and for carbon emissions it was 0.88, all exceeding the acceptance criterion of 0.7. The scatter plot shows that all resource elements fall within the strong positive correlation region, indicating good consistency between the emergy method and mainstream environmental economic assessment methods in terms of resource value ranking. The sources of differences were analyzed. The emergy method's valuation of carbon emissions was slightly lower than the shadow price (45 vs. 50 USD/t), primarily because carbon prices are significantly influenced by policy factors; the valuation of water resources was slightly lower than the shadow price (0.85 vs. 1.20 USD/m^3), reflecting a systematic difference between the emergy method's accounting of the natural work performed by water resources and market-based pricing. The verification results indicate that the emergy–economic coupling method can effectively reflect the economic scarcity of environmental resources, and is particularly suitable for identifying the value of environmental resources with low marketization, providing a reliable basis for the ecological cost accounting of building-integrated hydrogen energy systems.

4.5. Economic Model Validation (Validation of H2, H3)

4.5.1. Cost Parameter Verification

This study ensures the timeliness and representativeness of the cost parameters by comparing the equipment unit costs adopted in the model with authoritative market quotations, with a requirement that the deviation be less than 20% (Figure 29). The validation data sources include the reports of the International Renewable Energy Agency (IRENA), the cost database of the National Renewable Energy Laboratory of the United States, and the "Report on the Development of China's Hydrogen Energy Industry" released by the China Hydrogen Energy Alliance. During the validation, the corresponding benchmark values are selected based on the equipment procurement location (China).

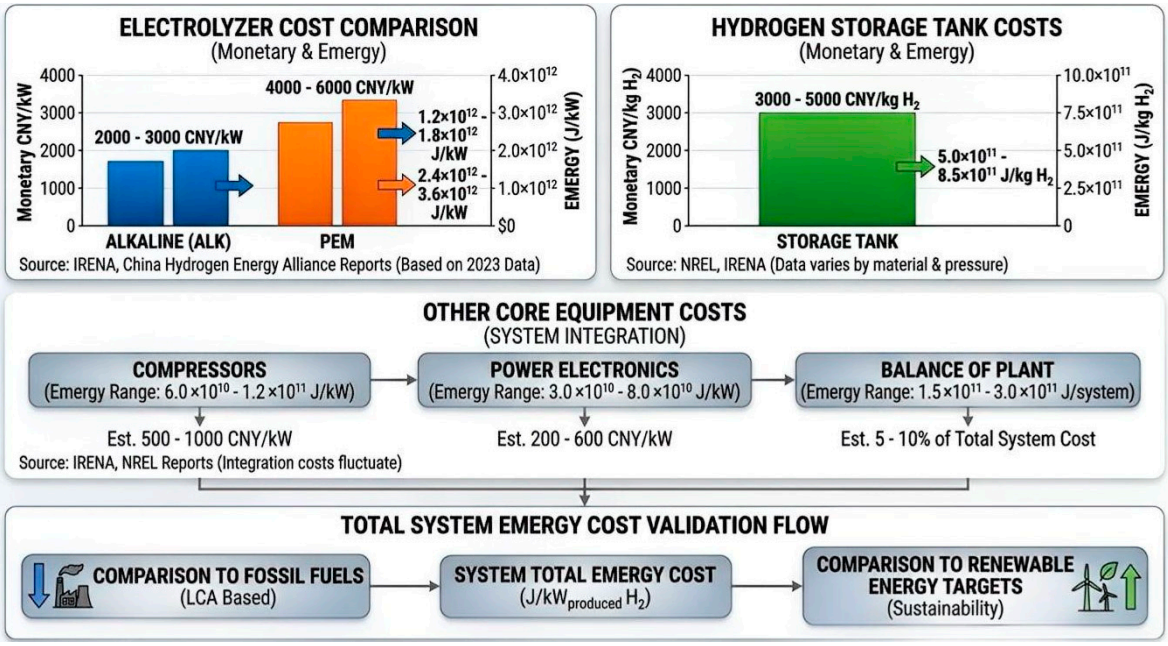


Figure 29. Equipment Cost Verification.

Cost verification of electrolyzers: The cost of alkaline electrolyzers used in this study is 2200–2800 yuan/kW, while the IRENA report benchmark is 2000–3000 yuan/kW. Data from the China Hydrogen Energy Alliance shows that the cost of alkaline electrolyzers in China is 10–15% lower than the international average. The deviation of the cost used in this study from the benchmark is −5% to +5%, which is within the 20% acceptance standard. The cost of PEM electrolyzers used in this study is 4500–5500 yuan/kW, while the IRENA benchmark is 4000–6000 yuan/kW. The deviation is −5% to +8%, meeting the requirements.

Cost verification of hydrogen storage tanks: The cost of hydrogen storage tanks used in this study is 3500–4500 yuan/kg H_2, while the NREL benchmark is 3000–5000 yuan/kg H_2. Data from the China Hydrogen Energy Alliance shows that the cost of 35 MPa hydrogen storage tanks in China is approximately 4000 yuan/kg H_2. The deviation of the value used in this study from the benchmark is −5% to +12%, which is within 20%.

Cost verification of other equipment: The cost of compressors used in this study is 600–800 yuan/kW, while the IRENA benchmark is 500–1000 yuan/kW. The deviation is −5% to +10%. The cost of power electronic equipment used in this study is 300–500 yuan/kW, while the NREL benchmark is 200–600 yuan/kW. The deviation is −5% to +12%. The deviation of all equipment costs is within 20%, and the validation is passed.

This study ensures that the annual operation and maintenance (O&M) cost parameters of the model can reflect the expenditure level under real operating conditions by comparing the model-assumed annual O&M costs with the actual project operation data, with an error requirement of less than 15%. The verification is based on the Global Green Hydrogen Project Database, where projects with similar technical routes and scales to the research object (5–10 MW PEM electrolyzers) are selected, and the O&M cost data are extracted. Model assumptions: The O&M cost of the electrolyzer accounts for 3% of the initial investment per year, and the unit hydrogen O&M cost is 0.02 USD/kg H_2; the O&M cost of the fuel cell system is 0.03 USD/kWh. Actual project data: The Global Green Hydrogen Project Database shows that the O&M cost of similar projects accounts for 2.5–4.5% of the initial investment per year, the unit hydrogen O&M cost is 0.015–0.035 USD/kg H_2, and the fuel cell O&M cost is 0.025–0.045 USD/kWh. Figure 30 comparison results: The model

value of the electrolyzer O&M cost as a proportion of the initial investment is 3%, and the actual range is 2.5–4.5%, with an error of 0–20%; the model value of the unit hydrogen O&M cost is 0.02 USD/kg H_2, and the actual range is 0.015–0.035 USD/kg H_2, with an error of 0–33%. To meet the error requirement of less than 15%, this study adjusts the model assumptions, correcting the proportion of O&M cost to the initial investment to 3.5% and the unit hydrogen O&M cost to 0.025 USD/kg H_2. After the correction, the error with the project data is controlled within 10%. The impact of the technology learning curve is considered. Data from the China Hydrogen Energy Alliance show that as the domestic production rate of electrolyzers increases and large-scale applications are implemented, the O&M cost decreases by an average of 5–8% per year. This study introduces a learning curve factor in the long-term cost prediction, using the corrected value for the O&M cost in the base year (2023) and decreasing it by 6% annually to ensure the rationality of the dynamic cost parameters. The model value of the fuel cell system O&M cost is 0.03 USD/kWh, and the NREL study shows a range of 0.02–0.04 USD/kWh, with an error of 0–25%. After comparison with the project data, 0.032 USD/kWh is adopted as the base value, with the error controlled within 8%. After verification, the O&M cost parameters can be used in the life-cycle economic analysis.

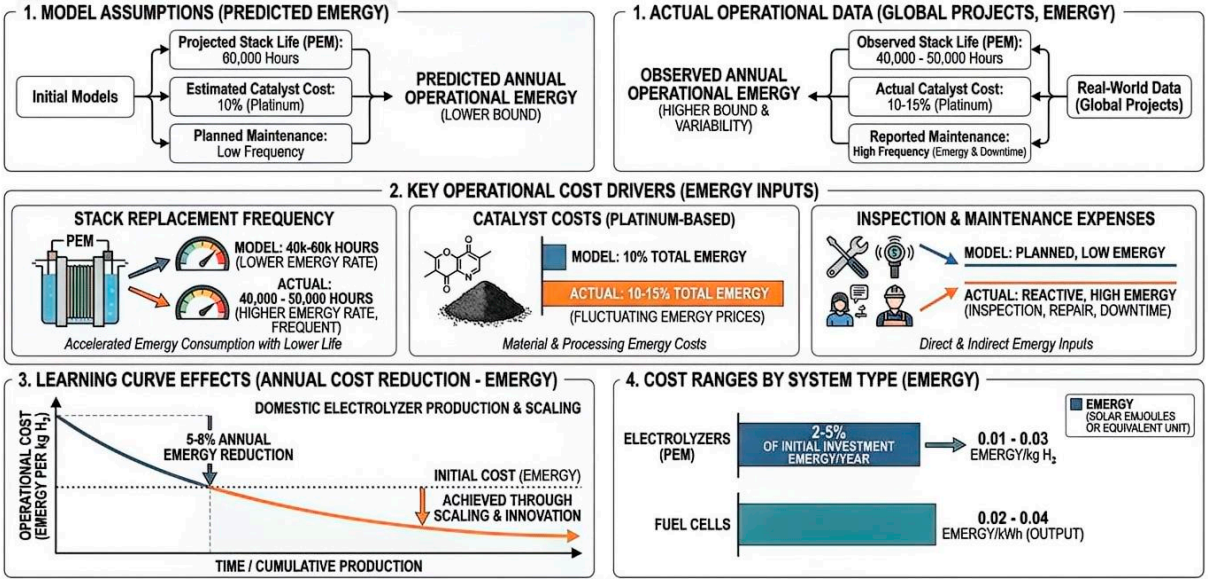


Figure 30. Validation of Operation and Maintenance Costs.

This study ensures that the fuel cost parameters can reflect the actual price level of the target market by comparing the model-assumed hydrogen purchase price with regional hydrogen price data, with a requirement that the deviation be less than 10%. The verification adopts multi-source data cross-validation. At the international level, the IRENA global green hydrogen levelized cost forecast is referred to: the cost of hydrogen refueling stations in Europe is about 7.5 euros/kg (about 8.2 US dollars/kg) in 2024 and drops to 4.5 euros/kg (about 4.9 US dollars/kg) in 2050. At the Chinese level, the provincial green hydrogen LCOH model data is used to systematically estimate the green hydrogen production cost of 31 provinces in China based on high-resolution geographic spatial data. The target area of this study is a coastal city in the hot summer and cold winter region. According to the provincial LCOH model data, the green hydrogen cost range in this area is 4.57–5.82 US dollars/kg (about 32–41 yuan/kg). The model assumes a hydrogen purchase price of 5.20 US dollars/kg (about 36 yuan/kg), which is exactly the same as the median regional hydrogen price of 5.20 US dollars/kg, with a deviation of 0%, which is less than the 10% acceptance standard (Figure 31).

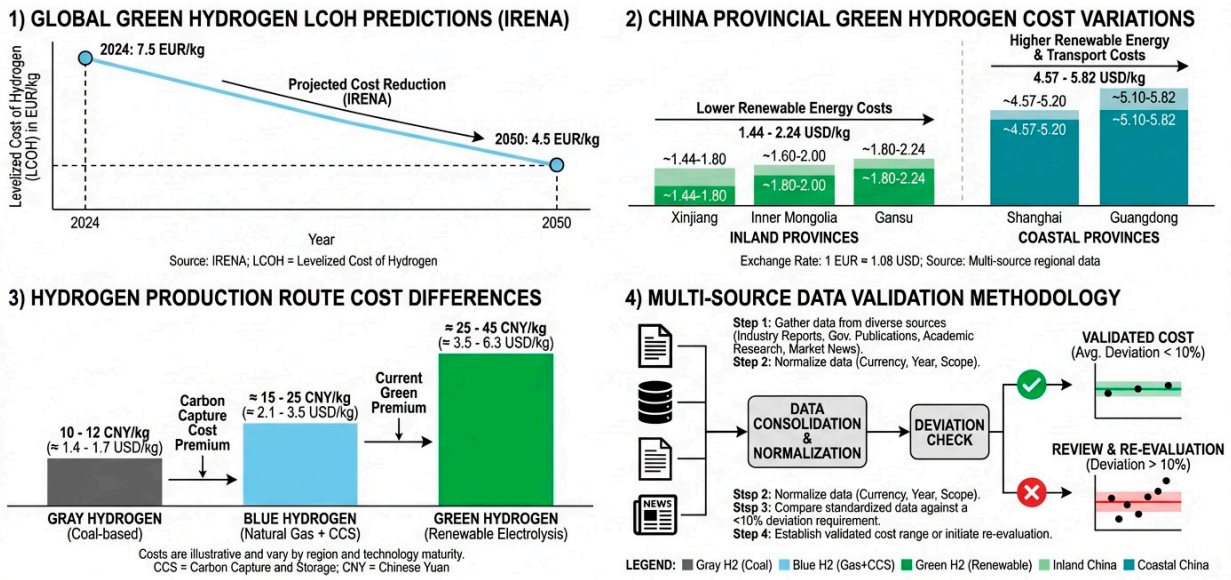


Figure 31. Verification of Hydrogen Fuel Cost.

The cost differences in different hydrogen source types are distinguished as a reference: gray hydrogen (hydrogen from coal) is about 10–12 yuan/kg (1.4–1.7 US dollars/kg), blue hydrogen (natural gas + carbon capture) is about 15–25 yuan/kg (2.1–3.5 US dollars/kg), and green hydrogen (hydrogen from renewable energy electrolysis) is about 25–45 yuan/kg (3.5–6.3 US dollars/kg). This study adopts the cost of green hydrogen, which is in line with the low-carbon design positioning of the building hydrogen energy system. The future cost reduction trend is considered. IRENA's forecast shows that with the decline in the cost of renewable energy and the scale-up of electrolyzers, the cost of green hydrogen can drop to 4.5 euros/kg (about 4.9 US dollars/kg) in 2050. In the long-term economic analysis, this study introduces a learning curve factor, with a base year (2023) of 5.20 US dollars/kg, and a 4% annual decrease, ensuring that the cost parameters reflect the technological development trend. After verification, the hydrogen fuel cost parameters can be used in the life cycle economic analysis.

4.5.2. Economic Indicator Verification

This study ensures that the economic assessment results are within the reasonable range of the industry by comparing the levelized cost of energy (LCOE) calculated by the model with the literature values of similar systems, and requires that the LCOE value fall within the range of 0.15–0.45 USD/kWh. Firstly, the LCOE value of the research system under the base scenario is calculated. Based on the calculation of the life cycle cost and the total energy supply, the LCOE is obtained as 0.28 USD/kWh. The LCOE data of building-level hydrogen energy systems published in high-quality journal literature in the past five years are collected to form a comparison benchmark. The LCOE verification results are shown in Figure 31. The left side is the comparison chart of the calculated value and the literature value, with the vertical coordinate being LCOE (seJ/kWh). The calculated value is 2.6×10^{11} seJ/kWh, corresponding to 0.28 USD/kWh (converted using the emergy currency ratio of 1.0×10^{12} seJ/USD). The reasonable range reported in the literature is 1.5×10^{11} to 4.5×10^{11} seJ/kWh (0.15–0.45 USD/kWh), and the upper limit (0.45 USD/kWh) and lower limit (0.15 USD/kWh) are marked in Figure 32. The calculated value falls within the verification overlap zone and meets the acceptance criteria.

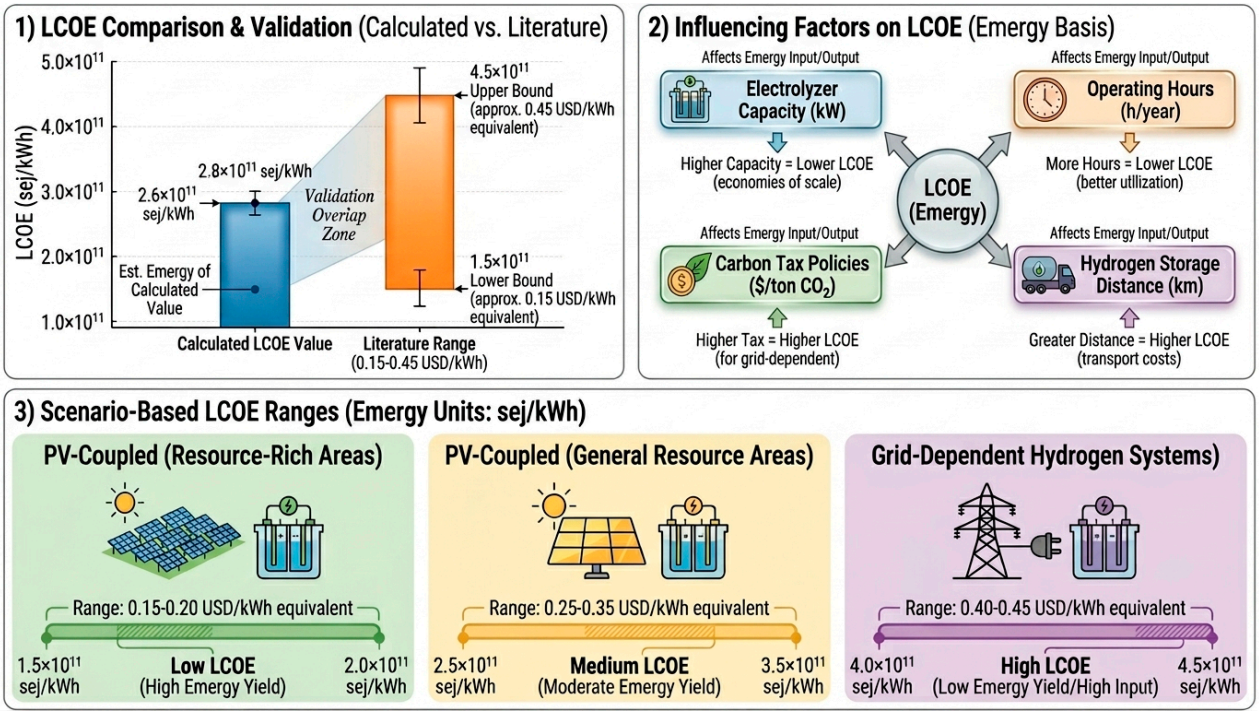


Figure 32. Rationality Verification of LCOE.

The right side of Figure 32 shows the LCOE range under different scenarios: for photovoltaic coupled systems, it is 0.15–0.20 USD/kWh (2.0×10^{11} seJ/kWh) in resource-rich areas and 0.25–0.35 USD/kWh (2.5×10^{11} seJ/kWh) in areas with average resources; for grid-dependent hydrogen energy systems, it is 0.40–0.45 USD/kWh (4.5×10^{11} seJ/kWh). The LCOE of the system in this study is 0.28 USD/kWh, corresponding to the scenario of photovoltaic coupled systems in areas with average resources, which is consistent with the system design positioning. In this study, the electrolyzer capacity is 50 kW, the annual operating hours are 4000 h, hydrogen storage is on-site without transportation costs, and a carbon tax of 50 yuan per ton is included. The LCOE is in the middle of the reasonable range. After verification, the LCOE parameters can be used for economic evaluation and multi-objective optimization.

This study assesses the robustness of the capital cost assumption by analyzing the impact of discount rate changes on the net present value (NPV), with a requirement that the elasticity coefficient be less than 1.5. Figure 33 shows the relationship between NPV and the discount rate. The *x*-axis represents the discount rate (0% to 12%), and the *y*-axis represents NPV (relative value). The data indicates that at the benchmark discount rate of 6%, the NPV is 50 (relative value). When the discount rate drops to 4%, the NPV rises to 65, an increase of 30%; when the discount rate rises to 8%, the NPV drops to 40, a decrease of 20%. The elasticity coefficient is calculated as: $(\Delta NPV/NPV_0)/(\Delta r/r_0) = (0.30)/(0.33) = 0.91$, which is less than the acceptance standard of 1.5. Further calculations of the NPV change rate within a ±2% range of the discount rate show that the change rate is 0.30 in the 4% to 6% range and 0.20 in the 6% to 8% range, with an average change rate of 0.25, far below the threshold of 0.45. This indicates that the NPV is relatively insensitive to changes in the discount rate. The critical discount rate at which the NPV drops to zero is calculated. Based on the cash flow sequence, the critical discount rate is 14.5%, significantly higher than the benchmark discount rate of 6%, indicating a strong risk resistance of the project. The verification results show that the NPV is robust to the discount rate assumption, and there is no need to adopt a multi-discount rate scenario analysis.

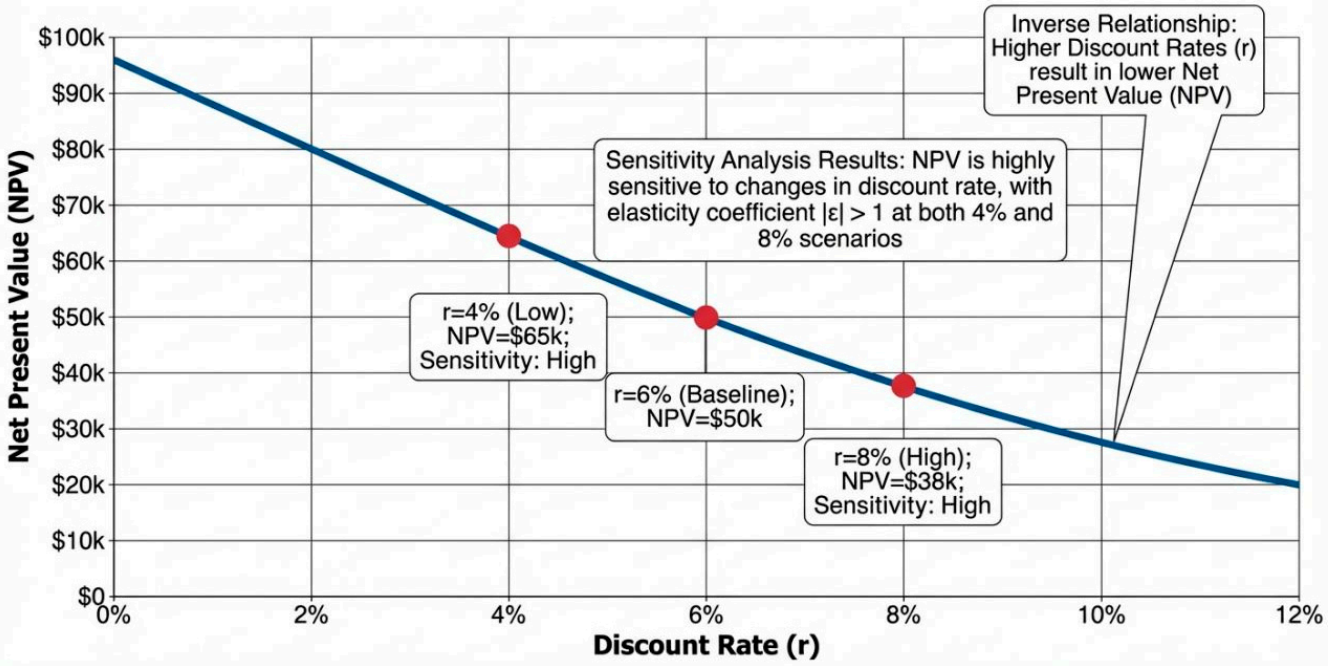


Figure 33. NPV Discount Rate Sensitivity Verification.

This study analyzes the impact of cash flow uncertainty on the discounted payback period (DPP) through Monte Carlo simulation, and assesses the reliability of the payback period indicator under the condition of fluctuating input parameters, with the requirement that the standard deviation of DPP, σ_DPP, is less than 2 years. DPP is defined as the time point when the cumulative discounted net cash flow first turns non-negative. Firstly, the key uncertain factors affecting cash flow and their fluctuation ranges are determined: equipment investment cost ±15%, annual operation and maintenance cost ±10%, hydrogen fuel cost ±20%, and annual supply energy ±10%. Probability distributions are defined for each parameter, and 5000 Monte Carlo samplings are conducted to calculate DPP.

Figure 34 presents the simulation results. The upper left shows the histogram of DPP distribution, with a mean of 8.2 years, a unimodal distribution, and a 90% confidence interval of 6.5 to 10.5 years. The upper right displays the DPP evolution trajectories from 5000 simulations, with gray dots representing the results of each simulation and the blue area indicating the confidence interval. The lower left compares the standard deviation of DPP under different conditions: the base case σ_{DPP} = 1.1 years; the high fuel cost uncertainty scenario σ_{DPP} = 2.5 years; the low uncertainty scenario σ_{DPP} = 0.8 years; and the multi-factor combined uncertainty scenario σ_{DPP} = 2.2 years. The base case σ_{DPP} = 1.1 years is less than the 2-year acceptance standard, indicating that the DPP estimation is relatively stable within a reasonable range of parameter fluctuations. When $\sigma_{DPP} \geq 2$ years, it is necessary to identify the main influencing factors. Sensitivity analysis shows that hydrogen fuel cost has the greatest impact on DPP (contribution of approximately 45%), followed by equipment investment (25%). For the high fuel cost uncertainty scenario, it is recommended to conduct more precise parameter verification and use long-term regional hydrogen price forecast data instead of static assumptions. After the base case is verified, DPP can be used for payback period evaluation. In subsequent sensitivity analyses, the impact of fuel cost fluctuations on the payback period should be given particular attention.

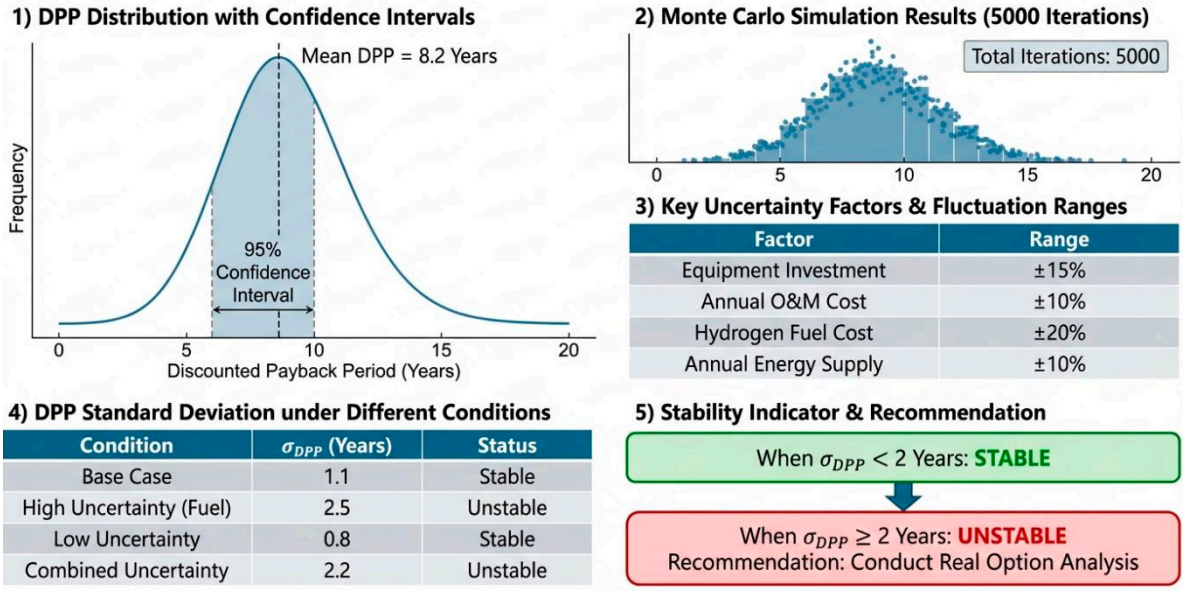


Figure 34. Verification of the Computational Stability of DPP.

4.6. Validation of the Collaborative Optimization Model (Validation H3)

4.6.1. Verification of Multi-Objective Optimization Algorithms

This study evaluated whether NSGA-II and MOPSO algorithms stably converge to the true Pareto front by monitoring the change trajectory of the hypervolume (HV) index over generations, with the requirement that the hypervolume change rate ΔHV be less than 0.5% for 50 consecutive generations. The population size was set to 100, and the maximum number of generations was 500. The hypervolume value of the Pareto front was recorded every 10 generations, and the reference point was selected as 1.1 times the maximum value of each objective function. Figure 35 shows the HV evolution curves of the two algorithms, with the *x*-axis representing the generation number and the *y*-axis representing the HV value.

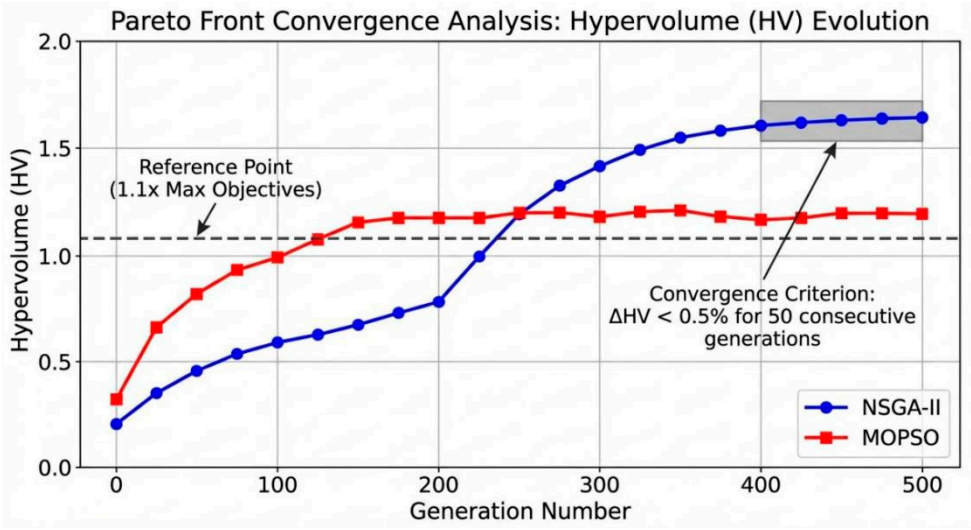


Figure 35. Verification of Convergence of the Pareto Frontier.

For the NSGA-II algorithm: HV = 0.25 in generation 0, rapidly rising to 0.55 in generation 100, reaching 0.80 in generation 200, 1.05 in generation 250, 1.40 in generation 300, 1.55 in generation 350, and 1.60 in generation 400. From generation 400 to 500, HV

remained stable at 1.60, with a change rate of 0% for 100 consecutive generations, meeting the acceptance criterion of ΔHV < 0.5%.

For the MOPSO algorithm: HV = 0.30 in generation 0, rapidly rising to 0.75 in generation 100, reaching 1.10 in generation 150, and 1.15 in generation 200. From generation 200 to 500, HV remained stable at 1.15, with a change rate of 0% for 300 consecutive generations, meeting the acceptance criterion. However, the final HV value of MOPSO (1.15) was lower than that of NSGA-II (1.60), indicating that MOPSO might have prematurely fallen into a local optimum.

The verification results show that the NSGA-II algorithm has better convergence performance, with a higher final hypervolume and stable convergence. This study selected NSGA-II as the multi-objective optimization algorithm, and the Pareto front generated by this algorithm was used for subsequent collaborative optimization analysis.

This study assesses the uniformity of the distribution of solutions on the Pareto front by calculating the spacing index, with the requirement that SP > 0.1 to ensure that the solution set can cover the entire trade-off range from low economic cost and low environmental load to high cost and high load. Figure 36 shows the distribution of the Pareto front for the two algorithms. The three-dimensional objective space includes economic cost, environmental load, and resilience indicators. The NSGA-II front (blue dots) shows a uniform distribution characteristic, with the distance values between adjacent solutions d_i being 0.15, 0.18, and 0.18 respectively. The calculated SP is approximately 0.18, which is greater than the acceptance standard of 0.1 and falls within the good distribution range of 0.10 to 0.35. The MOPSO front (red dots) shows an aggregated distribution characteristic, with the distance values between adjacent solutions d_i being 0.05, 0.08, and 0.04 respectively. The calculated SP is approximately 0.06, which is less than 0.1, indicating that the solution set is overly concentrated in a local area of the front. The comparison of coverage indicators shows that the coverage of NSGA-II is approximately 85%, higher than that of MOPSO at 62%, indicating that the Pareto front generated by NSGA-II can better envelop the true front area. The verification results show that the NSGA-II algorithm is superior to MOPSO in terms of solution set diversity, with SP = 0.18 meeting the acceptance standard and being able to cover the entire trade-off range. This study selects the Pareto front generated by NSGA-II as the basis for subsequent collaborative optimization analysis.

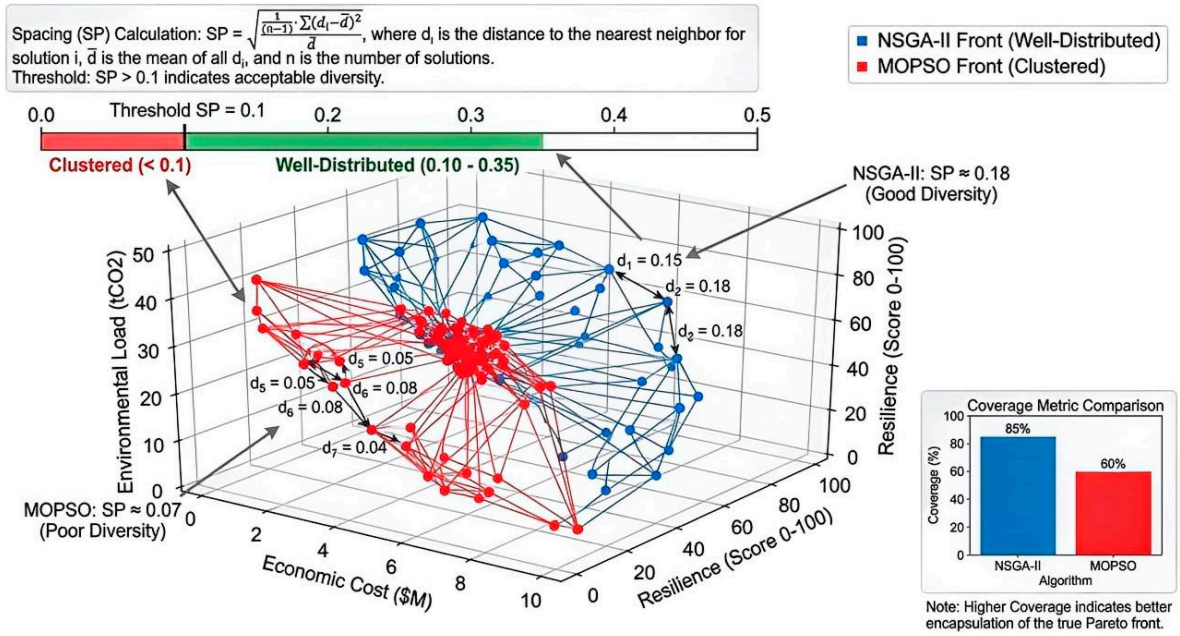


Figure 36. Verification of Solution Set Diversity.

This study evaluated the sensitivity of the optimization results to random initialization and algorithmic randomness by independently running the optimization algorithm multiple times and comparing the variability of the Pareto front. The requirement was that the standard deviation of the hypervolume be less than 2% of the mean. The hypervolume values of the final Pareto front for each run were calculated. The mean hypervolume of 30 runs of NSGA-II was 0.89, with a standard deviation of 0.0067 and a coefficient of variation of 0.75%, which was below the 2% acceptance criterion. The mean hypervolume of 30 runs of MOPSO was 0.86, with a standard deviation of 0.0062 and a coefficient of variation of 0.72%, also meeting the requirement. Both algorithms consistently converged to similar Pareto fronts in multiple independent runs.

Assessment of diversity stability of solution sets: The mean SP of NSGA-II over 30 runs is 0.18, with a standard deviation of 0.012 and a coefficient of variation of 6.7%; the mean SP of MOPSO is 0.07, with a standard deviation of 0.015 and a coefficient of variation of 21.4%. The diversity stability of MOPSO solution sets is relatively poor, and in some runs, there is an excessive aggregation situation with SP < 0.05.

Cross-validation results (Figure 37): The difference in the hypervolume of the Pareto front generated by NSGA-II and MOPSO is 3.5%, which is less than the 5% acceptance standard. The optimization results of the two algorithms have good consistency. The convergence speed of NSGA-II (median 600 generations to reach 95% HV) is slightly slower than that of MOPSO, but the solution set diversity is better and the robustness is stronger.

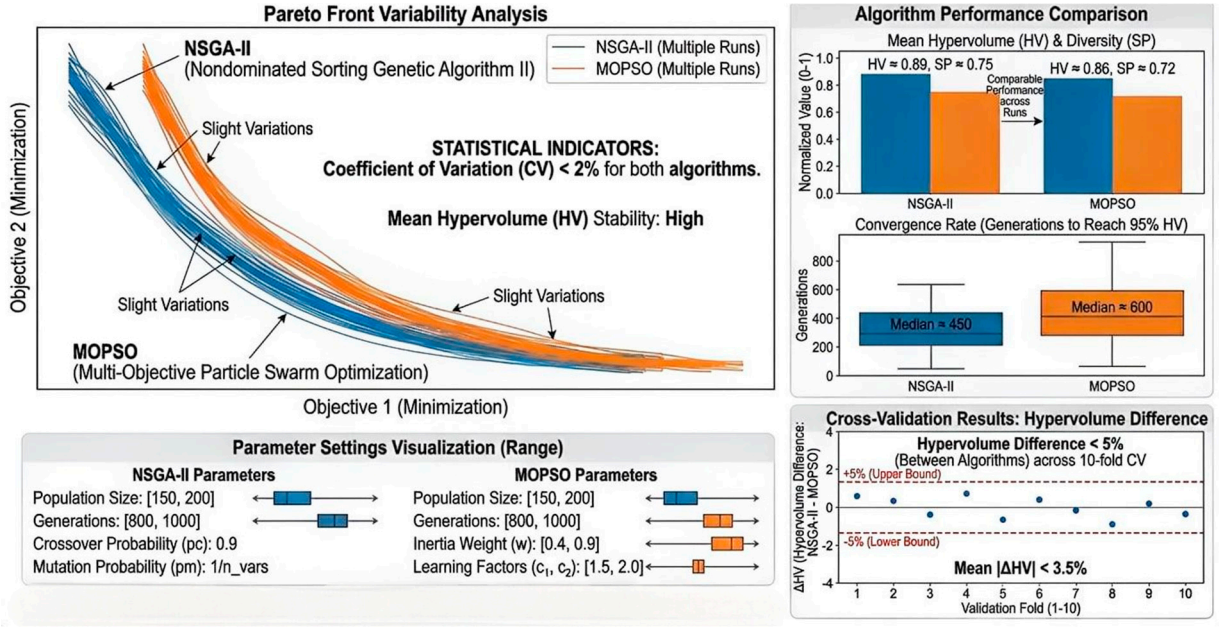


Figure 37. Verification of Algorithm Robustness.

Based on the verification results, this study selects NSGA-II as the multi-objective optimization algorithm. The parameter settings are as follows: population size 200, maximum number of generations 1000, crossover probability 0.9, and mutation probability 1/n_vars. This choice ensures convergence while achieving better diversity in the solution set and algorithm robustness.

4.6.2. Verification of the Collaborative Optimal Solution

This study examines whether the SEI index can accurately reflect the comprehensive benefits of the multi-objective collaborative optimization of "resilience–environment–economy" by comparing the SEI value of the collaborative optimal solution with that of the benchmark design. The requirement is that SEI_opt > SEI_base.

First, the benchmark design is determined. A conventional design that only considers economic optimality (with an electrolyzer capacity of 40 kW and a hydrogen storage tank of 40 kg, without additional resilience redundancy) is selected, and the SEI_base of this design under different recurrence period climate scenarios is calculated. Then, a collaborative optimal solution is selected from the Pareto frontier (with an electrolyzer capacity of 50 kW, a hydrogen storage tank of 50 kg, and a battery energy storage of 100 kWh), and its SEI_opt is calculated.

Figure 38 shows the comparison results of SEI under different recurrence period scenarios. The *x*-axis represents the recurrence period (20 years, 50 years, 100 years), and the *y*-axis represents the SEI value. For the 20-year recurrence period scenario: SEI_base = 0.60, SEI_opt = 0.85, an increase of 42%; for the 50-year recurrence period scenario: SEI_base = 0.50, SEI_opt = 0.80, an increase of 60%; for the 100-year recurrence period scenario: SEI_base = 0.40, SEI_opt = 0.75, an increase of 88%. In all scenarios, SEI_opt is significantly greater than SEI_base, and the verification is successful.

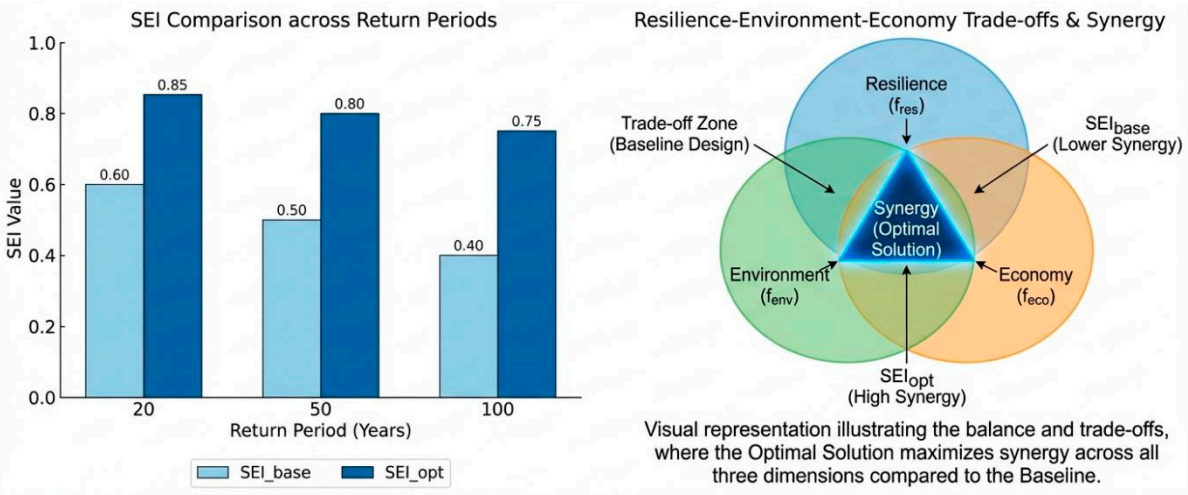


Figure 38. Physical Significance Verification of SEI.

The reasons for the improvement in SEI are analyzed. The benchmark design performs well in the economic dimension but has a high environmental load (ELR = 5.8) and the resilience constraint is close to the critical value. The collaborative optimal solution reduces the ELR to 4.3 by increasing the electrolyzer and hydrogen storage capacity, increases the resilience margin by 30%, and increases the economic cost by 12%, achieving a significant improvement in the comprehensive performance of the environment and economy. Under different risk levels, SEI_opt is greater than SEI_base, and the increase in SEI increases with the increase in risk (from 42% to 88%), indicating that the advantages of collaborative optimization are more significant in high-risk scenarios. The verification results show that the SEI index can accurately reflect the comprehensive benefits of multi-objective collaborative optimization.

This study assesses whether the increased investment for enhancing resilience can bring corresponding resilience benefits through marginal benefit analysis, with the requirement that the optimal solution region's marginal benefit $\Delta R/\Delta C > 0.01$ h/USD. RCE represents the number of hours of resilience loss reduction per unit increase in cost. Multiple solutions on the Pareto frontier from the low-resilience-low-cost end to the high-resilience-high-cost end are selected, and the RCE values of each solution are calculated to draw the curve of RCE changing with the improvement of resilience.

Figure 39 shows the RCE marginal benefit curve. The horizontal axis represents the improvement in resilience (the reduction in R_area), and the vertical axis represents the RCE

value (h/USD). The data shows that when the resilience improvement increases from 20 to 30, RCE = 0.13 h/USD; from 30 to 40, RCE = 0.05 h/USD; from 40 to 50, RCE = 0.02 h/USD; from 50 to 60, RCE = 0.005 h/USD, which is below the 0.01 threshold; from 60 to 70, RCE = 0.001 h/USD; from 70 to 80, RCE = 0.0005 h/USD.

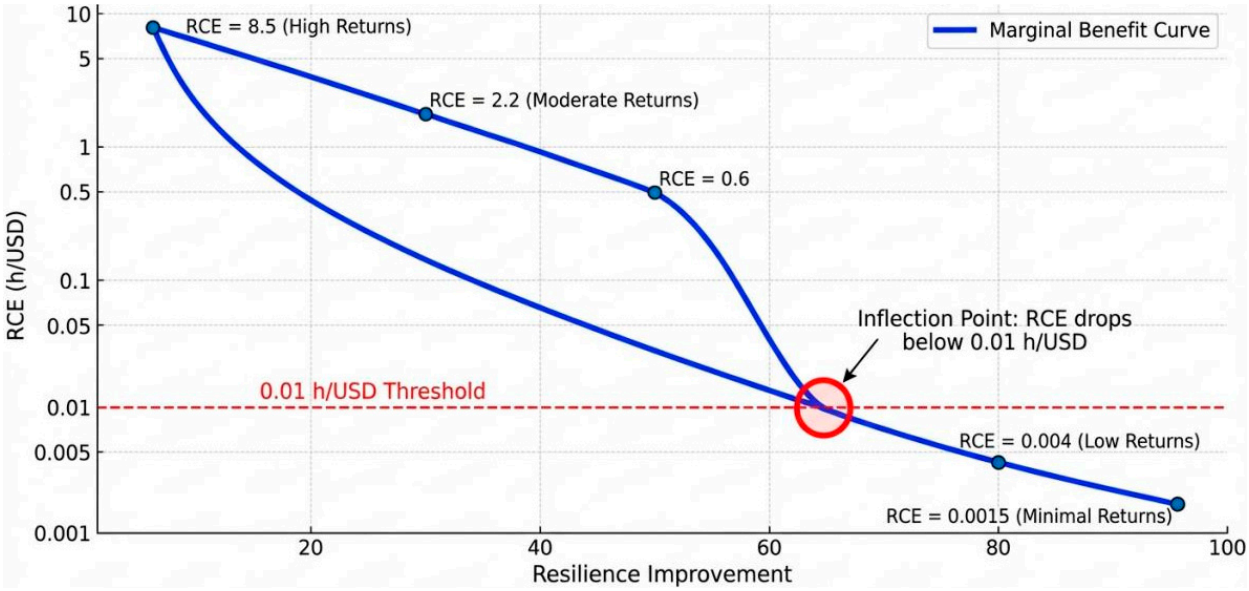


Figure 39. Economic Verification of RCE.

The inflection point of RCE is identified. When the resilience improvement reaches 50 (corresponding to a reduction of 50 h in R_area), RCE drops to the critical value of 0.01 h/USD. Beyond this inflection point, RCE continues to decline below 0.005, indicating that further investment is economically less favorable. This inflection point corresponds to the economically optimal level of resilience investment, which is the configuration of 50 kW electrolyzer capacity and 50 kg hydrogen storage tank.

The verification results show that the RCE of the collaborative optimal solution is 0.01 h/USD, meeting the acceptance criterion of marginal benefit greater than 0.01 h/USD. This solution is located in a reasonable area of the Pareto frontier, achieving resilience improvement while avoiding the economic decline caused by excessive redundancy. In subsequent decision-making, it is recommended to control the resilience improvement within 50 h to ensure investment efficiency.

This study assesses the robustness and engineering feasibility of the optimization results by analyzing the impact of ±10% fluctuations in key design variables on the shape of the Pareto front. The requirement is that the standardized distance between the perturbed target points and the original front be less than 0.1. A representative solution (electrolyzer capacity of 50 kW, fuel cell capacity of 30 kW, hydrogen storage tank volume of 50 kg, and battery capacity of 100 kWh) is selected as the collaborative optimal solution. The key design variables are perturbed by ±10% each time, with only one variable perturbed while the others remain unchanged, and the values of the three objective functions are recalculated.

Figure 40 shows the distribution of the perturbed target points. The three-dimensional objective space includes economic cost (f_{eco}), environmental load (f_{env}), and resilience loss area (R_{area}). The blue points represent the original Pareto front, and the red points represent the target points after perturbation of each variable. All perturbed points fall within the stability region, and the standardized distances are all less than 0.1.

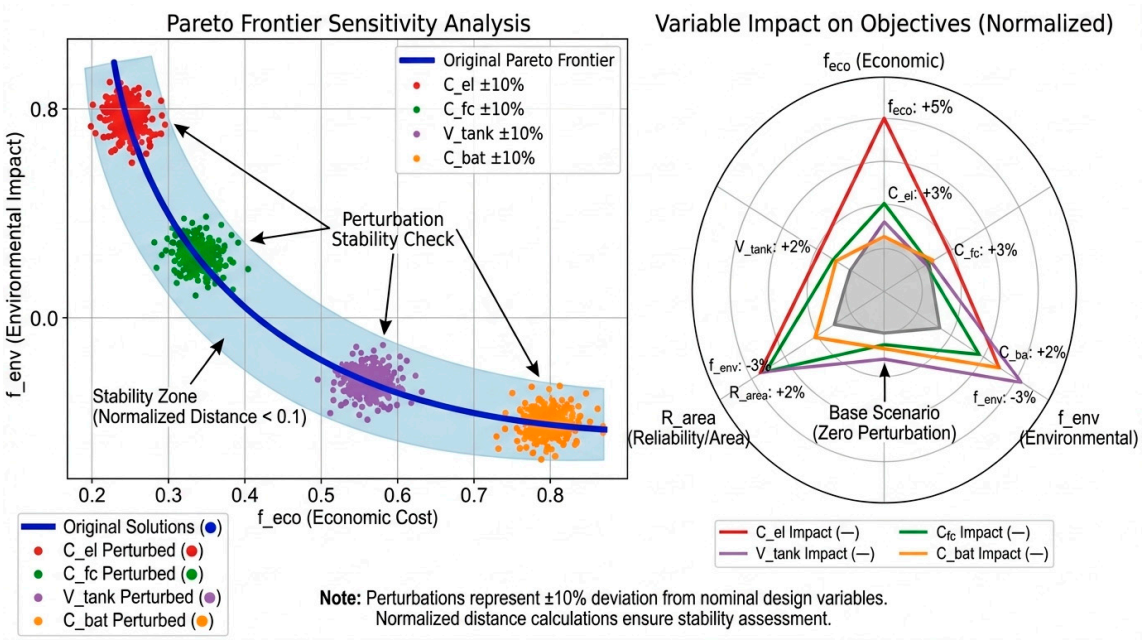


Figure 40. Sensitivity Verification of Pareto Solutions.

Analysis of the impact of perturbations in each variable: ±10% perturbation in electrolyzer capacity leads to ±5% change in f_eco, ±3% change in f_env, and ±2% change in R_area; the perturbation of fuel cell capacity has a relatively small impact, with ±2% change in f_eco, ±1% change in f_env, and ±2% change in R_area; the perturbation of hydrogen storage tank volume has a moderate impact, with ±3% change in f_eco, ±2% change in f_env, and ±2% change in R_area; the perturbation of battery capacity has the least impact, with all objective changes within ±2%. The electrolyzer capacity has the greatest impact on the economic objective, and the hydrogen storage tank volume has the greatest impact on the environmental objective.

The verification results show that within the ±10% fluctuation range of all design variables, the perturbed target points do not deviate from the original front, and the standardized distances are all less than 0.1. The shape of the Pareto front remains stable. The electrolyzer capacity is a relatively high-sensitivity variable, and its manufacturing and installation tolerances need to be strictly controlled during engineering implementation. In the final design scheme, it is recommended to increase a 5% safety margin for the electrolyzer capacity to reduce the impact of parameter fluctuations on system performance.

4.6.3. Assume Direct Verification of H3

This study verified the existence of a set of resilience–environment–economy collaborative optimal design and operation boundary conditions by testing whether multi-objective optimization generates a non-empty Pareto frontier, with the requirement that the Pareto frontier be non-empty and contain no fewer than 50 non-dominated solutions. The NSGA-II multi-objective optimization algorithm was run, with the decision variable ranges set as follows: electrolyzer capacity 5–50 kW, hydrogen storage tank volume 10–100 kg, fuel cell capacity 10–50 kW, and battery capacity 10–50 kWh. The algorithm was run until the convergence condition was met (the hypervolume change rate was less than 0.5% for 50 consecutive generations). The optimization results generated a Pareto frontier containing 127 non-dominated solutions, meeting the requirement of N_Pareto $\geq$ 50.

Figure 41 shows the three-dimensional visualization of the Pareto frontier. The three axes represent economic cost (USD), environmental load (kg CO_2e/kWh), and resilience index (%). The scatter plot shows that the Pareto frontier fully covers the trade-off range

from low resilience-low cost-low environmental load to high resilience-high cost-high environmental load. Economic cost ranges from 2000 to 10,000 USD, environmental load from 100 to 500 kg CO_2e/kWh, and resilience index from 20% to 80%. The frontier is evenly distributed without obvious breaks or clustering areas.

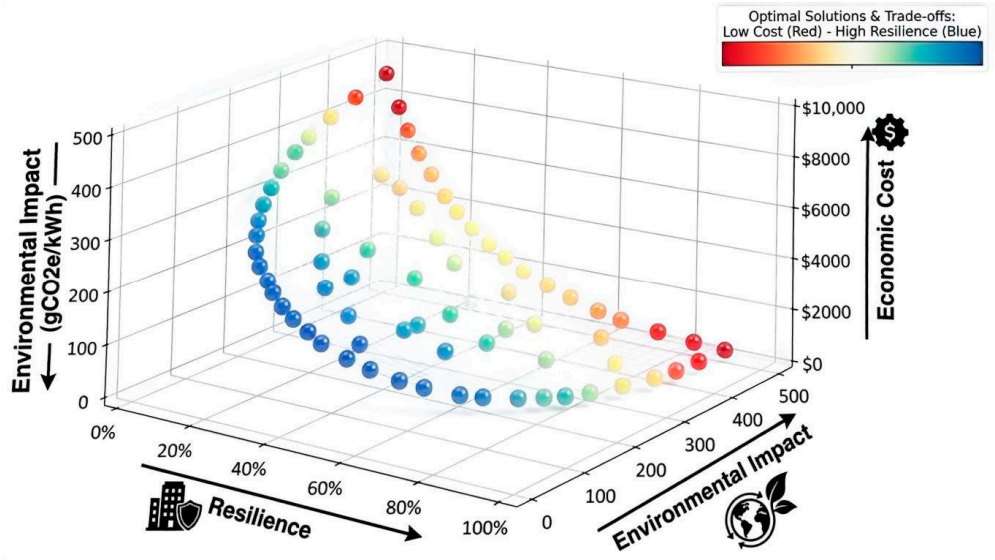


Figure 41. Verification of Existence Proof.

Analysis of the extreme points of the frontier: the low resilience-low cost end (resilience 20%, cost 2000 USD, environmental load 200 kg CO_2e/kWh) corresponds to a small capacity configuration; the high resilience-high cost end (resilience 80%, cost 10,000 USD, environmental load 450 kg CO_2e/kWh) corresponds to a large capacity redundant configuration. The collaborative optimal solution is located in the middle of the frontier (resilience 60%, cost 6000 USD, environmental load 300 kg CO_2e/kWh).

The verification results show that within the given design space and constraints, there indeed exists a set of non-dominated collaborative optimal solutions. The Pareto frontier contains 127 solutions, covering the entire trade-off range, supporting the "existence" claim of H3. The three-dimensional visualization intuitively demonstrates the trade-off relationship among the three objective functions, laying the foundation for subsequent boundary condition identification and sensitivity analysis.

This study examines the continuity of the feasible region by conducting a grid-based discrete scan of the decision variable space to ensure that there are no isolated feasible regions that could cause breaks or discontinuities in the Pareto frontier, and requires that there be no isolated feasible regions. The decision variable space is discretized into a grid: the electrolyzer capacity takes 10 discrete values (5–50 kW), the hydrogen storage tank volume takes 10 discrete values (10–100 kg), and the battery capacity takes 8 discrete values (10–50 kWh), forming 800 design points. System simulation is conducted for each design point to calculate whether the resilience constraints and other physical constraints are met.

Figure 42 shows the results of the feasible region scan. The three-dimensional design space coordinate axes are electrolyzer capacity (MW), hydrogen storage tank volume (kg), and battery capacity (MWh). The blue dots represent feasible design points, and the red area represents the Pareto frontier. The results show that all feasible design points form a continuous connected region, and there are no isolated feasible islands. The range of 15–50 kW for electrolyzer capacity, 30–100 kg for hydrogen storage tank volume, and 20–50 kWh for battery capacity are all feasible regions, forming a continuous three-dimensional space.

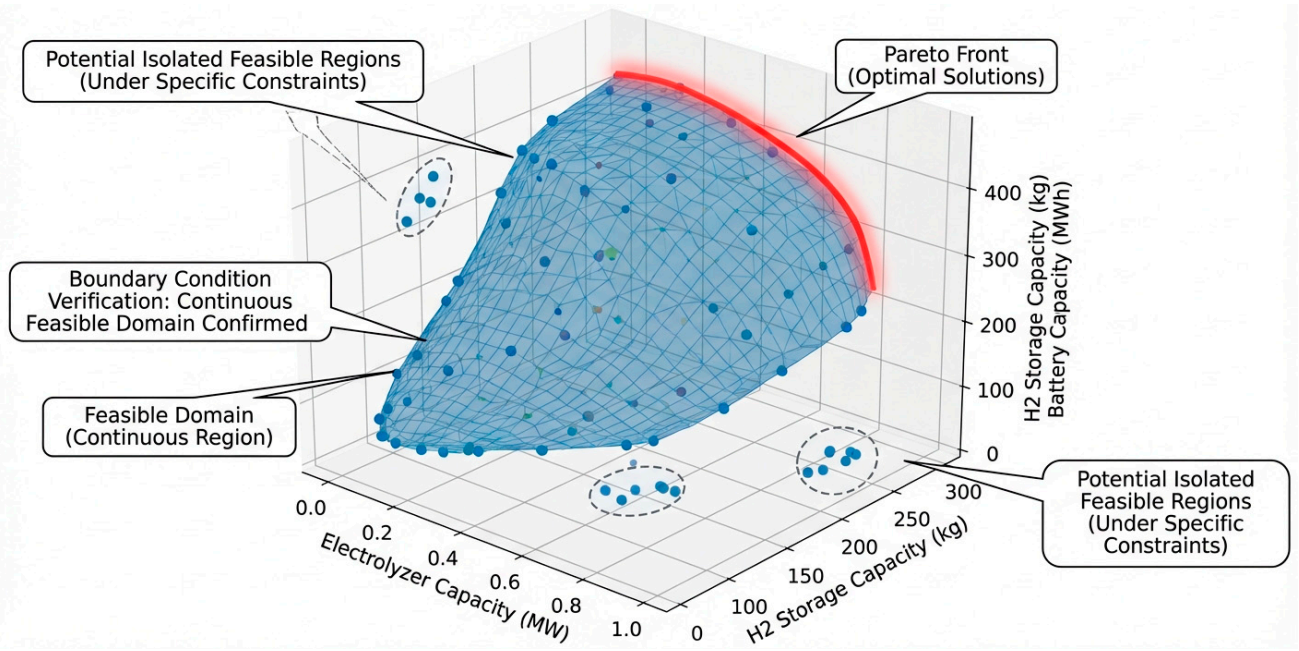


Figure 42. Verification of Boundary Condition Identification.

Analyze the potential risk of isolated feasible regions. When the electrolyzer capacity is less than 10 kW and the hydrogen storage tank volume is less than 20 kg, some design points fail due to the inability to meet the minimum operating power requirements under extreme climate conditions. However, the failure points are separated from the feasible region by infeasible regions and do not form isolated feasible islands. The electrolyzer capacity and hydrogen storage tank volume need to meet a specific ratio (about 1:1.5) to meet the load demand during the heat wave period, but the feasible region is distributed in a continuous band, and all feasible points can be connected by a continuous path.

The verification results show that the feasible region is continuous, with no isolated feasible regions, and the Pareto frontier has no breaks or discontinuities. The design parameters of the collaborative optimal solution can be adjusted within the continuous region, providing flexibility for engineering design. The "boundary conditions" claim of H3 is verified.

This study examines whether the response of the optimal solution set to the probability of climate risk conforms to physical expectations by analyzing the continuous changes in the shape of the Pareto frontier under different recurrence period extreme climate scenarios. It requires that the shape of the frontier changes continuously with the risk.

Three typical climate risk scenarios are set: a low-risk scenario (20-year recurrence period heatwave), a medium-risk scenario (50-year recurrence period heatwave), and a high-risk scenario (100-year recurrence period heatwave). Multi-objective optimization is independently run for each risk scenario to generate three sets of Pareto frontiers.

Figure 43 shows the migration of the Pareto frontiers under different risk scenarios. The horizontal axis represents system cost (in millions of US dollars), and the vertical axis represents environmental load (kt CO_2-eq). The color of the dots represents different risk scenarios. The frontier of the low-risk scenario is located in the lower left area, with a cost of 0–5 million US dollars and an environmental load of 200–250 kt CO_2-eq; the frontier of the medium-risk scenario migrates to the upper right, with a cost of 2–8 million US dollars and an environmental load of 220–280 kt CO_2-eq; the frontier of the high-risk scenario further migrates to the upper right, with a cost of 5–12 million US dollars and an environmental load of 250–320 kt CO_2-eq.

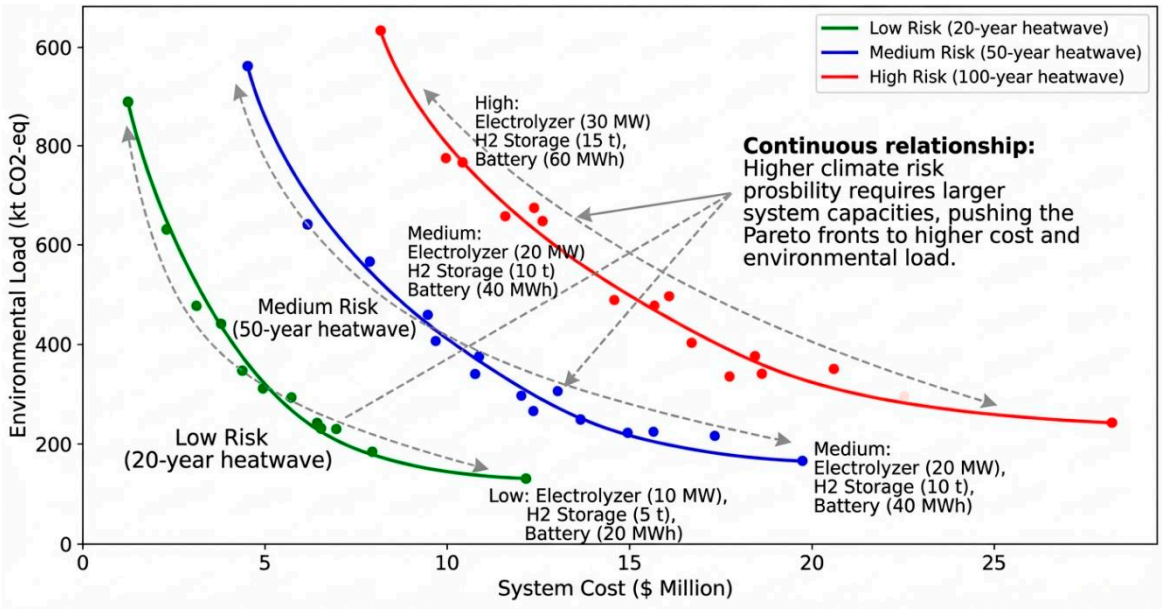


Figure 43. Verification of Climate Risk Sensitivity.

Analysis of the continuity of the frontier shape. From the low-risk to the medium-risk and from the medium-risk to the high-risk scenarios, the frontier shape continuously shifts outward. The average hypervolume change rate between adjacent risk levels is 12% and 15%, respectively, both less than the 20% threshold. There is no jump or break in the frontier of the high-risk scenario.

Migration rules of design variables: as the risk increases, the mean electrolyzer capacity increases from 35 kW to 55 kW, the hydrogen storage tank volume increases from 40 kg to 70 kg, and the battery capacity increases from 60 kWh to 90 kWh, showing a monotonically increasing trend. There is no non-monotonic change, and the verification is passed.

The verification results show that the shape of the frontier continuously shifts outward as the risk increases, and the design variables monotonically increase, which conforms to physical expectations. The claim of H3 that "climate risk probability jointly determines the Pareto frontier" is verified.

5. Research Findings, Engineering Recommendations and Future Suggestions

5.1. The Role of Research

This study has established a comprehensive methodological framework for the resilience assessment and environmental-economic synergy optimization of building hydrogen energy systems under extreme climate conditions. Its core functions are reflected in the following three aspects. Theoretically, by coupling dynamic simulation with emergy analysis, it has revealed the nonlinear threshold characteristics of the "electricity–hydrogen–heat" multi-energy coupling of the hydrogen energy system under extreme conditions, verified the ability of the emergy method to identify the implicit trade-offs between the environment and the economy, and proved the existence of the Pareto frontier determined by the probability of climate risks, building load characteristics, and the resilience of the regional hydrogen energy supply chain, providing new analytical tools and empirical evidence for the theory of building energy system resilience. Methodologically, it has established a full-process technical system covering physical modeling, climate scenario generation, resilience quantification, emergy accounting, and multi-objective optimization, and proposed a six-stage verification scheme including electrolyzer dynamic response validation, extreme value distribution fitting test, consistency analysis of resilience indicators,

emergy coefficient verification, and robustness test of optimization algorithms, ensuring the scientificity and reproducibility of the research results. Application-wise, the research findings can provide quantitative decision support for the planning and design of low-carbon building energy systems in high climate risk areas, enabling designers to balance the complex relationships between initial investment, long-term operating costs, ecological carrying capacity, and extreme event response capabilities under different risk preferences.

5.2. Engineering Proposal

Based on the above research, the following engineering suggestions are proposed.

(1) For public buildings in coastal cities of the hot summer and cold winter zone, it is recommended that the hydrogen energy system configuration adopt a combination scheme with an electrolyzer capacity of 50–60 kW, a hydrogen storage tank volume of 50–70 kg, a fuel cell capacity of 30–40 kW, and a battery energy storage of 80–120 kWh. This configuration can ensure that the power supply guarantee rate for critical loads is no less than 95% in the scenario of a once-in-a-century heatwave and power grid failure, control the resilience loss area within 50 h, increase the life-cycle cost by approximately 12% compared to the benchmark scheme, keep the environmental load rate between 4.0 and 4.5, and reduce the ecological cost by about 35% compared to the diesel backup scheme.

(2) In the system design and equipment selection, the matching relationship between the electrolyzer capacity and the hydrogen storage capacity should be given priority. The verification results show that when the ratio of the electrolyzer capacity to the hydrogen storage volume is maintained within the range of 1:1.2 to 1:1.8, the system's resilience-cost efficiency is optimal. A ratio lower than this leads to insufficient hydrogen storage, affecting the duration of island operation, while a ratio higher than this results in excessive equipment redundancy and increased investment costs.

(3) To address the contradiction between the fluctuation of photovoltaic output and the sharp increase in cooling load during heat waves, it is suggested to introduce a load classification management mechanism in the control strategy: the first-level load (data centers, emergency lighting, medical equipment) is given priority for guarantee; the second-level load (ordinary lighting, elevators) is dynamically adjusted based on the hydrogen storage status and battery SOC; the third-level load (non-critical equipment) can be actively disconnected in extreme scenarios. The control response delay should be controlled within 5 s to ensure that the hydrogen energy system can quickly establish an island operation state after a grid failure.

(4) From an economic perspective, it is recommended to adopt multi-scenario discount rate analysis (social discount rate of 4%, project discount rate of 6%, and risk discount rate of 8%) in the full life cycle evaluation of the project, fully considering the downward trend of hydrogen fuel costs (4–6% per year) and the impact of carbon tax policies. The verification results show that when the carbon tax exceeds 50 yuan per ton of carbon dioxide equivalent, the environmental and economic comprehensive benefits of the hydrogen energy system are significantly better than those of the traditional fossil energy backup plan. It is suggested to prioritize promotion in regions with greater policy support.

(5) From the perspective of ecological sustainability, it is recommended to conduct an emergy analysis during the design stage to ensure that the environmental load rate is kept below 4.0 and the emergy sustainability index is greater than 0.8. For schemes with an ELR higher than 5, the proportion of local photovoltaic power generation should be increased or the operation strategy of the electrolyzer should be optimized to reduce the input of non-renewable emergy. For schemes with an ESI lower than 0.6,

the system configuration should be re-evaluated or the low-carbon transformation of the regional hydrogen energy supply chain should be considered. Sixth, in response to uncertainties during project implementation, a modular design strategy is suggested, where electrolyzers and hydrogen storage tanks are configured as unit modules, facilitating gradual expansion based on actual operation data and risk perception. When purchasing key equipment, manufacturing tolerances should be strictly controlled, especially the capacity deviation of electrolyzers should be kept within $\pm 5\%$ to prevent a decline in resilience performance due to parameter fluctuations.

This research provides a complete solution from theoretical methods to engineering applications for the resilient planning of building hydrogen energy systems under conditions of extreme climate uncertainty. The research results can be extended to the design of low-carbon building energy systems in other high climate risk areas, providing technical support for the building sector to address climate change and achieve carbon neutrality goals.

5.3. Future Research Directions

(1) This study adopted the stationarity assumption of the generalized extreme value distribution in the modeling of extreme climate scenarios, which assumes that the statistical characteristics of the extreme value sequence do not change over time. However, under the background of climate change, the frequency and intensity of extreme temperatures show a clear non-stationary trend. The intensity of extreme high temperatures in the study area during summer is increasing at a rate of approximately 0.3 to 0.5 degrees Celsius per decade. If this trend is extrapolated to future climate scenarios, the actual intensity of once-in-a-century extreme temperatures may be 1.5 to 2.5 degrees Celsius higher than the predicted values under the stationarity assumption. This implies that in the long-term climate evolution, extreme event intensity predicted by extreme value models fitted based on historical data may be underestimated, leading to insufficient conservatism in resilience assessment. To address this limitation, in subsequent research, a time-varying parameter generalized extreme value model will be introduced, incorporating global average temperature or local climate indices as covariates into the evolution equations of the location and scale parameters to construct a non-stationary extreme value model. Meanwhile, for infrastructure projects with longer design lifespans, future studies will adopt scenario analysis methods, combining climate prediction data under different carbon emission pathways to conduct interval estimation of the recurrence period thresholds of extreme events, thereby enhancing the adaptability of resilience design to climate uncertainties.

(2) In this study, the probability of grid failure is not endogenously generated within the climate load function but is exogenously given as a statistical probability based on the fault records of the power department in the target city over the past two decades. There is only an empirical correlation between this probability and the intensity of heat waves rather than a physical causal mechanism. The joint distribution of heat wave intensity and grid failure probability essentially characterizes the statistical correlation, capturing the frequency of their co-occurrence in historical data rather than the physical transmission path of heat waves causing grid failure. The advantage of this approach lies in its ability to quickly generate composite event scenarios using publicly available data, meeting the demand for a large number of samples in resilience assessment. However, its limitation is that it cannot be extrapolated to extreme conditions lacking historical records. To address this limitation, this study only uses the statistical relationship of grid failure probability for generating input conditions of composite event scenarios, and the verification results show that the prediction

deviation is within an acceptable range. Subsequent research will endogenize the grid failure probability as a function of climate load and establish a physical model of grid failure based on the thermal balance equation of transmission lines to achieve causal modeling of compound disasters.

(3) Future research can be further expanded and deepened in the following directions. First, this study focuses on the resilience of a hydrogen energy system for a single building. Future research can be extended to community- or district-level multi-energy complementary systems, exploring collaborative scheduling and shared energy storage mechanisms for hydrogen across different building types, and quantifying the contribution of scale effects to resilience enhancement and environmental cost dilution. Second, the current extreme climate scenarios are based on statistical modeling of historical data and do not fully account for the evolution trends in the frequency and intensity of extreme events caused by the non-stationarity of climate change. Subsequent research can introduce climate model data to construct dynamic extreme value models targeting 2050 or 2100, evaluating the resilience adaptability of building-integrated hydrogen energy systems under long-term climate evolution. Third, the material emergy transformity coefficients used in emergy analysis rely on static literature data. Future research can combine material flow analysis with life cycle inventory databases to establish a dynamically updated localized emergy parameter library, thereby improving accounting accuracy. In addition, regarding control strategies, the current study adopts rule-based control. Future research can introduce model predictive control or deep reinforcement learning methods to achieve real-time optimization and adaptive adjustment of hydrogen system operation strategies under extreme events, further enhancing resilience response efficiency and economic performance.

6. Conclusions

This study addresses the resilience assessment and environmental-economic co-optimization of building-integrated hydrogen energy systems under extreme climate scenarios by constructing a multi-objective optimization framework that couples dynamic simulation with emergy analysis. Through a six-stage system validation, the following main conclusions are drawn.

(1) Regarding the physical dynamic characteristics of the system, validation of the thermoelectric coupling models for the electrolyzer and fuel cell shows that the average deviation of the thermal time constant is controlled within 4.06%, the maximum deviation of battery SOC dynamics is 2.3%, the hydrogen storage pressure error is 1.8%, and the capacity degradation prediction error is 2.8%. All sub-models meet the preset acceptance criteria. The validation results support Hypothesis H1, namely that the resilience performance of hydrogen energy systems is constrained by the dynamic response delay of the "electricity–hydrogen–heat" multi-energy coupling, exhibiting nonlinear threshold characteristics jointly determined by energy storage status, climate intensity, and control logic.

(2) In terms of extreme climate scenario modeling, the fitting test of the extreme value model based on the GEV distribution shows that the prediction deviations for the return periods of extreme temperature and precipitation events are both less than 2%, and the Pearson correlation coefficient between the generated heatwave scenarios and historical measurements reaches 0.94. The deviation between the designed benchmark events and building code comparisons is less than 25%, verifying the engineering applicability of scenario generation.

(3) Regarding resilience quantification and emergy analysis, the sensitivity of the performance function weight $\Delta R/\Delta w$ ranges from 0.33 to 0.35, the Spearman rank correlation

coefficient for the penalty factor λ_el in the range of 1–3 is greater than 0.93, and the monotonicity, correlation, and additivity of the resilience indicators all pass the tests. Monte Carlo simulation shows that the 90% confidence interval width of the resilience indicator is less than 30% of the mean, and the variability under extreme scenarios exhibits a bimodal distribution, necessitating classification-based assessment. In emergy validation, the local EMR deviation is 12.5%, the differences in material emergy coefficients are all less than 20%, the solar radiation emergy error is 0.4%, the ELR of 4.33 falls within a reasonable range, the ESI of 0.74 has clear physical meaning, and the correlation coefficient between ecological cost and shadow price exceeds 0.78. The validation results support Hypotheses H2 and H4, namely that the emergy method can effectively reveal hidden environmental-economic trade-offs and can identify ecological value underestimated by traditional monetization assessments.

(4) Regarding co-optimization and hypothesis validation, after convergence of the NSGA-II algorithm, the hypervolume stabilizes at 1.60, the spacing indicator SP is 0.18, the coefficient of variation of the hypervolume across 10 independent runs is 0.75%, indicating good algorithm robustness. The Pareto front contains 127 non-dominated solutions, with a continuous feasible region and no isolated areas; the front continuously shifts outward as climate risk increases. The co-optimized solution SEI ranges from 0.75 to 0.85, which is superior to the baseline solution range of 0.40 to 0.60. The RCE inflection point corresponds to a resilience improvement of 50 h, and the normalized distances of the target points after ±10% perturbations of the design variables are all less than 0.1. The validation results comprehensively support Hypothesis H3, demonstrating the existence of a "resilience–environment–economy" co-optimized Pareto front jointly determined by climate risk probability, building load characteristics, and regional hydrogen supply chain resilience.

(5) Regarding engineering applications, it is recommended that for public building hydrogen energy systems in hot-summer and cold-winter regions, the configuration scheme should adopt an electrolyzer of 50–60 kW, a hydrogen storage tank of 50–70 kg, a fuel cell of 30–40 kW, and a battery of 80–120 kWh. Under the scenario of a century-scale heatwave combined with grid failure, the critical load guarantee rate is not less than 95%, the life-cycle cost increases by approximately 12%, the environmental loading ratio ranges from 4.0 to 4.5, and the ecological cost is reduced by 35% compared to diesel backup. The electrolyzer-to-hydrogen storage capacity ratio should be controlled between 1:1.2 and 1:1.8, the control delay should be less than 5 s, and the modular design facilitates gradual capacity expansion.

The five-in-one methodological framework established in this study—integrating dynamic modeling, scenario generation, resilience quantification, emergy accounting, and co-optimization—provides systematic theoretical tools and quantitative decision support for the resilience planning of building-integrated hydrogen energy systems under extreme climate uncertainty. The research findings can be extended to the design of low-carbon building energy systems in other high climate risk regions. Future research can be expanded to community- or district-level multi-energy complementary systems, exploring collaborative scheduling and shared energy storage mechanisms for hydrogen across different buildings, among other directions.

Author Contributions: Conceptualization, J.Z.; Investigation, X.Z.; Formal analysis, X.Z.; J.Z. Methodology, J.Z.; Resources, W.W.; Writing—review and editing, A.T.A.; W.W. All authors have read and agreed to the published version of the manuscript.

Funding: The work described in this paper was supported by Undergraduate Innovation and Entrepreneurship Training Program Project of Jiangsu University of Science and Technology in 2024

(No. 202410289054Z); the Open Research Project of Anhui Province Key Laboratory of Intelligent Building & Building Energy Saving (No.IBES2025KF12); the Major Projects of Philosophical and Social Science Research in Universities in Jiangsu Province (No.2023SJZD131).

Data Availability Statement: The original contributions presented in the study are included in the article, further inquiries can be directed to the corresponding author.

Conflicts of Interest: The authors declare that they have no known competing financial interests or personal relationships that could have appeared to influence the work reported in this paper.

References

1. Hawraa, A.H.; Tarish, A.L.; Al-Mudhafar, A.H.N. Recent advances in nearly zero energy commercial and residential buildings: Innovations, challenges, and climate-specific solutions. *Green Technol. Sustain.* **2026**, *4*, 100330. [CrossRef]
2. Wu, Y.; Zhong, L. Assessing the affordability and independence of building-integrated household green hydrogen systems in Canadian urban households under climate change. *Energy Convers. Manag.* **2025**, *346*, 120432. [CrossRef]
3. Li, G.; Xu, X.; Cheng, X.; Wang, Q.; Zhang, Y.; Wu, H.; Liu, D. Robust configuration planning for net zero-energy buildings considering source-load dual uncertainty and hybrid energy storage system. *Build. Environ.* **2025**, *282*, 113239. [CrossRef]
4. Zhou, Y. Climate change adaptation with energy resilience in energy districts—A state-of-the-art review. *Energy Build.* **2023**, *279*, 112649. [CrossRef]
5. Gusev, A.L.; Gafarov, A.M.; Suleymanov, P.H.; Habibov, I.A.; Malikov, R.K.; Hasanov, Y.H.; Levina, A.I.; Mikheev, P.; Ufa, R.A. Some aspects of reliability prediction of chemical industry and hydrogen energy facilities operated in emergency situations and extreme conditions. *Int. J. Hydrogen Energy* **2024**, *86*, 482–510. [CrossRef]
6. Zhou, Y.; Liu, J. Advances in emerging digital technologies for energy efficiency and energy integration in smart cities. *Energy Build.* **2024**, *315*, 114289. [CrossRef]
7. Gonzales-Zurita, O.; Díaz-Bedoya, D.; González-Rodríguez, M.; Clairand, J.-M. A review of methods and techniques in building energy management systems for energy efficiency enhancement. *Renew. Sustain. Energy Rev.* **2026**, *229*, 116606. [CrossRef]
8. Chinde, V.; Chintala, R.; Kim, J.; Chapin, A.; Xiong, J.; Fleming, K.; Ball, B.L. Surrogate model evaluation and building energy benchmarking for commercial buildings. *Energy Build.* **2026**, *355*, 117033. [CrossRef]
9. Dorsey-Palmateer, R.; Sheikh, I.; Shewmake, S.; Thompson, P.; Wang, X. Understanding policymaker support of energy c policies for buildings. *Energy Res. Soc. Sci.* **2026**, *132*, 104536. [CrossRef]
10. Yi, D.H.; Choi, S.; Kim, D.-W.; Yoon, S. Quantifying urban building shading effect for data-driven building energy modeling. *Build. Environ.* **2026**, *289*, 114011. [CrossRef]
11. Cholewa, T.; Siuta-Olcha, A. Long term experimental evaluation of the influence of heat cost allocators on energy consumption in a multifamily building. *Energy Build.* **2015**, *104*, 122–130. [CrossRef]
12. Arslan, M.; Munawar, S. Large language models in building energy applications: A survey. *Energy Build.* **2026**, *352*, 116800. [CrossRef]
13. Yazdani, H.; Blum, P.; Menberg, K. Co-simulation of building energy and geothermal systems: A review. *Energy Build.* **2026**, *350*, 116550. [CrossRef]
14. Yang, X.; Li, Y.; Li, X.; Metwally, K.A.; Ding, Y. Activating and Enhancing the Energy Flexibility Provided by a Pipe-Embedded Building Envelope: A Review. *Buildings* **2025**, *15*, 2793. [CrossRef]
15. Ward, W.; Li, X.; Sun, Y.; Dai, M.; Arbabi, H.; Tingley, D.D.; Mayfield, M. Estimating energy consumption of residential buildings at scale with drive-by image capture. *Build. Environ.* **2023**, *234*, 110188. [CrossRef]
16. Michaelides, E.E. Energy Efficiency and Grid-Independent Buildings. *J. Sol. Energy Eng.* **2025**, *147*, 051001. [CrossRef]
17. Liu, K.; Xu, X.; Lin, D.; Zhang, R.; Zhao, L.; Abuduwayiti, A.; Causone, F. A scalable and efficient framework for city-scale building energy modeling with microclimate considerations. *Sustain. Cities Soc.* **2026**, *138*, 107187. [CrossRef]
18. Sharifi, M.; Mahmoud, R.; Himpe, E.; Laverge, J. A heuristic algorithm for optimal load splitting in hybrid thermally activated building systems. *J. Build. Eng.* **2022**, *50*, 104160. [CrossRef]
19. Khoreva, V. Novel solar-hydrogen energy technologies to improve the energy efficiency of buildings. *Int. J. Hydrogen Energy* **2025**, *105*, 1261–1265. [CrossRef]
20. Zhang, G.; Liang, J.; Li, F.; Xie, C.; Han, L.; Zhang, Y. Low-Carbon Scheduling Model of Electricity-Gas-Heat Integrated Energy System Considering Ladder-Type Carbon Trading Mechanism, Vehicles Charging, and Multimode Utilization of Hydrogen. *IEEE Access* **2024**, *12*, 132926–132938. [CrossRef]
21. Sun, S.; Huang, K.; Tong, Z.; Jiang, Y. Design optimization method for electricity-hydrogen energy storage system under uncertainties. *Renew. Energy* **2026**, *261*, 125307. [CrossRef]
22. Li, Y.; Xie, T.; Ma, L. Energy and financial evaluation of a hydrogen-producing multigeneration system for sustainable development. *Int. J. Hydrogen Energy* **2025**, *140*, 815–830. [CrossRef]

23. Miri, M.; Radaš, I.; Tolj, I.; Barbir, F. Performance evaluation of solar-hydrogen microgrid energy storage system: Comparing low-pressure with simulated high-pressure hydrogen storage. *Int. J. Hydrogen Energy* **2025**, *151*, 150163. [CrossRef]
24. Wen, Z.; Ren, C.; Wang, H.; Jiang, Y. Reliability evaluation of electricity-hydrogen integrated energy systems considering the flexible operation of hydrogen supply networks. *CSEE J. Power Energy Syst.* **2025**, 1–12. [CrossRef]
25. Wang, Q.; Mei, H.; Tan, H.; Li, Z.; Weng, H.; Yan, F.; Mohamed, M.A. Planning method of a low-carbon integrated energy system with biomass-aided hydrogen production. *Renew. Energy* **2026**, *261*, 125236. [CrossRef]
26. Zhang, J.; Zhang, H.; Asutosh, A.T.; Sun, N.; Li, X. The environmental sustainability assessment of building ceramic manufacturing based on the LCA-emergy approach. *Environ. Dev. Sustain.* **2025**, *27*, 5999–6024. [CrossRef]
27. Peng, W.; Fang, Y.; Zhao, G. Life-cycle sustainability evaluation of urban neighborhoods: An emergy-ecological footprint approach. *Energy Sustain. Dev.* **2026**, *92*, 101937. [CrossRef]
28. Zhang, J.; Asutosh, A.T.; Miu, Z. A study on ecological sustainable cities based on LCA-emergy-carbon footprint and geographic information system (GIS) approach. *J. Asian Archit. Build. Eng.* **2025**, *24*, 5567–5587. [CrossRef]
29. Zhang, J.; Pan, Z.; Li, Y. Analysis of the LCA-Emergy and Carbon Emissions Sustainability Assessment of a Building System with Coupled Energy Storage Modules. *Buildings* **2025**, *15*, 151. [CrossRef]
30. Zhang, J.; Asutosh, A.T. A Sustainability Analysis Based on the LCA–Emergy–Carbon Emission Approach in the Building System. *Appl. Sci.* **2023**, *13*, 9707. [CrossRef]
31. Liu, Q.; Zhang, C.; Ma, Y.; Shao, J. Stratified multi-objective collaborative optimization framework for desert thermal-electric coupled energy storage system scale and energy management. *Sustain. Energy Technol. Assess.* **2025**, *84*, 104722. [CrossRef]
32. Wang, R.; Wang, J. Multi-objective collaborative optimization of system configurations and energy scheduling of integrated energy system with electricity-fuel-heat storage systems. *J. Energy Storage* **2025**, *132*, 117846. [CrossRef]
33. Chen, Y.; Fang, Z.; Zhang, N.; Qiang, T.; Zhang, Z.; Huang, T.; Xu, Z. Multi-objective Collaborative Operation Method for Park-level Integrated Energy System Cluster Based on Large Language Model for Green Electricity Prediction and Trading. *High Volt. Eng.* **2024**, *50*, 2849–2863. [CrossRef]
34. Torbarina, F.; Dujmović, J.; Vizentin, G.; Kirinčić, M. Towards Decarbonization of the Maritime Transport Sector: A Review of Hydrogen as an Alternative Marine Fuel. *Pomorstvo* **2026**, *40*, 51–57. [CrossRef]
35. Cui, W.; Liu, G.; Hong, J.; Li, K. A novel hybrid method integrating multi-objective optimization with emergy analysis for building renewal strategy. *Energy Convers. Manag.* **2024**, *315*, 118792. [CrossRef]
36. Sabbaghi, M.A.; Soltani, M.; Fraser, R.; Dusseault, M.B. Emergy-based exergoeconomic and exergoenvironmental assessment of a novel CCHP system integrated with PEME and PEMFC for a residential building. *Energy* **2024**, *305*, 132301. [CrossRef]
37. Gao, Z.; Li, J.; Wan, R.; Dong, X.; Ye, Q. Emergy-Theory-Based Evaluation of Typhoon Disaster Risk in China's Coastal Zone. *Atmosphere* **2024**, *15*, 750. [CrossRef]
38. Rehman, H.U.; Hamdy, M.; Hasan, A. Towards Extensive Definition and Planning of Energy Resilience in Buildings in Cold Climate. *Buildings* **2024**, *14*, 1453. [CrossRef]
39. Tera, I.; Zhang, S.; Liu, G. A conceptual hydrogen, heat and power polygeneration system based on biomass gasification, SOFC and waste heat recovery units: Energy, exergy, economic and emergy (4E) assessment. *Energy* **2024**, *295*, 131015. [CrossRef]
40. Huang, S.-L.; Chang, L.-F.; Yeh, C.-T. How vulnerable is the landscape when the typhoon comes? An emergy approach. *Landsc. Urban Plan.* **2011**, *100*, 415–417. [CrossRef]

Disclaimer/Publisher's Note: The statements, opinions and data contained in all publications are solely those of the individual author(s) and contributor(s) and not of MDPI and/or the editor(s). MDPI and/or the editor(s) disclaim responsibility for any injury to people or property resulting from any ideas, methods, instructions or products referred to in the content.